

# LIBRARY Michigan State University

This is to certify that the

dissertation entitled

Transverse Vorticity Measurements In An Excited Two-Dimensional Mixing Layer

presented by

Peter John Disimile

has been accepted towards fulfillment of the requirements for

Ph.D. degree in Mechanical Engineering

Major professor

Date 28 June 1984



RETURNING MATERIALS:
Place in book drop to remove this checkout from your record. FINES will be charged if book is returned after the date stamped below.

# TRANSVERSE VORTICITY MEASUREMENTS IN AN EXCITED TWO-DIMENSIONAL MIXING LAYER

Вy

Peter John Disimile

# A DISSERTATION

Submitted to

Michigan State University

in partial fulfillment of the requirements

for the degree of

DOCTOR OF PHILOSOPHY

Department of Mechanical Engineering

© Copyright by
PETER JOHN DISIMILE
1984

# ABSTRACT

# TRANSVERSE VORTICITY MEASUREMENTS IN AN EXCITED TWO-DIMENSIONAL MIXING LAYER

By

#### Peter John Disimile

Transverse vorticity time series have been obtained in a weakly excited, single-stream mixing layer. Quasi-intantaneous vorticity time series were obtained with a four-wire array and phase averaged transverse vorticity time series were obtained with an X-array at each of the 414 points in the measurement grid. These data showed the regions of vortex formation, saturation and decay. In addition to the detailed vorticity measurements in the mixing layer, the upstream turbulent boundary layer was also documented.

The spatial locations of the distinctive vortex motions were found to be in good agreement with previous studies. Using the vorticity field documentation, the spatial distribution and the temporal evolution of the primary vortex motions in the mixing layer were examined. The spatial distribution revealed deep depressions of the

vorticity contours on the high speed side of the mixing layer. The primary growth of the vortical structure was observed to be on the low speed side. In addition, it has been observed (over 15% of the available excitation cycle) that the core of the vortical structures appear to move at substantially different speeds.

This detailed documentation of the vorticity field and the upstream turbulent boundary layer has also, i) produced information showing the tearing and fusing of vortical contours in the phase averaged plots and ii) shown the affects of excitation on the turbulent boundary layer.

The quasi-instantaneous transverse vorticity measurements indicate absolute values of peak vorticity which are an order of magnitude greater than those indicated by phase averaged transverse vorticity measurements. These large quasi-instantaneous transverse vorticity fluctuations indicate strong mixing throughout the core and periphery of the newly formed and saturated vortical structures. Althrough the magnitude is approximately the same throughout these structures, the frequency of occurrence of these large fluctuations appears to be less on the low speed side of the newly formed vortex.

I dedicate this Dissertation in memory of my father,
Peter Disimile

#### **ACKNOWLEDGMENTS**

I would like to express my appreciation to all the people that I have worked with during the past four years. Particularily, I would like to extend a warm thank you to the following people:

S. Kendall	T. Skeltis	M. Murawski

- J. Klewicki R. Watson J. Gafford
- S. Strachan R. Greene D. O'Reagan
- D. McKenny S. Cary D. Smith
- P. Crowley R. Robb H. Pollack
- E. Gunckle R. Annan T. Gentner
- J. Peters R. Focia G. Statkiewicz
- J. Davoust K. Cole M. Brower
- P. Hennessey B. Agar R. Rose

In addition, I would like to express my gratitude;

To the men in the machine shop, especially D. Childs and S. Kurtz.

To the people in DER, especially M. J. Kroll and K. Perkins.

To C. L. Klewicki for the software development of PROCESS I and II.

- To S. Ali for acting as a vibration absorber.
- To O. Ahmed for an excellent drafting job.
- To C. E. Wark for the support, nourishment and encouragement she provided under very difficult conditions.
- To B. Curlett for the many long nights he spent cunching data and helping me prepare this document. His hard work and dedication will never be forgotten.
- To Dr. J. F. Foss for providing me with the opportunity to design and construct a major flow facility.

To the NASA Ames Research Center, grant monitor: Dr. M. Rubesin.

I would also like to express my appreciation to my mother and brothers for a very special kind of encouragement they showed throughout my entire college career.

To Ronnie my wife and friend, my children, Ellie, Christopher and Michael it would not have been possible without your love, support and understanding. I thank you from the bottom of my heart and I'm proud to be a part of you.

# TABLE OF CONTENTS

LIST O	F TABLE	S	rii:
LIST O	F FIGUR	æs	i
NOMENC	LATURE	·····	:111
CHAPTE	R	P.	AGE
1	INTROD	UCTION	. 1
	1.1 I	iterature Review	, 1
	1.2 P	resent Experiment	, 4
	1.3 D	evelopment of Facility	, <b>5</b>
	1.4 0	bjectives	, 6
2	EXPERI	MENTAL FACILITY	, <b>7</b>
	2.1 I	ntroduction	, <b>7</b>
	2.2	nlet Contraction Highlights	. 7
	2.3 1	he Boundary Layer Transition Module	, 8
	2.4 1	he Entrainment Module	10
	2.5 E	Receiver/Fan Room	12
	2.6	Computer Room/Labortory	12
3	Data A	Acquisition Facility	13
	3.1	Introduction	13
	3.2 I	Pressure Measurement Facility	13
	3.3	The Hot Wires	14
	3 4 1	Vicateoria Signal Conversion / Computer Resility	1.5

4	EXPE	RIMENTAL FACILITY AND PROCEDURE
	4.1	Introduction 17
	4.2	Excitation Nechanism
	4.3	Hot Wire Alignment and Calibration 19
		4.3.1 Low Velocity Calibration
		4.3.2 Straight Wire and Vorticity Probe Alignment
		4.3.3 Hot-Wire Calibration
		4.3.4 Hot-Wire Positioning For Boundary Layer Surveys 22
	4.4	Data Acquisition Strategy 23
		4.4.1 The Boundary Layer 23
		4.4.2 The Excited Mixing Layer 24
5	UPST	REAN BOUNDARY LAYER RESULTS AND DISCUSION 26
	5.1	Introduction 26
	5.2	Boundary Layer Mean Velocity Profiles 27
		5.2.1 Mid Plane Mean Velocity Profiles 27
		5.2.2 Test of the Three-Dimensionality of the Mean Velocity Profiles
		5.2.3 The Influence of Excitation on the Mean Velocity Profiles
		5.2.4 The Influence of Phase Time on the Mean Velocity
	5.3	Streamwise Component of Turbulent Intensity 32
		5.3.1 Mid Plane Turbulent Intensity Profiles 32
		5.3.2 The Three-Dimensionality of the Turbulent Intensity Profiles
		5.3.3 Influence of the Phase Time on the Turbulent Intensity Profiles

6	RESU	LTS OF THE EXCITED MIXING LAYER INVESTIGATION 34
	6.1	Introduction 34
	6.2	Spatial Distribution of the Phase Averaged Transverse Vorticity
	6.3	Phase Averaged Streamwise Velocity Profiles
	6.4	Perturbed Phase Averaged Transverse Vorticity Contours
	6.5	Temporal Evolution of the Phase Averaged Transverse Vorticity
	6.6	Quasi-Instantaneous Transverse Vorticity 43
7		USSION OF VORTICITY MEASUREMENTS IN AN TED MIXING LAYER
	7.1	Introduction 45
	7.2	Phase Averaged Streamwise Velocity 47
	7.3	Evolution of the Phase Averaged Transverse Vorticity
		7.3.1 Spatial Distribution of the Phase Averaged Transverse Vorticity
		7.3.2 General Temporal Evolution of the Coherent Vorticity Conours
	7.4	Global Evaluation of the Perturbed and Imperturbed $\langle \omega_z \rangle_i$ Contours
	7.5	Phase Averaged Transverse Vorticity Time Series 55
	7.6	Quasi-Instantaneous Transverse Vorticity 56
		7.6.1 Introduction 56
		7.6.2 Quasi-Instantaneous Transverse Vorticity Time Series
		7.6.3 Quasi-Instantaneous Transverse Vorticity Summary

8	NCLUSIONS 6	2
APPENDI	A CUBIC SPLINE END CONDITIONS 12	25
APPENDI	B STANDARD DEVIATION OF THE X-ARRAY VOLTAGES 13	35
APPENDI	C TEMPORAL EVALUATION OF VORTICITY CONTOURS 14	44
REFEREN	3S	<b>5</b> 3

# LIST OF TABLES

TABL	TABLE	
6.1	Designation of the Phase Avgeraged Time (i) for $\langle w_z \rangle_i$ Contours: Wi	
6.2	Designation of the Phase Avgeraged Time (i) for $\langle w_{\mathbf{Z}}^{\mathbf{D}} \rangle_{\mathbf{i}}$ Contours: WPi	
6.3	Phase Averaged Transverse Vorticity Time Series 43	
6.4	Quasi-Instantaneous Transverse Voricity 44	
<b>A.1</b>	Effect of Cubic Spline End Conditions on the Calculated Vorticity	
B.1	Standard Deviations For X-array	

# LIST OF FIGURES

Figu	ire	Page
1	Free Shear Flow Facility Floor Plan	64
2	Boundary Layer Transition Module and Test Section	65
3	Entrainment Module	66
4	Dual Cavity Throttling Chamber	67
5	Method of Entrainment Velocity Determination	68
6	Data Aquisition Facility	69
7a	The Vorticity Probe	70
7ъ	A Typical Hot-Wire Probe	71
8a	Excitation Mechanism (Isometric View)	72
8ъ	Excitation Mechanism (Side View)	73
8 c	Excitation Nechanism (Support Fixture)	74
9 <b>a</b>	Schematic Representation of Excitation Intensity Determination	75
9ъ	Schematic Representation of Excitation Placement and Movement	76
10a	Schematic Representation of Probe and Support Arm used for low speed calibration	77
10ъ	Schematic Representation of the Probe Positioning Unit	78
10c	Schematic Representation of the Traverse Mechanism	79
11	A Visual Representation of the Ensemble Averaging Technique	80
12	Schematic Representation of the Measurement Grid	81
13.	Clanear Plot of Data at X=-4 5 cm 7=0 0 cm	22

13ъ	Law of the Wall Plot of Data at X=-4.5 cm, Z=0.0 cm	83
14	Law of the Wall Plot of Data at X=-25 cm, Z=0.0 cm	84
15	Law of the Wall Plot of Data at X=-4.5 cm, Z=0.0, ±20 cm	8:
16	Law of the Wall Plot for Data at X=-4.5 cm, Z=0.0 cm, Excited and Unexcited	86
17	Law of the Wall Plot for Data at X=-4.5 cm, Z=0.0 cm; Phase Points: 1, 14, 28 and 42	87
18	Streamwise Component of Turbulent Intensity for Data at X=-4.5 cm, Z=0.0 cm, Excited and Unexcited	88
19	Streamwise Component of Turbulent Intensity for Data at X=-25 cm, Z=0.0 cm, Excited and Unexcited	89
20	Streamwise Component of Turbulent Intensity for Data at X=-4.5 cm, Z=0.0 cm, ±20 cm	90
21	Streamwise Component of Turbulent Intensity for Data at X=-4.5 cm, Z=0.0 cm; Phase Points: 1, 7, 14, 28 and 42	91
22	Phase Averaged Transverse Vorticity $\langle w_z \rangle_i$ ; Expanded Initial Region for W1	92
23	Phase Averaged Transverse Vorticity $\langle w_z \rangle_i$ ; a) W1 and b) W63	93
24	Phase Averaged Transverse Vorticity $\langle w_z \rangle_i$ ; a)W63 and b)W125	94
25	Phase Averaged Transverse Vorticity $\langle w_z \rangle_i$ ; a)W125 and b)W187	9:
26	Phase Averaged Transverse Vorticity $\langle w_z \rangle_i$ ; a) W187 and b) W227	96
27	Phase Averaged Transverse Vorticity $\langle \omega_z \rangle_i$ ; a) W227 and b) W289	97
28	Phase Averaged Transverse Vorticity $\langle \omega_z \rangle_i$ ; a) W289 and b) W320	98
29	Phase Averaged Non-dimensional Velocity Profiles; For Phase Point, i=320 and at X=24.4, 39.6, 54.9, 70.1, 85.4, 100.6, 115.8, 131.1, 146.3 cm	99
30	Phase Averaged Non-dimensional Velocity Profiles; at X=85.4 cm and i=1, 63, 125, 187, 227, 289 and 320	10(

31	Perturbed Phase Averaged Transverse Vorticity, $\langle \omega_{\mathbf{z}}^{\mathbf{p}} \rangle_{\mathbf{i}}$ ; a) WP1 and b) WP63	
32	Perturbed Phase Averaged Transverse Vorticity, $\langle \omega_{Z}^{p} \rangle_{i}$ ; a) WP63 and b) WP125	
33	Perturbed Phase Averaged Transverse Vorticity, $\langle \omega_{z}^{p} \rangle_{i}$ ; a) WP125 and b) WP187	
34	Perturbed Phase Averaged Transverse Vorticity, $\langle \omega_{z}^{p} \rangle_{i}$ ; a) WP187 and b) WP227	
35	Perturbed Phase Averaged Transverse Vorticity, $\langle \omega_{\mathbf{z}}^{\mathbf{p}} \rangle_{\mathbf{i}}$ ; a) WP227 and b) WP289	
36	Perturbed Phase Averaged Transverse Vorticity, $\langle \omega_{z}^{p} \rangle_{i}$ ; a) WP289 and b) WP320	
37a	Phase Averaged Transverse Vorticity Time Series at X=48.8 cm and Y= -7.3, -4.3, -1.2 and 1.8 cm	
37ъ	Phase Averaged Transverse Vorticity Time Series at X=48.8 cm and Y= 1.8, 4.9, 7.9 and 11.0 cm	
38a	Phase Averaged Transverse Vorticity Time Series at X=85.4 cm and Y= -7.3, -4.3, -1.2 and 1.8 cm	
38Ъ	Phase Averaged Transverse Vorticity Time Series at X=85.4 cm and Y= 1.8, 4.9, 7.9 and 11.0 cm	
39	Quasi-Instantaneous Transverse Vorticity at X=18.3 cm and Y= -4.3, -1.2 and 1.8 cm	
40	Quasi-Instantaneous Transverse Vorticity at X=18.3 cm and Y= -4.3, -1.2 and 1.8 cm	
41	Quasi-Instantaneous Transverse Vorticity at X=33.6 cm and Y= -4.3 and -1.2 cm	
42	Quasi-Instantaneous Transverse Vorticity at X=33.6 cm and Y= -4.3 and -1.2 cm	
43	Quasi-Instantaneous Transverse Vorticity at X=42.7 cm and Y= -4.3 and -1.2 cm	
44	Quasi-Instantaneous Transverse Vorticity at X=42.7 cm and Y= -4.3 and -1.2 cm	
45	Quasi-Instantaneous Transverse Vorticity at X=48.8 cm and Y= -4.3, -1.2 and 1.8 cm	

46	Quasi-Instantaneous Transverse Vorticity at X=51.9 cm and Y= -4.3, -1.2 and 1.8 cm
47	Quasi-Instantaneous Transverse Vorticity at X=58.0 cm and Y= -4.3, -1.2 and 1.8 cm
48	Quasi-Instantaneous Transverse Vorticity at X=61.0 cm and Y= -4.3, -1.2 and 1.8 cm
49	Quasi-Instantaneous Transverse Vorticity at X=79.3 cm and Y= -4.3, -1.2 and 1.8 cm
50	Quasi-Instantaneous Transverse Vorticity at X=134.2 cm and Y= -4.3, -1.2 and 1.8 cm
51	Velocity Isotach and Smoke Photography (Photograph 3, Taken From P. Mensing, Dissertation, 1981) 123
52	Streamwise Position of Saturated Structure Over 10.24 ms For Both the Unperturbed and Perturbed Data

# NOMEN CLATURE

A <sub>e</sub>	maximum displacement of excitation piston
A,B,n	coefficients for Collis and Williams equation
C	cubic spline coefficient
$\mathbf{c_f}$	local skin friction coefficient
đ	diameter of honeycomb
E	hot-wire output voltage
emax	maximum rms voltage
F	any property at a particular phase (or time)
fe	excitation frequency
f <sub>n</sub>	frequency of natural instability
i	a specific phase point of excitation cycle (the i counter varied from 1 to 320; this represents 0.1535 precent of a cycle)
K	Perturbation constant
1/d	length to diameter ratio of honeycomb
N	the total number of realizations
Q	velocity vector
Q,	velocity vector incident on wire 3
$\mathbf{Q_4}$	velocity vector incident on wire 4
Q <sub>x</sub>	velocity vector incident on X-array
r	radius
St <sub>s</sub>	Strouhal number based on the saturation length
St <sub>x</sub>	Strouhal number based on X

Strouhal number based on 0 Sta T period of excitation U local time mean streamwise velocity Uh average velocity of the back of the saturated structure Uf averave velocity of the front of the saturated structure. U free stream velocity of primary flow Ū. average saturated structure velocity U friction velocity U<sup>+</sup> dimensionless streamwise velocity U, upstream velocity at X=10 cm U. downstream velocity at X=290 cm u' streamwise velocity fluctuation local mean lateral velocity V V. entrainment velocity **v'** lateral velocity fluctuation X streamwise coordinate I initial streamwise position of probe X. saturation length Y lateral coordinate Yo initial lateral position of probe Y<sup>+</sup> dimensionless lateral displacement Z transverse coordinate ΔL distance saturated structure moves in At Δt time interval in which data was agguired δ boundary layer thickness

boundary layer displacement thickness

8

angle in the XY-plane between velocity vector γ and axis of X-array probe wavelength between newly formed and λ saturated vortex structure standard deviation quasi-instantaneous vorticity time step momentum thickness indicates a time averaged quantity quasi-instantaneous transverse vorticity wz <w\_> phase averaged transverse vorticity **〈 〉** phase or ensemble averaged quantity  $\langle \rangle_{i}$ with respect to a specific phase: i < >P this quantity has been perturbed summation d/dx derivitive with respect to X ∂⟨V⟩/∂x Spatial velocity gradient ∂⟨U⟩/∂y Spatial velocity gradient

# CHAPTER 1

#### INTRODUCTION

#### 1.1 Literature Review

In a natural (unexcited) free shear layer, vorticity from the boundary layer is continuously shed from a backward facing step. This vortical fluid tends to roll-up (or fold) and to form discrete vortices. The roll-up of the vortical fluid is a result of the natural instability process. For the free shear layer this instability is of the Kelvin-Helmholtz type. For convenience, these naturally occuring discrete vorticies are termed "unit vorticies" in the present discussion.

When periodic excitation is applied (at the separation lip) to a free shear layer, it causes a two-dimensional undulation of the separating boundary layer. This undulation is followed by the agglomeration of the shed vorticity into a large, isolated, vortical structure downstream from the separation lip (Fiedler, Dziomba, Mensing and Rosgen 1980 and Fiedler and Korschelt 1979). An efficient agglomeration may be accomplished by exciting the natural shear layer with a low frequency, long wavelength, periodic disturbance (Wygnanski, Oster and Fiedler 1979, Ho and Huerre 1984, Ho and Huang 1982).

In addition to agglomeration and non-linear increases in width, excitation has been found to organize and generate larger vortical structures than would exist in a naturally occuring shear layer. This organization is a result of the vortical structure being "locked" in space with respect to a particular phase (or time) of the excitation mechanism (Wygnanski, Oster and Fiedler 1979 and Fiedler, Korschelt and Mensing 1978). Using temperature as a passive contaminant, Fiedler and Korschelt (1979) measured the transverse space correlation of the temperature fluctuations in a two-dimensional jet. These results reveal a dramatic increase in the transverse spatial correlation and hence in the two-dimensionality of the excited case versus the natural shear layer.

These large vortical motions (or structures) are often referred to as "coherent structures". Hussain (1983) defines a coherent structure as "a connected, large-scale, turbulent fluid mass with phase-correlated vorticity over its spatial extent. That is, underlying the three-dimensional random vorticity fluctuations characterizing turbulence, there is an organized component of the vorticity which is phase correlated (i.e., coherent) over the extent of the structure".

The coherent structure properties can be educed by using phase averaging. Phase averaging is defined by the following operation:

$$\langle F(X,Y,Z,i) \rangle = \lim_{N \to \infty} 1/N \sum_{n=1}^{N} F(X,Y,Z,nT+t_i),$$

where  $t_i$  is the time corresponding to a specific phase point (i) and T is the period (Hussain 1970, Reynolds and Hussain 1970).

In the foundation work of Mensing (1981), the suppression of pairing of the large, isolated, vortical structures was obtained when the single stream shear layer was weakly excited. Specifically, the mixing layer is said to be weakly excited when a low frequency disturbance is introduced into the flow with an excitation intensity of,

$$[\overline{v}^{,2}]^{1/2}/\overline{v}_0 \le 0.0078.$$

Under these conditions Mensing found that the subharmonic energy remained approximately one order of magnitude below the energy of the fundamental mode of the structure; this observation reveals that the pairing process, of the large scale motions, is suppressed for these conditions. In addition, Mensing determined that for the case of a weakly excited flow, the vorticies would reach their maximum periodic energy level (become saturated) when the Strouhal number, St<sub>g</sub> based on X is approximately equal to 1. The downstream distance where this occurred is referred to as the saturation length (Feidler, Dziomba, Mensing and Rosgen 1980, Feidler and Mensing (1982), Mensing 1981).

## 1.2 The Present Experiment

In the present study the global vorticity distribution in an excited, plane, mixing layer was investigated. The simplest turbulent flow field in which this could be carried out was a non-reacting, single phase, isothermal, two-dimensional, incompressible mixing layer. The single stream mixing layer, which has a greater spread rate and requires a shorter downstream distance to fully evolve (as compared to that of a two-stream mixing layer) was selected for the present work.

There are many ways to introduce a periodic perturbation into the flow; among these are: the oscillating flap (Oster and Wygnanski 1982), the vibrating ribbon (Zaman and Hussain 1981) and a loudspeaker (Feidler, Korschelt and Mensing 1978 and Zaman and Hussain 1981). In the present study a new method, the reciprocating piston, was used to excite the mixing layer. This method assures a truly two-dimensional as well as a periodic perturbation (see section 4.2).

In the present investigation, an excitation intensity of 0.00537 and a Stroubal number,  $St_s$  (the expected location of the saturated structure) of 0.97 were selected based on Mensing's finding. Setting the excitation frequency,  $f_e$ , equal to 15 Hz, the saturation length  $X_s$  was determined to be 84 cm for a free stream velocity of 13 m/s. In addition, the approximate number of vorticies that would agglomerate was calculated based on the frequency of the natural instability,  $f_n$ . Based on the existence of a turbulent boundary layer, the following

mixing layer relationship is used to relate  $f_n$  to the momentum thickness,  $\theta$ ;

$$St_{\theta} = f_n + \theta/U_0$$

where  $\mathrm{St}_{\Theta}$ =0.024 (Drubka 1981 and Hussain and Zaman 1981) and  $\mathrm{U}_{\mathrm{O}}$  the free stream velocity. Once  $\mathrm{f}_{\mathrm{n}}$  is obtained, the ratio  $\mathrm{f}_{\mathrm{n}}/\mathrm{f}_{\mathrm{e}}$  can be computed and is approximatly equal to the number of unit vorticies expected to roll-up and form a large, vortical structure. In the present investigation approximately three unit vortices would agglomerate.

# 1.3 Development Of The Facility

In an effort to ensure high quality measurements in the present investigation, a flow facility was designed and constructed to provide the following conditions:

a) the ability to control the flow rate and disturbance level of the entrainment flow. The objective was to ensure that the entrainment flow was essentially irrotational. (This capability required the careful setting of the entrainment flow rate as described in chapter 2.)

b] a universal turbulent boundary layer at the separation lip.

# 1.4 Objectives

The primary goal of this study was to record and interpret the global distribution of phase averaged vorticity in the formation, saturation and decay regions in an excited, single-stream, free shear layer. In addition, both quasi-instantaneous and coherent transverse vorticity time series throughout the mixing layer were to be obtained and interpreted. A secondary objective of the study was to provide a test case for computer simulations of developing shear flows. The careful documentation of the turbulent boundary layer and the detailed vorticity measurements throughout the mixing layer will serve this objective. The detailed documentation of the flow field includes:

- 1) the determination of the relative magnitudes of the quasi-instantaneous transverse vorticity fluctuations in the non-linear, formation, saturation and decay regions of the weakly excited mixing layer.
- 2) the comparison of the quasi-instantaneous transverse vorticity to the transverse coherent vorticity in the non-linear, formation, saturation and decay regions of the excited mixing layer.
- 3) the affect of weak excitation on the upstream turbulent boundary layer.

#### CHAPTER 2

#### EXPERIMENTAL FACILITY

#### 2.1 Introduction

A novel single stream, free shear layer flow facility was designed and constructed for the present study. From the floor plan, Figure 1, one can see a large suction tunnel which occupies the complete laboratory (6.81 m x 26.34 m). The volume between the fan outlet and the inlet of the zeroth contraction serves as a high pressure (P = atmospheric pressure) settling chamber. The details of the flow facility are outlined below.

# 2.2 Inlet Contraction Highlights

The overall contraction ratio (the inlet area of the zeroth contraction divided by the entrance area of the test section) is 22.6:1. The fluid entering the zeroth contraction is accelerated toward the test section through three, two-dimensional contractions. The first two, the zeroth and the first contractions, are symmetric. They accelerate the fluid in the XY and XZ-planes, respectively. Upon exiting the first two stages of contraction and before proceeding through the final contraction, the fluid is passed through the primary

turbulence manipulator section. The design of the primary and entrainment turbulence manipulators was based on the work of Loehrke and Nagib (1972 and 1976). In their work, the specific combination of an 1/d=8 honeycomb (d=3.175 mm) and multiple 30 mesh screens were found to considerably reduce the disturbance level of the exiting flow. Five screens, spaced at a distance of 12.7 mm, were used to control the turbulence level upstream of the final contraction. The final asymmetric contraction, in the XY-plane and with an area ratio of 3.22:1, accelerates the fluid downstream. This contraction stage delivers the primary flow to the Boundary Layer Transition Module (BLT).

# 2.3 The Boundary Layer Transition Module

The BLT is a constant area duct (50 cm x 80 cm), with one of its vertical side walls serving as the boundary layer conditioning surface. This surface manipulates the boundary layer before it separates from the backward facing step. The step (or separation lip) is the location where the mixing layer originates; this location also serves as the entrance to the test section. The conditioning of the boundary layer before it reaches the separation lip is a two-stage process. First, to ensure that unwanted effects i.e., Gortler and corner vortices, are prevented from reaching the test section, the boundary layer leaving the second contraction and approaching the BLT is removed. This is accomplished by using a separate fan, throttling valve and splitter plate. The splitter plate diverts the boundary layer fluid exiting from the second contraction and exhausts this

unwanted fluid into the receiver. The plate has a parabolic leading edge (constructed from a redwood board) which has been fastened to the step side vertical wall. The leading edge and step side wall is displaced 2 cm inward (in the negative Y direction) towards the center of the primary flow. After the unwanted boundary layer is removed, the remaining flow continues over the leading edge and trip mechanism. A tripping mechanism is used to artificially thicken the boundary layer. In the present work, a number 16 open grit sandpaper was selected. Specifically, the sandpaper was located on the step side vertical wall immediately downstream of the leading edge and extended downstream for 60.5 cm (Figure 2). Choice and placement of the trip was based on the work of Klebanoff and Diehl (1951) who obtained a self-similar, mean velocity profile 170 cm downstream from the leading edge. The boundary layer continues to grow another 129 cm downstream before encountering the separation lip. The final 65.5 cm of the vertical wall upstream of the separation lip was constructed using Formica covered flakeboard. The motivation for this wall construction is as follows:

a) The low thermal conductivity will minimize erroneous hot wire readings resulting from the additional heat loss to the wall. This extra heat loss can occur when the hot wire probe is brought into close proximity to the surface under investigation. For non-conducting materials (materials with a low thermal conductivity), such as Formica covered flake-board, the additional heat loss from the measurement probe to these surfaces is much smaller and can be considered

negligible for most practical boundary layer measurements (Bhatia, Durst and Jovanovic, 1982).

b) The highly reflective Formica surface allows the use of an optical method in which the distance between the hot-wire and the wall can be accurately estimated (see section 4.3.4).

# 2.4 The Entrainment Module

The mixing layer, formed by a separating boundary layer, spreads laterally as it moves downstream in the test section. This lateral spread is associated with the entrainment of the surrounding fluid. In the present design, irrotational fluid is continually drawn into the test section from the laboratory. That is, an irrotational entrainment stream is introduced into the test section and a centrifugal fan (Chicago Blower, number 36.5 SQA Airfoil Fan) returns the primary and entrainment flows to the laboratory from the receiver. This entrainment fluid must pass through the entrainment module and the entrainment turbulent manipulator section (Figure 3) before being engulfed and ingested into the mixing layer. This is in contrast with a conventional single stream free shear flow facility in which previously sheared fluid is re-entrained in the test section without passing through the turbulence manipulators. In a conventional facility, the level of residual vorticity in the entrainment stream increases to an equilibrium level for the laboratory. The disturbance level in a conventional tunnel cannot be controlled since the entrainment fluid is not passed through the turbulent manipulators. It is

this feature of the present facility that justified the time and expense for its development.

The entrainment module was designed to provide a time independent, irrotational entrainment flow, with a constant velocity equal to that found in a natural mixing layer. This module consists of 155 flow conditioning units (each unit is a Dual Cavity Throttling Chamber: DCTC, Figure 4) followed by the entrainment plenum (a large settling chamber). The entrainment plenum is 2.44 m in height and 3.0 m in streamwise length. The DCTC is composed of two cavities which allow for the deceleration and the decay of the turbulent kinetic energy of the incoming flow. The flow rate is controlled by a slide mechanism on the front of the DCTC which adjusts the entrance cross sectional area; see Figure 4. Equalization of the flow non-uniformities can occur in the entrainment plenum before undergoing a 3.05:1 sudden contraction into the entrainment turbulent manipulator section.

The entrainment flow rate was set such that the primary core flow passing through the test section experienced little or no streamwise acceleration ( $dU_0/dX=0$ ; see Figure 5 for measurement locations). Adjusting the slide mechanism on the DCTC's, the velocity difference  $[(U_2-U_1)/U_1]$  was minimized to less than 1 % at the measured points ( $U_2$  is greater than  $U_1$  by approximately 1 %). Placing a hot wire 112 cm downstream from the separation lip and approximately 2 cm away from the last entrainment screen, a dimensionless entrainment velocity,  $V_e/U_0$  of 0.0395 was measured (see section 4.3.1 for the calibration

technique). This is in good agreement with the measured value of  $V_e/U_o = 0.042$ , which was experimentally determined by Fiedler and Theis (1982) in a conventional flow facility.

#### 2.5 Receiver/Fan Room

The combined primary and entrainment flows exit the test section and enter the receiver, which serves as a low pressure plenum. This plenum allows for the isolation of the test section from pressure fluctuations originating at the fan; that is, the fluctuations that would be associated with the blade passing frequencies or rotor instabilities. The fan returns the primary plus the entrainment air to the laboratory as mentioned earlier.

#### 2.6 Computer Room/Laboratory

The laboratory also houses a computer room where a PDP 11/23 and various units of electronic instrumentation are located. This room is pressurized and air conditioned. The flow facility has been constructed using vibration isolators, thereby minimizing the possibility of any disturbance being transmitted to the test section while data taking is in progress. In addition, the computer room, viewing platform and the fan have been constructed and installed with vibration isolation in mind. Specifically, any disturbances originating at these locations must first be transmitted through plywood vibration absorbers and the concrete floor of the laboratory before being transmitted to the test section structure.

#### CHAPTER 3

# DATA ACQUISITION FACILITY

# 3.1 Introduction

In the present study, direct velocity measurements were made with the use of hot-wire anemometry. A pitot-static pressure probe was used to monitor the tunnel speed and the hot wires were used to investigate the velocity at specific locations in the boundary layer or the mixing layer. The data acquisition facility used for the mixing layer investigation is shown in Figure 6.

# 3.2 Pressure Measurement Facility

The pressure probe was mounted from the ceiling of the test section at X=15 cm and Y=-25 cm. A Validyne DP45-22 pressure transducer and CD12 transducer indicator were used to measure the difference between total and static pressure.

#### 3.3 The Hot Vires

All hot-wires were operated in the constant temperature mode. A straight wire was used for boundary layer surveys and a four-wire array (vorticity probe) was used in the mixing layer invesigation. The four-wire array is composed of: an X-array and a parallel array (Figure 7a). This probe, and its processing algorithms, are extensively described in Foss, Klewicki and Disimile (1984). The X-array is composed of two slant wires (in the XY-plane), which are placed at nominal angles of ±45 degrees with respect to the probe axis and which are separated by approximately 1 mm. A parallel array is located below the X-array by a distance of approximately 3.8 mm in the Z-direction and the two parallel wires are separated by a distance of 1.27 mm. The location of the X-array is such that the active portion is placed directly above the mid-point of the parallel array. hot-wire probes were fabricated using 5 micron (diameter) tungsten wire. The ends of the tungsten wire were copper plated. The copper plating enables the wire to be soft-soldered to the tips of the jeweler's broaches (prongs, see Figure 7b) and it serves to isolate the active portion from the aerodynamic disturbance effects of the prongs. Although the wire was nominally 3 mm in length, the active portion was only 1 mm long. The hot-wires are connected to a bridge circuit incorporated in the DISA 55M01 anemometers and were set up with a heating ratio of 1.7.

## 3.4 Electronic Signal Conversion/Computer Facility

The analog outputs of the four anemometers were input to a TSI 1075X, 4 channel, simultaneous sample and hold analog-to-digital (referred to as A/D) converter. This 12 bit A/D converter has an input range of approximately 0 to +5 volts and a resolution of 1.2 millivolts (that is, one least significant bit, LSB is equivalent to 1.2 millivolts). Connecting all four channels to a common signal, the A/D was found to have an accuracy of ±2.4 millivolts (2 LSB's). All four channels have matched 50 kHz low pass input filters. Also, this A/D is equipped with a Direct Nemory Access (DMA) interface. With a DEC DEV11-B interface module and DMA, the transfer of data directly between the A/D and system memory can be accomplished. Once programmed, this operation occurs without micropressor intervention.

Once the A/D is preprogrammed (i.e., specification of starting channel, number of channels, number of samples and sampling rate) digitizing of the data can be initiated by either software control or external triggering. When the external trigger mode is chosen, control of the A/D is transferred to an external device. This device can actuate the A/D on the occurrence of a specific event. This feature of the facility was used in order to provide phase sampled measurements; the specific features of the phase sampling are described in section 4.4.

The data acquisition system includes a computer/manual controlled traversing mechanism (Figure 10c). This system allows a probe to be

moved in the XY-plane and to rotate about a Z-axis. Three stepper motors are used to drive the traverse. Communication between the motors and the computer takes place through the DEC DRV11 interface module.

The DEC DRV11 and the DRV11-B interface modules are installed in a Charles River Data Systems PDP 11/23 microcomputer. All data are stored on a Digital RL02 10 megabyte hard disc.

### CHAPTER 4

### EXPRRIMENTAL FACILITY AND PROCEDURE

### 4.1 Introduction

This chapter is divided into three sections: Excitation Mechanism. Hot Wire Alignment/Calibration and Data Acquisition Strategy.

### 4.2 Excitation Mechanism

In the present investigation, periodic excitation of the separating, turbulent boundary layer was required. To accomplish this, an excitation mechanism was designed using a flat, rectangular piston moving in simple harmonic motion (see Figures 8a, 8b and 8c). This reciprocating motion was in the ± Y-direction (Figure 9a). The piston was located immediately downstream of the separation lip (Figure 9a and 9b). The excitation frequency, f<sub>e</sub>, was set at approximately 15 Hz. Fiedler and co-workers have shown that a precise frequency contol is not required since the shear layer response is the same over a wide range of frequencies. Hence, a hand adjusted, electronic motor speed control was used to set the frequency to the nominal value of 15 Hz.

The simple harmonic motion, experienced by the piston, is a consequence of the approximately elliptical path travelled by the shoulder bolt (Figure 8a). The shoulder bolt fastens the connecting rod to the eccentric support fixture, which in turn is connected to the concentric support fixture. This fixture is able to communicate to the motor through the rotating shaft and the drive arrangement shown in Figure 8a. Selection of various eccentric support fixtures discretize the allowable excitation amplitude A (the maximum displacement of the piston). In addition, a "trip arm" is placed in between the eccentric and concentric support fixtures. The trip arm, in conjunction with an infrared optical encoder, was used to actuate the A/D converter. This is accomplished by allowing the trip arm to rotate and interrupt the infrared beam within the optical encoder. The arm is oriented such that the interruption of the infrared beam indicates the relative position of the excitation mechanism. Specifically, the interrupt signal corresponds to the first phase point (or sample). This is equivalent to an angular position of 90 degrees in the excitation piston cycle (Figure 9a).

For the present work, the shoulder bolt was located off-center at R=0.762 mm (the maximum displacement of the piston). At a rotational speed of 15 Hz, this offset gives an excitation intensity of:

$$\left[\frac{1}{V}, \frac{1}{2}/U_0^2\right]^{1/2} = 0.0039$$

A second evaluation of the excitation intensity was provided by a hot-wire anemometer probe. The probe was positioned at X=1.5 cm,

Z=0.0 cm and Y=2.5 cm (i.e., a displacement of approximately 13.3 mm into the excitation channel entrance Figure 9b). Setting the tunnel to the actual test conditions ( $U_0=13$  m/s and  $f_e=15$  Hz) the excitation intensity of:

$$\left[\frac{1}{V}, \frac{1}{2}, \frac{1}{U_0^2}\right]^{1/2} = 0.00537$$
 was obtained

Considering the difficulties in obtaining an accurate calibration of the hot-wire at very low velocities and the inherent problems of interpretting a hot-wire signal in an oscillatory flow, the agreement between these two values is acceptable. These results are interpretted to imply that the actual excitation intensity is nominally 0.0046.

# 4.3 Hot Wire Alignment and Calibration

### 4.3.1 Low Velocity Calibration

A low velocity calibration technique was used to obtain calibration coefficients for use in the measurement of the entrainment velocity. The schematic showing the setup used in this technique is shown in Figure 10a; it makes use of the rotating probe support arm capability in order to obtain relative motion between the probe and the stationary air. In this technique, the hot wire was positioned on the probe support arm, normal to the direction of motion and diplaced a distance r away from the traverse pivot point (Figure 10a). Specifically, with the fan shut off (no primary or entrainment air flow) the probe support arm was rotated (through an angle of approxi-

mately 180 degrees) about the pivot point at a constant speed. Optical devices, placed at preselected angular positions ( $\Delta\gamma \simeq 80$  degrees), allowed the detection of the probe passage. The signals obtained from the optical devices were input to the computer together with the output voltage of the hot-wire. With the use of software, the time interval ( $\Delta t$ ) was computed. The velocity, experienced by the hot-wire probe, was determined from the relationship,

 $U = r + \Delta \gamma / \Delta t$ 

where r is the radial position of the hot-wire probe from the axis of rotation of the traverse device. Repeating this process several times at various speeds of rotation and fitting the data to the Collis and Williams (1959) equation, calibration coefficients were obtained for the low speed range: 0.32 m/s < U < 1.077 m/s.

### 4.3.2 Straight-Wire And Vorticity Probe Alignment

Alignment of the hot-wire probe for the boundary layer investigations was performed with the use of a surveyor's transit. In addition, the transit was used to align the four-wire array. The parallel array used in the vorticity probe was aligned to ensure a vertical orientation (wires in the XZ-plane).

The vorticity probe, which contains both an X-array and a parallel array, was aligned such that the X-array (horizontal and in XY-plane) was perpendicular to the parallel array (residing in the IZ-plane). In addition, the active portion of the X-array is placed directly over the center of the parallel array. The parallel array was then positioned such that the distance between its two straight wires and the Z-axis extending up from the pivot point of the traversing mechanism were equal, when viewed through the transit. To ensure that the center of the vorticity probe is directly over the pivot point of the traverse mechanism, the probe support arm and probe assembly was rotated to +90 and -90 degrees (Figure 10b). At each angular position, the distance between the plane occupied by the parallel array (only one wire visible when probe is positioned at ±90) and the Z-axis extending up from the pivot point are set to zero. This is accomplished by adjusting the support arm and the probe assembly (along the radii extending out from the pivot point axis). Once the hot-wires were aligned, the calibration procedure could begin.

### 4.3.3 Hot-Wire Calibration

An additional calibration of a straight wire and the vorticity probe were conducted in the test section, at X=15 cm, Y=-25 cm, Z=0 cm. At this location, the inviscid core flow occupies approximately the central 40 cm of the flow. The tunnel speed was monitored with a pitot static probe. For a single straight wire calibration, the hot wire voltage and tunnel speed were recorded for seven tunnel settings. The data were then made to fit the generalized Collis and Williams equation,

 $E^2 = A + B + Q^n$ 

where Q is the velocity; A, B and n are constants. Selection of n is based on the minimization of the standard deviation (of Q) obtained using a least squares fit to the data. In a similar manner the four hot wire voltages of the vorticity probe were recorded at a constant tunnel speed while the vorticity probe was rotated through 13 angles:

 $\gamma = -42, -36, -30, -24, -18, -12, 0, 12, 18, 24, 30, 36, 42.$ 

This procedure was repeated for seven fan settings. The calibration of the vorticity probe was obtained using the recently completed four-wire calibration procedure developed by C.L.Klewicki (1983).

## 4.3.4 Hot-Wire Positioning For Boundary Layer Surveys

Once the single straight wire probe was aligned and calibrated and before the boundary layer surveys could be conducted, the determination of the initial lateral position: Y<sub>O</sub>, of the probe mwas obtained. Using an optical technique, Y<sub>O</sub> could be accurately estimated. This was obtained by moving the probe close to the wall, determining the effective distance between the reflection of the hot-wire support prongs (as seen in the Formica) and the actual support prongs. When these prongs and their mirror image coincide, the prongs are touching the wall. With the knowledge that the hot wire is mounted at the center of the prong tip and the diameter of the prongs at the tip is 0.20 mm for the present probe, Y<sub>O</sub> was determined to be 0.10 mm.

# 4.4 Data Acquisition Strategy

Data were recorded in the upstream boundary layer with a straight wire probe for both the excited and unexcited cases. In addition, the vorticity probe was used to record data in the excited mixing layer.

### 4.4.1 The Boundary Layer

In the boundary layer, hot-wire surveys (probe traversing laterally in the Y direction) were conducted at X=-4.5 cm (upstream from the separation lip) at Z=0,  $\pm 20$  cm and upstream at X=-25 cm and Z=0 cm. All boundary layer investigations were conducted with a free stream velocity  $U_0$  of nominally 13 m/s (as recorded by the pitot-static probe, section 3.2).

Data was acquired using the computer controlled traversing mechanism (described in chapter 2) and appropriate software. The specific software used in the boundary layer investigations depended on whether the boundary layer was excited or natural. In either case the measurement locations were the same. The probe was indexed laterally (from Yo and in the negative Y direction) through a total of 35 measurement locations to a final position of negative 7.86 cm (away from the step side wall). The measurement probe, initially located at Yo, was indexed as follows: the first 13 positions were incremented in intervals of 0.4 mm, the second 9 positions were incremented in intervals of 0.813 mm and the last 13 were incremented in intervals of 5.0 mm.

Ten thousand (10,000) samples were obtained at each of the 36 Y locations in the unexcited case; these data were acquired over a time period of 10.24 seconds at a sampling rate of 977 Hz. The resultant time series is then averaged over the 10.24 second time period; the mean voltage and its variance were obtained.

In the excited case, the data acquisition was initiated upon interruption of the infrared beam of the optical encoder as described in section 4.2. Specifically, at any Y-location an ensemble was created consisting of 1000 realizations (the begining of a realization is marked by the rotation of the trip arm past the detection mechanism). Each realization consisted of 56 samples (a time series 57.3 ms long) and were recorded at a sampling rate of 977 Hz. Once an ensemble was obtained, phase averaging (or an ensemble average taken with respect to a specific excitation phase angle) was performed. To obtain a phase average, the first sample (or phase point) of each time series would be added together and an average value determined for that phase point. Repeating this process for all remaining phase points, one obtains a phase averaged time series (Figure 11).

### 4.4.2 The Excited Mixing Layer

In the excited mixing layer, all the data were acquired using the vorticity probe. Although triggering of the A/D was accomplished by the identical method used in the excited boundary layer case, the sampling rate and the number of samples differed. A measurement grid of 414 node points was established. The rectangular grid was defined by

9 lateral Y locations: -7.3 \( \times \) 17.1 cm and 46 X (or streamwise) locations: 12.25 \( \times \) X \( \times \) 149.41 cm; see Figure 12. All mixing layer information was phase sampled with a sampling rate of 31.25 kHz. The data were then stored in two fashions: 1) a phase averaged time series (an ensemble average of 1000 events, see figure 11) and 2) 30 instantaneous time series. Each phase averaged time series is 320 samples (or 10.24 ms) long. All but two X-planes of the instantaneous time series are 80 samples (or 2.56 ms) long. The X=42.73 cm and X=45.78 cm mixing layer traverses are 320 samples (or 10.24 ms) long. The shortened instantaneous time series were a result of a typing error in the data acquisition software.

### CHAPTER 5

### UPSTREAM BOUNDARY LAYER RESULTS AND DISCUSSION

### 5.1 Introduction

Hot-wire traverses throughout the boundary layer were performed in order to determine the universality of the present turbulent boundary layer. The boundary layer data were processed and plotted in law of the wall coordinates  $(U^+,Y^+)$ , where

$$\overline{U}^+ = \overline{U}/\overline{U}_{\tau}$$
 and  $Y^+ = Y + \overline{U}_{\tau}/\nu$ 

where  $U_{\tau}$  is the friction velocity. Using a standard technique known as the Clauser plot (Clauser 1954), the data was plotted as  $U/U_{\rm O}$  versus  $Y^{*}U_{\rm O}/\nu$  and compared with the law of the wall. A value for the friction velocity  $U_{\tau}$  can be determined by using,

$$\mathbf{U}_{\tau} = \mathbf{U}_{\mathbf{0}} \left[ \mathbf{C}_{\mathbf{f}} / 2 \right]^{1/2}.$$

That is, the universal (law of the wall) curve can be replotted as a universal family of curves with the local skin friction coefficient,  $\mathbf{C}_{\mathbf{f}}$ , as a parameter. The value of  $\mathbf{C}_{\mathbf{f}}$  is chosen by selecting the appropriate member from the family of curves which best fits the

acquired data near the wall. A typical Clauser plot is shown in Figure 13a.

In addition to the local mean velocity  $\mathbf{U}$ , the streamwise component of turbulent intensity was calculated and plotted against  $\mathbf{Y}/\delta$ , where  $\delta$  is the boundary layer thickness. The value of delta was approximated by 10 theta where the momentum thickness,  $\theta$  was obtained from

$$\theta = \int_{\bullet}^{\infty} \overline{U}/U_{0}(1-\overline{U}/U_{0}) dY$$

using Simspon's Rule for the numerical integration and the discrete  $\overline{U}(Y)$  values. The displacement thickness,  $\delta^{*}$  is determined using,

$$\delta^{\bullet} = \int_{\bullet}^{\infty} (1 - \overline{U}/U_{0}) dY$$

and Simspon's Rule of numerical integration.

- 5.2 Boundary Layer Mean Velocity Profiles
- 5.2.1 Mid Plane Mean Velocity Profiles

The friction velocity was determined for the first phase point of the excited boundary layer case, see Figure 13a. The insensitivity of the mean velocity profiles to the phase point is dicussed in section 5.2.4. The data were obtained at a location upstream from the separation lip (X=-4.5 cm) at Z=0.0 cm. The values of  $C_f$  and  $U_\tau$  that were

determined for these conditions, are 0.0029 and 0.506 m/s, respectively. A comparison of the above Clauser plot to the one obtained for the unexcited case (not shown) shows negligible differences: namely,  $C_f$  and  $U_r$  were equal to 0.00285 and 0.501 m/s, respectively.

Once  $U_{\tau}$  was determined, the boundary layer data were replotted in law of the wall coordinates ( $U^{+},Y^{+}$ , Coles 1962,1968), as shown in Figure 13b for the excited case. These data show very good agreement with the law of the wall (Cole's line),

$$U^+ = 5.6 \log_{10} Y^+ + 4.9$$

in the log law region. The momentum thickness was determined to be 6.43 mm and the displacement thickness 8.83 mm for the excited case. This corresponds to a shape factor of approximately 1.37. In the unexcited case  $\theta=6.53$  mm and  $\delta^{0}=8.99$  mm corresponding to a shape factor of 1.38. In addition,  $u'/U_{\tau}$  is approximately equal to 2.57 for the unexcited case and 2.63 for the excited case. These results show that Two additional characteristics of a fully-developed turbulent boundary layer have also been satisfied: a shape factor of 1.4 and  $u'/U_{\tau}=2.5\pm0.25$  (Hussain, 1983).

The upstream boundary layer at X=-25 cm and Z=0 cm, Figure 14, has a shape factor,  $u'/U_{\tau}$  and  $C_f$  equal to 1.43, 2.68 and 0.0026 for the excited case, similarily 1.42, 2.80 and 0.0027 for the unexcited case. Comparing this upstream boundary layer to the boundary layer at the separation lip (X=-4.5 cm) one can observe the following: the

upstream boundary layer exhibits an overshoot in the wake region and fair agreement in the log region.

# 5.2.2 Test Of The Three-Dimensionality Of The Mean Velocity Profiles

additional boundary layer traverses were obtained at the same upstream location (X=-4.5 cm) but were displaced in the transverse direction along the surface of the step side plate. These traverses were used to examine the three-dimensionality of the boundary layer. This information was processed in the same manner (Clauser plot to determine  $U_{\tau}$ ) and plotted in law of the wall coordinates. The additional lateral traverses were obtained at Z=±20 cm (see Figure 15). The agreement between the three traverses and Cole's line in the law of the wall region is good. Comparison of the momentum thickness,  $\theta$  shows a maximum difference of 10 % between the three Z traverses.

It is inferred that the variation in theta is associated with the specific technique that was used to artifically thicken the boundary layer. Specifically, randomly distributed roughness elements (sandpaper) were used to create the desired boundary layer thickness. This method of producing an artifically thickened turbulent boundary layer is known to generate greater three-dimensionality in the mean properties than other tripping tripping mechanisms (Preston, 1958).

It should be noted that the objectives of the present research required a relatively large value for the momentum thickness. This would enable the excitation mechanism to produce the largest structure

possible at the selected value of  $f_{\rm e}$ . The reported three-dimensionalities are considered to be acceptable in the context of the objectives of the present investigation.

### 5.2.3 The Influence Of Excitation On The Mean Velocity Profiles

A comparison between the excited and unexcited turbulent boundary layer profiles obtained at (X,Y,Z) = (-4.5,Y,0.0) cm are plotted in law of the wall coordinates (Figure 16). Again, good agreement is found in the log law region; however, if attention is directed towards the outer (or wake) region of the boundary layer, a difference between the two cases can be detected. That is, the mean velocity profile in the excited case undershoots the mean velocity profile in the unexcited case in the outer region. This undershoot of the mean velocity profile indicates a reduction in  $\Theta$  in the excited boundary layer case. This reduction is approximately 2% based on the calculated momentum thickness. A number of additional boundary layer traverses were recorded during the setting of the boundary layer bleed flow and all surveys consistently showed a decrease in theta for the excited case from 1.5 to 8 percent. In the boundary layer traverse at X=-25 cm, the velocity profile in the excited case is observed to undershoot that in the unexcited case in the wake region. A corresponding 3% drop in 0 has been found (Figure 14).

Based on the observed effects of a low frequency, periodic excitation when applied to a free shear layer, a possible explanation for the decrease in theta in the turbulent boundary layer is presented. A known feature of periodic excitation is its ability to organize and generate large vortical motions periodically spaced in time. That is, the naturally shed vortices from the separation lip are agglomerated and regulated in space. It is hypothesized that the effect of this periodic flow interruption propagates upstream of the separation lip, tending to reduce the chaotic state of the flow by organizing and separating the large eddies present in a turbulent boundary layer.

### 5.2.4 The Influence Of Phase Time On The Mean Velocity

To examine the affect of the excitation phase angle on the mean velocity profiles, four phase points spanning the total excitation cycle were selected for comparison. These phase points are: 1,14,28 and 42; they are related to the position of the excitation mechanism throughout one complete cycle (Figure 9a). In Figure 17, the upstream traverse taken at Z=0 cm is shown for six phase points. Although some scatter exists in the data no significant variations appear. This indicates that the effect of phase position of the excitation mechanism on the mean velocity profiles is negligible.

- 5.3 Streamwise Component of Turbulent Intensity
- 5.3.1 Mid Plane Turbulent Intensity Profiles

The streamwise component of turbulent intensity,

$$\left[\frac{\pi}{u}, \frac{1}{2}/U_0^2\right]^{1/2}$$

in the boundary layer is plotted against Y/5, where  $\delta$  (= 10  $\theta$ ) is the boundary layer thickness. In all plots of the excited turbulent intensity profiles the first phase point has been used. In Figure 18, both an excited and an unexcited boundary layer traverse, taken upstream of the separation lip (X=4.5 cm) at Z=0 cm, are shown. No major differences were found between the two cases except at Y/5 greater than 1. In addition, the streamwise component of turbulent intensity for the last measurement point in the unexcited case is 0.5%. The boundary layer traverses obtained at X=-25 cm for the excited and unexcited cases (Figures 19) shows slight data scatter for Y/5<0.7.

## 5.3.2 The Three-Dimensionality Of The Turbulent Intensity Profiles

To indicate the degree of three-dimensionality in the turbulent intensity, the three traverses for the excited case are plotted in Figure 20. They were taken at the same X-location, X=-4.5 cm and at Z=0,+20 and -20 cm. Again, the curves show good agreement except when Y/8 is greater than 1. This effect is apparently due to the variation in the free stream turbulent intensity.

# 5.3.3 Influence Of The Phase Time On The Turbulent Intensity Profiles

To assess the affect of the phase time (point) of the excitation mechanism on the streamwise component of turbulent intensity, the profile obtained at X=-4.5 cm and Z=0 cm was replotted in Figure 21 with four additional phase points: 7,14,28 and 42. Considerable scatter is found among the various phase points when Y/5 exceeded 0.8.

### CHAPTER 6

### RESULTS OF THE EXCITED MIXING LAYER INVESTIGATION

### 6.1 Introduction

This chapter presents the scheme used for processing the data and the results which have been obtained for the excited mixing layer; see chapter 7 for the discussion of the results.

All results presented in this chapter have been obtained by processing the data acquired using the four-wire array (i.e., the vorticity probe shown in Figure 7a and described in section 4.3.2). These data were obtained over a rectangular measurement grid (described in section 4.4.2) with the probe positioned at the transverse position of Z=0 cm. The resulting data were stored as least significant bits (LSB's) and were used as input to a software package, PROCESS I. The algorithms, PROCESS I and PROCESS II, are discussed extensively in Foss, Klewicki and Disimile, 1984. The outputs of PROCESS I are the following time series: the velocities, Q<sub>3</sub> and Q<sub>4</sub> from the parallel array and the velocity Q<sub>x</sub> and the angle γ from the I-array.

The following sections will present the phase averaged transverse vorticity,  $\langle \omega_z \rangle$ . The spatial distribution and the temporal evolution of the phase averaged vorticity field will be evident in the contour plot representations of these phase averaged data. In addition, the quasi-instantaneous transverse vorticity,  $\omega_z(\tau)$  will also be presented.

## 6.2 Spatial Distribution of the Phase Averaged Transverse Vorticity

Figures 22 to 28 represent the phase averaged transverse vorticity,  $\langle \mathbf{w}_{\mathbf{z}} \rangle_{\mathbf{i}}$ , contours depicting the spatial distribution of the vortical motions in the mixing layer at a specific phase point (i). These spatial values of the phase averaged transverse vorticity,  $\langle \mathbf{w}_{\mathbf{z}} \rangle_{\mathbf{i}}$ , were obtained with the use of an algorithm called "VORTIS". The following items identify the signal processing steps used to obtain the  $\langle \mathbf{w}_{\mathbf{z}} \rangle_{\mathbf{i}}$  output:

- i) The digitized and phase averaged hot-wire voltages  $\langle E_1 \rangle$  and  $\langle E_2 \rangle$  from the X-array were used by Process I to calculate  $\langle Q_{\chi} \rangle_i$  and  $\langle \gamma \rangle_i$ .
- ii) The values  $\langle Q_x \rangle_i$  and  $\langle \gamma \rangle_i$  were input to the processing routine "VORTIS" where  $\langle U \rangle_i$  and  $\langle V \rangle_i$  were computed

$$\langle \mathbb{U} \rangle_{i} = \langle \mathbb{Q}_{x} \rangle_{i} \cos \langle \gamma \rangle_{i} \tag{6.1a}$$

and

$$\langle V \rangle_{\dot{i}} = \langle Q_{x} \rangle_{\dot{i}} \sin \langle \gamma \rangle_{\dot{i}}$$
 (6.1b)

for each phase point i at each of the (X,Y)-locations.

iii) To determine the value of the phase averaged transverse vorticity,  $\langle w_{\chi} \rangle_{\dot{1}}$ , at a specific phase point and (X,Y)-location, two spatial velocity gradients are required:

$$\partial \langle V \rangle / \partial X \Big]_i$$
 and  $\partial \langle U \rangle / \partial Y \Big]_i$ .

These spatial velocity gradients were also calculated with the use of VORTIS.

iv) Starting with the first phase point (i=1), all the  $\langle U \rangle_1$  components of velocity for the first X-plane (all 9 Y-measurement locations) were curve-fit with the use of a cubic spline subroutine (included in VORTIS). The present cubic spline subroutine allows the user to select various end conditions. These end conditions are;

- a] The first derivative is equal to zero.
- b] The second derivative is equal to zero.
- c] The jump in the third derivative across the adjacent

interior point is forced to zero.

The vorticity was calculated using all three end conditions and the respective values are compared in Appendix A. Except for the measurement points on the lateral boundaries, the vorticity values were found to be insensitive to the end conditions. The end condition corresponding to the second derivative equal to zero was selected for use in this study.

The cubic spline subroutine curve-fits a cubic equation of the following general form between the data points:

$$F_{i}(Y) = C_{i}(1,I) + C_{i}(2,I) + C_{i}(3,I) + C_{i}(4,I) + C_{i}$$

Y = location where  $F_i$  is to be evaluated,

Y(I) = actual Y measurement location.

i = phase point.

The result of this curve-fitting operation is 8 sets of coefficients (or 8 cubic equations) which are obtained for each of the X-planes.

v) Taking the derivative of equation (6.2), with respect to Y, yields an equation for the determination of F'(Y) at any Y-location:

$$F_{i}'(Y) = C_{i}(2,I)+C_{i}(3,I)+C_{i}(4,I)+B^{2}/2$$

The spatial velocity gradient  $\partial \langle U \rangle / \partial Y \Big]_i$  can be determined throughout the 46x9 measurement grid by repeating this calculation for all 46 X-planes.

vi) In a similar manner, all the phase averaged lateral velocity components,  $\langle V \rangle_i$ , for a specific Y-plane were computed and stored in memory. Then, for a given Y-plane a cubic spline was fit through each data pair at all 46 X-locations (the 46 locations correspond to the number of X-measurement points in a single Y-plane). The results are 45 sets of coefficients or 45 cubic equations. The general form is:

$$G_{i}(X) = D_{i}(1,I) + D_{i}(2,I) + D_{i}(3,I) + D_{i}(4,I) + D_{i}$$

X = location where  $G_i$  is to be evaluated,

X(I) = actual X-measurement location,

i = phase point (or time).

vii) Taking the derivative of equation (6.3) with respect to X yields an equation for the determination of G'(X) at any X-location. Performing this set of operations for all Y-planes (there are 9 Y-planes), the spatial velocity gradient  $\partial \langle V \rangle / \partial X$  can be calculated throughout the 46x9 measurement grid.

viii) Finally, the phase averaged transverse vorticity can be calculated at a specific phase point as:

$$\langle \omega_{\mathbf{x}} \rangle_{\mathbf{i}} = \partial \langle \mathbf{V} \rangle / \partial \mathbf{X} \Big]_{\mathbf{i}} - \partial \langle \mathbf{U} \rangle / \partial \mathbf{Y} \Big]_{\mathbf{i}}. \tag{6.4}$$

These results were stored in a file containing the (X,Y) coordinates and the magnitudes of  $\langle w_{Z} \rangle_{i}$  for the complete 414 point measurement grid. This file was then sent to the Cyber 750 mainframe computer where  $\langle w_{Z} \rangle_{i}$  contours were generated using the Surface II Graphics System.

A comparison of the contours obtained at the different phases (times) will give an indication of the temporal changes in the vorticity field. To allow for easy identification of the vorticity contour lines in the initial region of the excited mixing layer, an expanded view of this region is included in Figure 22. In Figures 22 to 28 the phase averaged transverse vorticity is plotted for a specific phase point of the excitation mechanism. These figures are labelled in such a fashion as to indicate the phase point which they represent. For example, Figure 23, containing the contours W1 and W63, represents the phase averaged transverse vorticity obtained at the 1st and 63rd phase point of the excitation mechanism, respectively. The following table presents a list of the figures and their respective phase points.

Table 6.1 Designation of the phase time (i) for  $\langle \omega_z \rangle_i$  contours: Wi

Figure 22: W1 (initial region)

Figure 23: V1 AND V63

Figure 24: W63 and W125

Figure 25: W125 and W187

Figure 26: W187 and W227

Figure 27: W227 and W289

Figure 28: W289 and W320

## 6.3 Phase Averaged Streamwise Velocity Profiles

The phase averaged streamwise velocity component was calculated for each phase point, at all (XY) locations and fit with a cubic spline using VORTIS. The resulting spline equations allow for the determination of the lateral distribution of non-dimensional velocity. This lateral distribution of the nondimensional streamwise component of velocity at the last phase point,  $\langle U(Y) \rangle_{sign}/U_0$  is plotted in Figure 29 for the following X-planes:

X = 24.4, 39.7, 54.9, 70.2, 85.4, 100.6, 115.9, 131.1 and 146.4 cm.

Also  $\langle U(Y) \rangle_i / U_0$  is plotted at X=85.4 cm (Figure 30) for the following phase points:

i = 1, 63, 125, 187, 227, 289, and 320.

## 6.4 Perturbed Phase Averaged Transverse Vorticity Contours

The contours of phase averaged vorticity exhibit many interesting features. However, it was recognized that some of the features may be artifacts of the contouring routine or they may result from finite sample size affects. It was considered appropriate to test the sensitivity of the contours to perturbations of the measured voltages.

The strategy used to investigate this sensitivity, was to select random voltage perturbations to be added to the phase average voltages

random voltage perturbations to be added to the phase average voltages  $(\langle E_1 \rangle, \langle E_3 \rangle)$  at a given (X,Y)-location. The technique used to generate the random perturbations is described below; it should be noted that the spatial locations, at which the perturbation was to be applied, was also randomly selected. This spatial randomness was to eliminate any bias in the spatial derivatives. The voltages at each of the 414 measurement locations were subjected to the following perturbation process.

The perturbed voltages  $\langle E_1^p \rangle$  and  $\langle E_2^p \rangle$  were obtained from the phase average voltages ( $\langle E_1 \rangle$  and  $\langle E_2 \rangle$ ) and the average standard deviations ( $\sigma_1$  and  $\sigma_2$ ) by the following operation:

$$\langle E_1^p \rangle = \langle E_1 \rangle + K \circ \sigma_1 \tag{6.5a}$$

$$\langle \mathbb{E}_{3}^{p} \rangle = \langle \mathbb{E}_{3} \rangle + \mathbb{K}^{\bullet} \sigma_{2} \tag{6.5b}$$

where the values of  $\sigma_1$  and  $\sigma_2$  are presented in Appendix B and K is the randomly selected multiplier with possible values of 0.±.0625, ±.125, ±.1875, ±.25. The K multiplier was selected by using the following procedure:

- i) a random number routine, with equal probability of selecting a value from a 0 to 1 line seement, was sampled.
- ii) if the sample was within 0.5±0.25, K was set to zero; if the sample was beyond the first range but within 0.5±0.41, K was set

to ±0.0625.

iii) a similar procedure was used for the other K values where the bounds are  $0.5\pm0.47$ ,  $0.5\pm0.49$  and  $0.5\pm0.5$ .

The routine, PERTAV. was used to create the perturbed data files that were subsequently input to PROCESS I and VORTIS. The output of VORTIS was then plotted as perturbed phase averaged transverse vorticity,  $\langle \mathbf{e}_{\mathbf{z}}^{\mathbf{p}} \rangle_{\mathbf{i}}$ , contours using Surface II graphics. The perturbed plots have also been labelled in a manner similar to the unperturbed contours. For example, in Figure 31 the contours WP1 and WP63 represent the perturbed phase averaged transverse vorticity acquired at the 1st and 63rd phase point of the excitation cycle. The following table presents a list of the figures and their respective phase points.

Table 6.2 Designation of the phase time (i) for  $\langle \omega_z^p \rangle_i$  contours: WPi

Figure 31: WP1 and WP63

Figure 32: WP63 and WP125

Figure 33: WP125 and WP187

Figure 34: WP187 and WP227

Figure 35: WP227 and WP289

Figure 36: WP289 and WP320

## 6.5 Temporal Evolution of the Phase Averaged Transverse Vorticity

Phase averaged transverse vorticity,  $\langle m_{\chi}(\chi, \Upsilon) \rangle$  time series were obtained at all 414 (X,Y) locations (see Figures 37 to 38). In order to obtain an accurate temporal history at any given (X,Y) location the

algorithm VORTIS was run for each discrete phase time; hence, 320 calculations were executed for the 10.24 ms sample time. (The discrete samples were separated by 0.032 ms.) In addition the output files from VORTIS had to be passed to the software package "VORTEN". This algorithm rearranges the phase averaged transverse vorticity files in such a manner as to prepare an  $\langle \omega_{\chi}(\chi, \chi) \rangle$  time series for each  $(\chi, \chi)$ —measurement location. The temporal resolution of these time series is 0.032 ms. The following table presents a list of figures at the respective  $(\chi, \chi)$  locations.

# Table 6.3 Phase Average Transverse Vorticity Time Series

Figure 37a and b: X=48.8 cm and Y=-7.3 cm to 7.9 cm

Figure 38a and b: X=84.4 cm and Y=-7.3 cm to 11.0 cm

## 6.6 Quasi-Instantaneous Transverse Vorticity

The quasi-instantanteous vorticity  $\omega_{\chi}(X,Y,\tau)$  is calculated using the instantaneous data obtained at each of the 414  $(X,Y,\tau)$  measurement locations and the algorithm PROCESS II (which is extensively discussed in Foss, Flewecki and Disimile, 1984). To obtain an  $\omega_{\chi}(X,Y,\tau)$  time series it is essential that the four wire array (the vorticity probe) be used. Specifically, the stored instantaneous voltage time series is passed through PROCESS I whose output is read by PROCESS II. The output of PROCESS II is an irregular time series of  $\omega_{\chi}(X,Y,\tau)$ . Because of the size of the data set (there were 12.500  $\omega_{\chi}(\tau)$  plots available) only a few representative plots are being presented. They

# are listed in table 6.4.

# Table 6.4 Quasi-Instantaneous Transverse Vorticity

Figures 39 and 40: Y=18.3 cm and Y=-4.3,-1.2 and 1.8 cm.

Figures 41 and 42: X=34.6 cm and Y=-4.3 and -1.2 cm.

Figures 43 and 44: X=42.7 cm and Y=-4.3 and -1.2 cm.

Figure 45: X=45.8 cm and Y=-7.3, -4.3 and -1.2 cm.

Figure 46: X=48.8 cm and Y=-4.3, -1.2 and 1.8 cm.

Figure 47: X=51.9 cm and Y=-4.3,-1.2 and Y=1.8 cm.

Figure 48: X=58.0 cm and Y=-4.3,-1.2 and 1.8 cm.

Figure 49: X=61.0 cm and Y=-4.3,-1.2 and 1.8 cm.

Figure 50: X=134.2 cm and Y=-4.3,-1.2 and 1.8 cm.

### CHAPTER 7

### DISCUSSION OF VORTICITY MEASUREMENTS IN AN EXCITED MIXING LAYER

### 7.1 Introduction

In the present section the detailed properties of the phase averaged vorticity field over 15% of the excitation cycle (and some aspects of the quasi-instantaneous vorticity time series from representive spatial locations) are examined. The phase averaged vorticity is created by the excitation of the separating boundary layer of a single stream mixing layer.

Fieldler and coworkers (1978, 1979, 1980, 1982) have extensively examined the general features of the excited mixing layer; the present results are in agreement with and extend their observations. A prominent feature of the phase averaged vorticity field is the existance of relatively large scale vortical motions at some distance downstream from the separation lip. It is important to emphasize that these well defined vortical structures would not be observed in the time (or ensemble) averaged data from an unexcited mixing layer. Such structures, or coherent motions, are known to exist in an unexcited mixing layer, but spatial and temporal irregularity of their occurence would

not allow them to be discerned in a time (or ensemble) average representation of the flow field. Figure 51, shows a smoke photograph taken from the Dr.-Ing. Thesis of P. Mensing (1981, photograph 3). The dimensionless phase averaged isotochs,  $U/U_0=0.1$  and 0.95, and the smoke photograph taken at the same phase time are superimposed showing that an instantaneous and the phase average representations of the flow are in good agreement. This is representative of the repeatability (in the flow behavior) that is created by the excitation process. From this figure (Mensing's) the prominant features of the excited mixing layer can be identified:

- i) The mixing layer width, as defined by the 0.1 and 0.95 isotach contours, exhibits a sudden increase at a streamwise distance that is slightly upstream of the first identifiable vortex.
- ii) As the vortex moves downstream it grows in size and its periodic (or phase average) energy reaches a maximum at a location  $X_s$  (St<sub>s</sub>=1). At this location the vortical motion is said to be saturated. That is, the vortex has reached the end of the region of amplification and will no longer be amplified.
- iii) Slightly upstream of the location of the saturated structure the mixing layer exhibits another rapid change in width.
- iv) A thin region of concentrated vorticity exists between the separation lip and the first formed vortical motion. In the present study this region is termed the "tongue".

Seven contour plots of phase averaged transverse vorticity,  $\langle \omega_z \rangle_1$  have been selected for discussion. Each plot represents the phase averaged transverse vorticity field at a phase time i and the seven plots cover 15% of the excitation cycle. The evolution of the phase averaged transverse vorticity can be determined by a comparison of two or more contour plots. In addition, plots of the streamwise component of velocity for several X-planes have been included for reference (see Figure 29). These considerations are dealt with in the following section.

# 7.2 Phase Averaged Streamwise Velocity

The non-dimensional phase averaged streamwise velocity component,  $\langle U(Y)\rangle_i/U_0$  is presented in Figure 29. An examination of these curves indicates the varying slope at the lateral end points of the measurement grid as the profile is plotted at subsequent downstream X-planes. The flattening or spreading out of the velocity profiles is apparent downstream of the separation lip. Figure 30 depicts the  $\langle U(Y)\rangle_i/U_0$  profiles obtained at an X-plane approximately aligned with the center of the saturated structure for successive phase times. This plot indicates that the streamwise non-dimensional velocity profile at this specific X-plane is relatively independent of the phase time.

# 7.3 Evolution of the Phase Averaged Transverse Vorticity

# 7.3.1 Spatial Distribution of the Phase Averaged Transverse Vorticity

The phase averaged transverse vorticity,  $\langle \omega_z \rangle_i$  contours, are presented in Figures 22 to 28. These contours show the general features of an excited mixing layer. The insensitivity of some features of these  $\langle \omega_z \rangle_i$  contours to random perturbations in the flow is discussed in section 7.4. This insensitivity allows detailed examination of these features with the confidence that the perceived features are not an artifact of the contouring routine. A comparison of Mensing's photograph 3 (Figure 51) to the phase averaged transverse vorticity:  $\langle \omega_z \rangle_i$ , contours obtained in the present work indicate good agreement between the general features of the two flow fields.

A relatively thin region of vortical fluid, which extends from the separation lip downstream to the newly formed vortical structure, is also visible. This relatively thin, highly vortical, region is characterized by: i) the closed vortical contour lines ( $\langle \omega_z \rangle_i = 140,150$ ...) and ii) a slight linear growth of the contour lines upstream of the closure region. As in section 7.1 item iv) above, this region is termed the tongue.

There are two options for selecting a distance used in the nondimensional represention of the downstream distance (X); they are: i) use of the momentum thickness of the separation boundary layer, as has

been standard in the unexcited mixing layer, or ii) use of  $\mathbb{U}/f_e$  resulting in a Strouhal number based on X. The latter has been selected to allow direct quantitative comparison to the studies of Fiedler and coworkers.

In the present discussion Figure 28b will be used to compare the present work to that of Fiedler and coworkers. An examination of Figure 28b (W320) indicates that the boundary layer "tongue" extends downstream to approximately X=42 cm or  $St_x\approx0.48$ . A rapid change in the width of the lower level vorticity lines on the low velocity side of the mixing layer is observed (see X=28 to 33 cm) in Figure 28b. After this rapid growth, the width of the mixing layer is approximately constant. This region of approximately zero growth continues downstream to the nominal upstream boundary (X=43 cm,  $St_x=0.496$ ) of the first fully formed vortex motion. The location of this first vortex is termed the region of "roll-up" by Fiedler and coworkers and it is preceded by another short segment of rapid growth in the width of the vorticity contours. The center of this first vortex is at X=48 cm or  $St_x=0.55$ . This value is in quite good agreement with the corresponding location ( $St_x=0.5$ ) from the Mensing study.

A region of nominally zero growth exists downstream of the first newly formed vortex. This "constant" width region is terminated by another region of rapid growth just upstream of the saturated vortical structure. The position of this second vortex (X<sub>g</sub>=85 cm) is in striking agreement with the equivalent vortex motion (the saturated vortex)

that was observed by Fiedler and coworkers [1980, 1982]; see item ii of Section 7.1. For a weakly excited flow, they found that the nondimensional downstream distance where the saturated structure is located is related to  $St_x$ . Interpolating  $St_x$  from Mensing's work (1981) for a similar excitation intensity the following was obtained:

$$St_s = f_e + I_s / U_o = 0.97$$

(where St 20.97 is based on an approximate excitation intensity of 0.0052 as compared to 0.00537 in the present investigation). For the present investigation a St. = 0.98 was determined. Farther downstream the periodic energy of the saturated structure starts to decay, with little or no increase in the width of the shear layer. The distance beginning at the location of the saturated structure and extending downstream to a location where the St, ~1.5 is termed the decay region (Chapter 1) by Fiedler, et.al. For the present work, the decay starts at approximately X=85 cm and extends downstream to X=140 cm (to the center of the decayed structure). This is equivalent to St, ~1.6, which differs by 6.6 % from the value found by Fiedler and coworkers [1980,1981,1982]. At this position, X=140 cm (the end of the decay region), another rapid change in the shear layer width is observed; beyond this position, it is inferred (from the observations by Fiedler, et.al.) that the shear layer will slowly assume the character of a natural shear layer. Hence, any noticable effect of excitation is found to persist only up to a streamwise position of approximately 140 cm.

## 7.3.2 General Temporal Evolution of the Coherent Vorticity Contours

The temporal evolution of the coherent vorticity,  $\langle \omega_z \rangle_i$  can be qualitatively obtained by a comparison of Figure 22 and 28 (each contour plot represents a specific phase time, i). The detailed observations obtained from such comparisons are listed in Appendix C. The following observations are based upon a net evaluation of these separate observations.

From the phase averaged transverse vorticity contours it has been observed that the lower level vorticity contour lines, from the high speed side, make deeper depressions into the mixing layer (at X=42 and 73.2 cm) than their counterparts on the low speed side. Accompanying this depression of the vorticity lines is an increase in the phase averaged lateral velocity  $\langle V \rangle$  on the upstream side of the depression by approximately 25 % (cf. the  $\langle V \rangle$  value of the fluid in the region where the  $\langle w_z \rangle$  contours are "parallel" to the X axis). In a complimentary way the growth and shrinkage of the concentrated vortical structure (vorticity values from 80 to 160) appear to be more dominant on the low speed side.

The average structure velocity ( $\mathbf{U}_{\mathbf{s}}$  was obtained for the newly formed vortex, the saturated vortex and the decayed vortex using the ratio  $\Delta L/\Delta t$ . The displacement:  $\Delta L$  is the downstream distance a specific vortical structure moved in the sample time interval:  $\Delta t$ . The average structure velocities were determined to be:

 $U_{\rm g} = 0.70$  m/s for the newly formed structure

 $\overline{U}_{s} = 5.51$  m/s for the saturated structure

 $\overline{\mathbf{U}}_{\mathbf{z}} = 1.76 \text{ m/s}$  for the decaying structure

As suggested by the velocity values, the translation of the three structures are quite different over the observation time of 15 percent of the complete cycle. The newly formed vortex moved 0.72 cm, the saturated vortex moved 5.64 cm and the decayed structure moved 1.7cm. If the 320th phase point is used to establish a characteristic "wavelength", it is noted for reference that the distance between the newly formed and the saturated vortex is 36.5 cm.

The velocity of the saturated structure, quoted above, is an average value; a more detailed examination of the time dependent position of the structures center is presented in Figure 52. The slope of this curve indicates the core velocity of the saturated structure. These velocities vary an order of magnitude and appear to indicate that the core has undergone periods of large acceleration and deceleration. The positions obtained by this method are estimates, in as much as they depend upon the somewhat arbitrary selection of "the vortex center". The dashed curve in Figure 52 is based upon the center of the saturated structure using the perturbed contours. This curve shows greater scatter but the trend is similar to that for the measured data. The perturbed results suggest that the non-uniform

translation of the vortex core may be an strongly influenced by the data processing procedures. In a similar manner, it can be determined that the front and the back of the large, saturated, vortical structure move at different speeds. Specifically, the front velocity,  $U_f$  =6.43 m/s and the back velocity,  $U_b$  =3.86 m/s. Evidence of this is also found in a flow visualization study preformed in an axisymmetric mixing layer by Hussain and Clark (1981).

The lateral location of the boundary layer tongue and of the centers of concentrated vortical fluid appear to be distributed symmetrically around the YZ-measurement plane where Y=-1.2 cm. If a measurement plane were aligned with the separation lip (at Y=0) it is possible that symmetry would exist around that plane. This is a result of the large spatial velocity gradient,

that exists at the separation lip and its influence on all points downstream.

There are two dominant vortex interactions which have been observed in the present experiment. They are the "tearing and fusing" of vortical fluid masses. The tearing process appears to be related to the deep incursions of the lower level vortical fluid from the high speed side of the mixing layer. The extent to which the vorticity contour lines are torn and the size of vortical fluid mass which is

separated is related to the distance downstream from the separation lip. That is, the farther downstream the structure is located when this tearing process takes place, the greater is the number of vorticity contour lines that are torn and the larger is this separate fluid mass. The fusion process is one in which two or more vortical fluid masses are brought close to each other, fuse and become one vortical mass.

# 7.4 Global Evaluation of the Perturbed and Unperturbed $\langle \omega_z \rangle_i$ Contours

The purpose of this section is to summarize the inferences that are based on the data perturbations. Recall from section 6.4 that the perturbed phase averaged transverse vorticity,  $\langle \omega_z^p \rangle_i$  contours were derived in the same manner as  $\langle w_z \rangle_i$  with the exception of the random addition or subtraction of a random voltage perturbation to the data before the processing stage. This random constant  $K^{\bullet}\overline{\sigma}$ , took on the discrete values from 0 to  $\pm$  .25 $\overline{\sigma}$  in increments of 0.0625 $\overline{\sigma}$ , where  $\overline{\sigma}$  is the time averaged standard deviation (discussed in section 6.4) of the unprocesed data. The spread of the mixing layer in both the perturbed and unperturbed cases are approximately the same. In addition, the locations of the concentrated vortical structures are also similar and the vortex interactions observed in the unperturbed case can still be observed in the perturbed contours. In general the only differences in the two cases are the magnitudes of vorticity; that is the level of vorticity in structures in the perturbed case appear to be greater than the unperturbed case by approximately 10 %. The deep depression of lower level vorticity lines in the region between the tongue and the newly formed vortex is also present. Therefore, it is concluded that in general, the major features, observed in the unperturbed case, are "robust" results and are not altered by perturbations to the original data. It should be noted that, in general, larger perturbation levels led to more "closures" of the vorticity contours. See the large X values of Figures 28 and 36 as examples of the "closure" effect.

## 7.5 Phase Averaged Transverse Vorticity Time Series

An investigation into the phase averaged transverse vorticity,  $\langle \omega_{\rm z} \rangle$ , time series in Figures 39a and 39b to 40a and 40b, provides quantitative information in support of the events observed in the  $\langle \omega_{\rm z} \rangle_{\rm i}$  contours. Note that these time series extend over 15.4 percent of the full cycle.

An examination of Figures 39a and 39b (X=48.8 cm and Y=-7.3, -4.3, -1.2, 1.8, 4.9, 7.9 and 11.0 cm) shows the level of phase averaged transverse vorticity variation to be of the same order at the center of the newly formed vortex (Y=-1.2 cm) and on the vortex periphery located at Y=1.8 cm; the variation is considerably reduced at Y=-4.3 cm. A similar comparison has been made for the saturated structure (Figures 40a and 40b). The center of this structure is located at X=85.4 cm (and Y=-7.3, -4.3, -1.2, 1.8, 4.9, 7.9 and 11.0 cm). The results indicate approximately the same magnitude of phase

averaged transverse vorticity variation at the structure center (Y=-1.2 cm) and its peripheries located at Y=-4.3 and 1.8 cm. Therefore it can be concluded from the phase averaged transverse vorticity time series that the center of the saturated structure is relatively calm on the average and that the  $\langle w_z \rangle$  variations in the concentrated vortical core is of similar magnitude as the  $\langle w_z \rangle$  variations on the vortex peripheries.

## 7.6 Quasi-Instantaneous Transverse Vorticity

### 7.6.1 Introduction

Thirty sets of high-rate (32 µs) data samples were collected at each point in the measurement grid. The majority of these sets are 2.5 ms in duration; two X-planes, as noted below provide 10 ms duration records. The transverse vorticity is computed for small (\(\lambda\) 1 mm x 1 mm) micro-circulation domains from these data. The resulting output is an irregular function of time as a result of the convected displacement which defines the length of the domain. Therefore, the output is termed a quasi-instantaneous time series of the transverse vorticity. Prior investigations of excited shear layers have not employed direct measurement of vorticity; hence, the results of this section are unique observations.

The plots of quasi-instantaneous transverse vorticity  $(\omega_z)$  shown are representative of the thirty sets of time series at any given (X,Y)-measurement location, unless otherwise specified. Specifically,

the representative plots were derived using the following procedure:
i) the mean and standard deviations were evaluated for each of the
thirty time series. ii) a single time series, which had a standard
deviation and a mean value that were similar to the average of the
group of thirty, was selected as the representative case.

It is recognized that this process provides only a qualitative basis for the comparisons of the phase averaged and the instantaneous vorticity values. However, these comparisons are quite instructive and they are included herein for this purpose.

## 7.6.2 Quasi-Instantaneous Transverse Vorticity Time Series

Figure 39 is a representative plot of  $\omega_{\chi}(\tau)$  for three lateral locations in the tongue region at X=18.4 cm. Their respective phase averaged values for the first phase point are included on the figure for reference. Large excursions of the vorticity at the center of the tongue are evident in this figure. The representative excursions near the high speed edge of the tongue, Y=-4.3 cm are relatively small ( $\simeq$ 100 s<sup>-1</sup>) whereas the low speed edge of the tongue exhibits intermediate level excursions. The limited data for the low speed side is indicative of the number of time steps which are required to form a complete circulation micro-domain.

Figure 40 shows two additional time series at X=18.4 cm; these where selected to represent the extreme cases for minimum excursions

at the centerline and relatively large excursions at the high speed edge. It is interesting to note that the excursion levels, for the two Y locations, are approximately the same.

Figures 41 and 42 are for X=33.6 cm. The former presents the representative conditions at X=33.6 cm and the latter Figure 42 shows two traces for which the excursion levels, at the high speed edge of the tongue and near the tongue centerline, are quite similar. The excursions are, again, seen to be quite large with respect to the phase averaged values.

In the region between the tongue's end and the newly formed vortex (X=39.7 to 45.8 cm) the net convective transport of lower level vortical fluid from the high speed side can be observed in the phase averaged transverse vorticity contours. An examination of the w, time series (Figures 43 and 44) which where obtained at X=42.7 cm, show high levels of vorticity fluctuations at the lateral locations: the high speed edge of the tongue (Y=-4.3 cm) and in the central region of the strongly vortical region (-1.2 cm). Unlike the tongue region, in which the excursions at the edge regions were small with respect to those near the centerline, the intermediate X-planes exhibit excursions which are large at both centerline and at Y-locations:-4.3 cm. It is considered to be significant that the quasi-instantaneous vorticity values show a distinctively different behavior in a region of the flow field where the phase averaged contours contours also exhibit a distinctive change.

Relatively large vorticity fluctuations can be observed in the newly formed vortex (at I=48.8 cm, Y=-4.3 cm, see Figure 45). In addition, the w<sub>Z</sub> fluctuation activity in the center of this new vortex (at Y=-1.2 cm) is approximately the same order of magnitude as the adjacent lateral positions on the periphery of the vortical structure. At the next downstream measurement plane (X=51.9 cm, Figure 46) the peak level of the w<sub>Z</sub> excursions, at Y=-1.2 and 1.8 cm, are also of the same order of magnitude. An examination of the complete set of the instantaneous records reveals that the frequency of the w<sub>Z</sub> fluctuations at Y=1.8 cm is systematically less than that at the central core and the high speed edge of the active region.

Figures 47 to 49 present a series of representative  $\mathbf{w}_{\mathbf{z}}(\tau)$  distributions at the streamwise locations: 58.0, 61.0,79.3 and 134.1 cm respectively. Althrough detailed differences exist, each of these stations can be characterized by similar magnitudes of peak excursions at the three lateral locations and by the relatively lower frequency of fluctuations at the Y=-1.8 cm locations. The  $\mathbf{w}_{\mathbf{z}}$  excursions in Figure 45 through 48 are quite large with respect to their respective phase averaged values.

In general the average level of the transverse vorticity fluctuations in the decaying region (X=134.1 cm, Figure 50) are smaller than at the upstream locations. Occasional  $\omega_{\rm Z}$  spikes of approximately 40 times the phase average transverse vorticity have been found in a number of the time series at this X-location.

## 7.6.3 Quasi-Instantaneous Transverse Vorticity Summary

The peak quasi-instantaneous transverse vorticity fluctuations in the tongue region reach a maximum in the core. These values of quasi-instantaneous transverse vorticity,  $\omega_z$  are approximately 20 times larger than the phase averaged transverse vorticity,  $\langle \omega_z \rangle_i$ . This confirms the concern regarding the possibility of ensemble averaging amearing out the peak values of vorticity (Dimotakis, Debussy and Koochesfahani,1981). In addition there were realizations in which  $\omega_z$  in the core region were of the same order of magnitude as  $\omega_z$  values at the laterally adjacent measurement points outside the concentrated tongue.

The quasi-instantaneous vorticity time series, although limited in scope, can be used to infer some basic features of the vortical regions. It is considered to be instructive that the fluctuation levels, across the newly formed and the saturated vortex motions are relatively large. This indicates that the entire vortex is a region of strong "activity". In contrast, Wygnanski, Oster and Fiedler (1979), have shown that the thermal field, in the core region of a large forced vortex motion, is relatively "inactive" whereas the boundaries of the vortex exhibit large temperature gradients and temperature fluctuations. The difference between these two measures of the excited mixing layer can be attributed to the different response in the vortical and in the thermal properties of a flow with intense, small scale, vortex motions. Specifically, it is inferred

from the vorticity measurements that the relatively high frequency and strongly fluctuating vorticity values are representative of such a flow. For a given amount of thermal energy (supplied in the upstream boundary layer) a flow field with energetic small scale motions would lead to enhanced heat transfer between adjacent fluid elements; hence, the imbedded temperature variations would be smoothed out by the enhanced diffusive effects.

In addition it has been found that the frequency of occurrence of these vorticity fluctuations varies throughout the newly forming structure. That is, the vorticity fluctuations on the low speed side (Y=1.8 cm) of the mixing layer are characterized by smaller frequency fluctuations in comparison with the fluctuation frequencies of the Y=-1.2 and -4.3 cm locations. Conversely the frequency of occurrence (of these w<sub>2</sub> fluctuations) appear approximately the same throughout the saturated structure.

In general, lower levels of  $\mathbf{w}_{\mathbf{z}}$  are found in the decay region. With the exception of an ocassional  $\mathbf{w}_{\mathbf{z}}$  spike, this decaying process appears to be quite violent at times generating fluctuations of  $\mathbf{w}_{\mathbf{z}}$  approximately 40 times the phase averaged transverse vorticity.

### CHAPTER 8

#### CONCLUSIONS

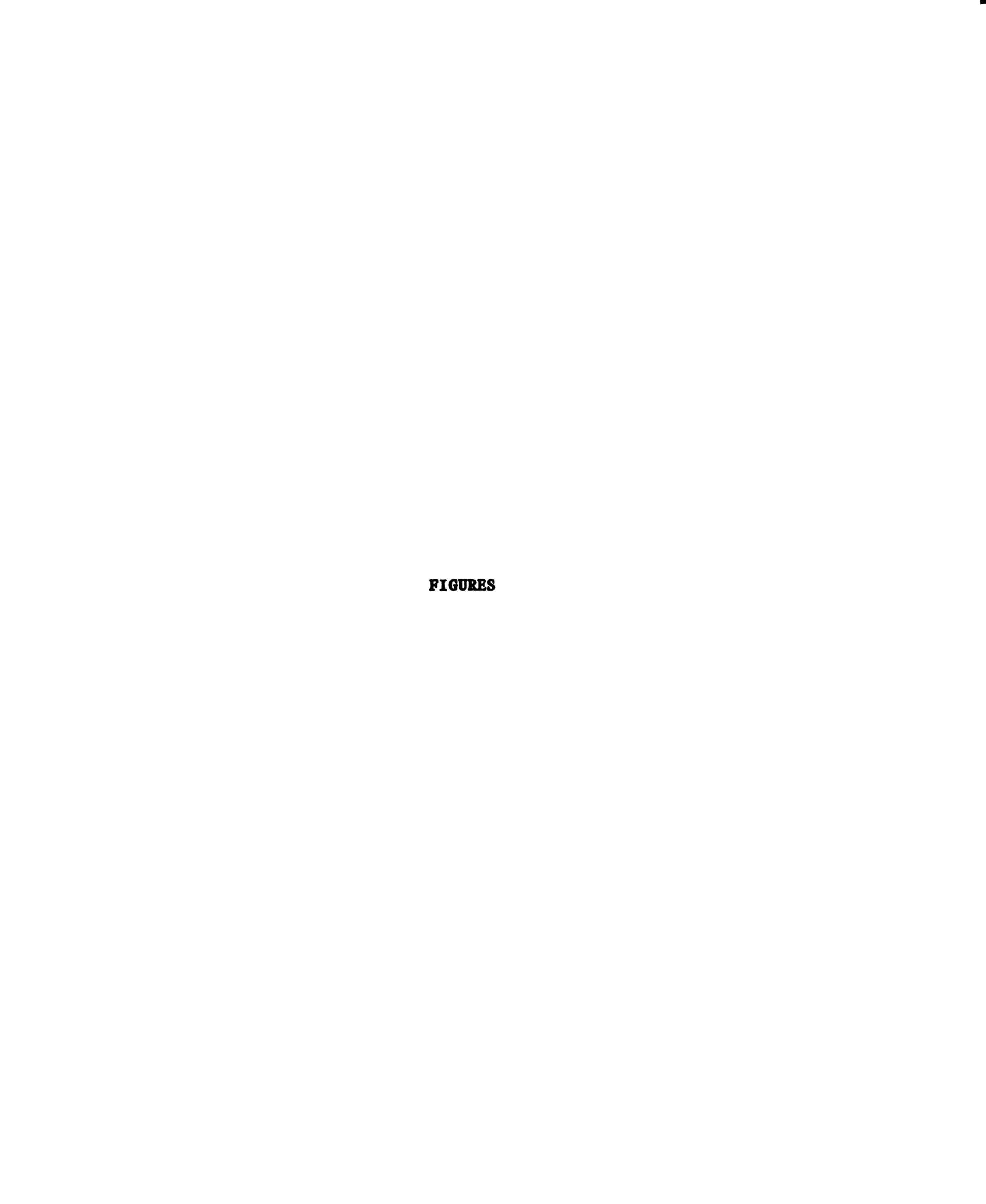
From the examination of the weakly excited and unexcited turbulent boundary layers, the following has been determined. The mean
velocity profiles obtained from the turbulent boundary layer surveys
show good agreement with Coles law in the logorithmic region. This
agreement in the mean velocity profiles will enable computational
fluid dynamists to apply modeling techniques to the excited mixing
layer using Coles law as a valid initial approximation to the velocity
profile in the turbulent boundary layer. In addition, a slight reduction in the momentum thickness was obtained in the present work when
the boundary layer was excited.

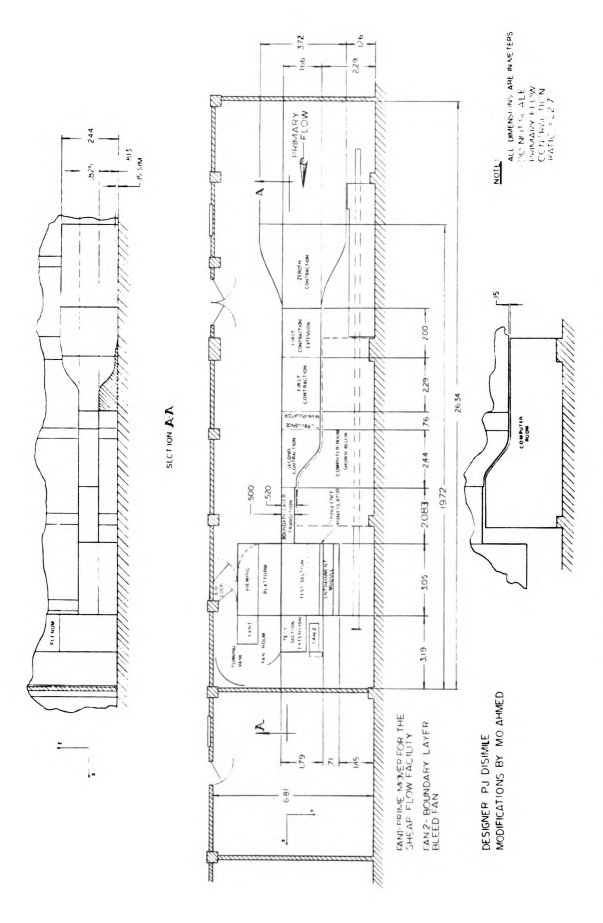
The prominent features of the phase averaged field: the tongue, the newly formed vortex, the saturated vortex and the decaying vortex, that were observed by Fiedler and coworkers are also observed in the present study. Using the 320th phase point as a representative condition, these last three structures appear at the nominal Strouhal number locations of:  $St_x=f_e*x/U_o=0.55$ , 0.98 and 1.6 respectively. These values are in good agreement with the corresponding values reported by Fiedler and coworkers.

The phase averaged vorticity contours indicate the deep depres-

In addition, the dominant growth and shrinkage of the vortical fluid masses seem to be more predominant on the low speed side of the mixing layer. It has also been observed (over the available 15% of the excitation cycle) that the cores of the vortical structures move at different speeds. Specifically, the saturated structure appears to move with a much larger average velocity, including periods of relatively large acceleration and deceleration. The existance of vortex interactions, such as tearing and fusing of vortical contours has also been observed.

The measurement of quasi-instantaneous transverse vorticity in the tongue and farther downstream in the vortical structures, have shown peak values of transverse vorticity excursions which are an order of magnitude larger than those of the phase averaged transverse vorticity. This sheds considerable light on the vortical activity within the concentrated vortex. In addition, these large instantaneous transverse vorticity fluctuations appear to have the same order of magnitude both in the concentrated region and the periphery of the Although the peak vortical structures. values of the quasi-instantaneous transverse vorticity, throughout the vortical structure, are of the same order of magnitude, their frequency of occurrence is not. Specifically, the occurrence of these large excursions is less frequent on the low velocity side of the mixing layer in the newly formed vortex.





jure 1 Free Shear Flow Facility Floor Plan

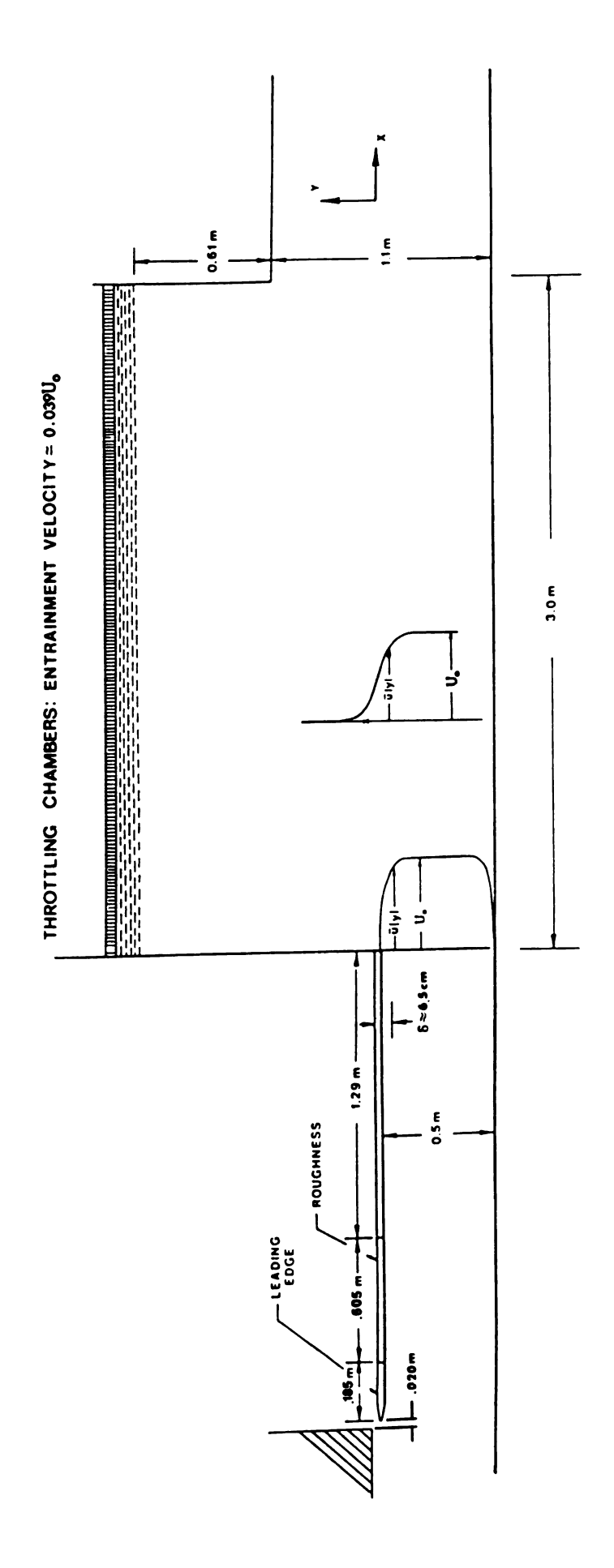


Figure 2 Boundary Layer Transition Module and Test Section

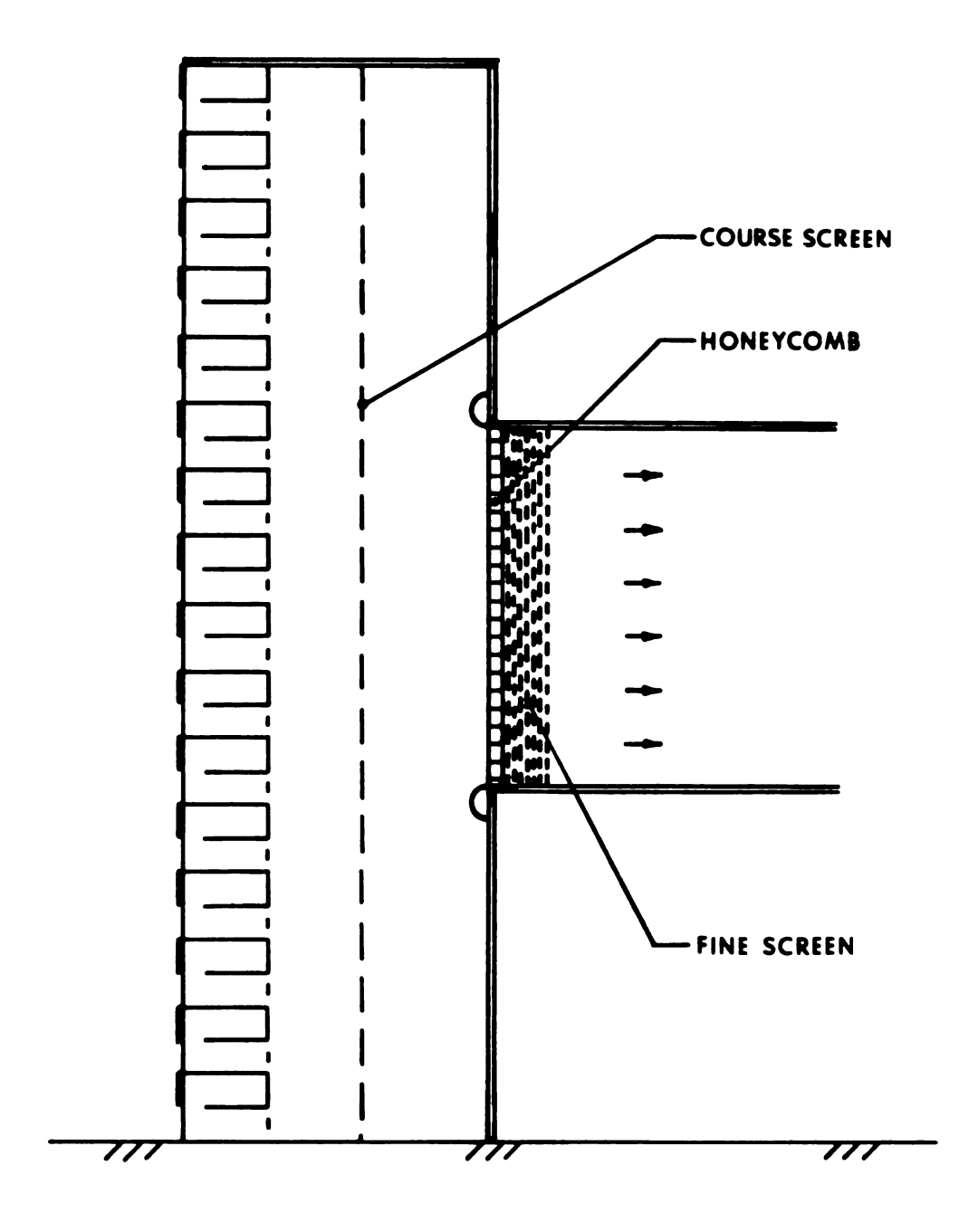
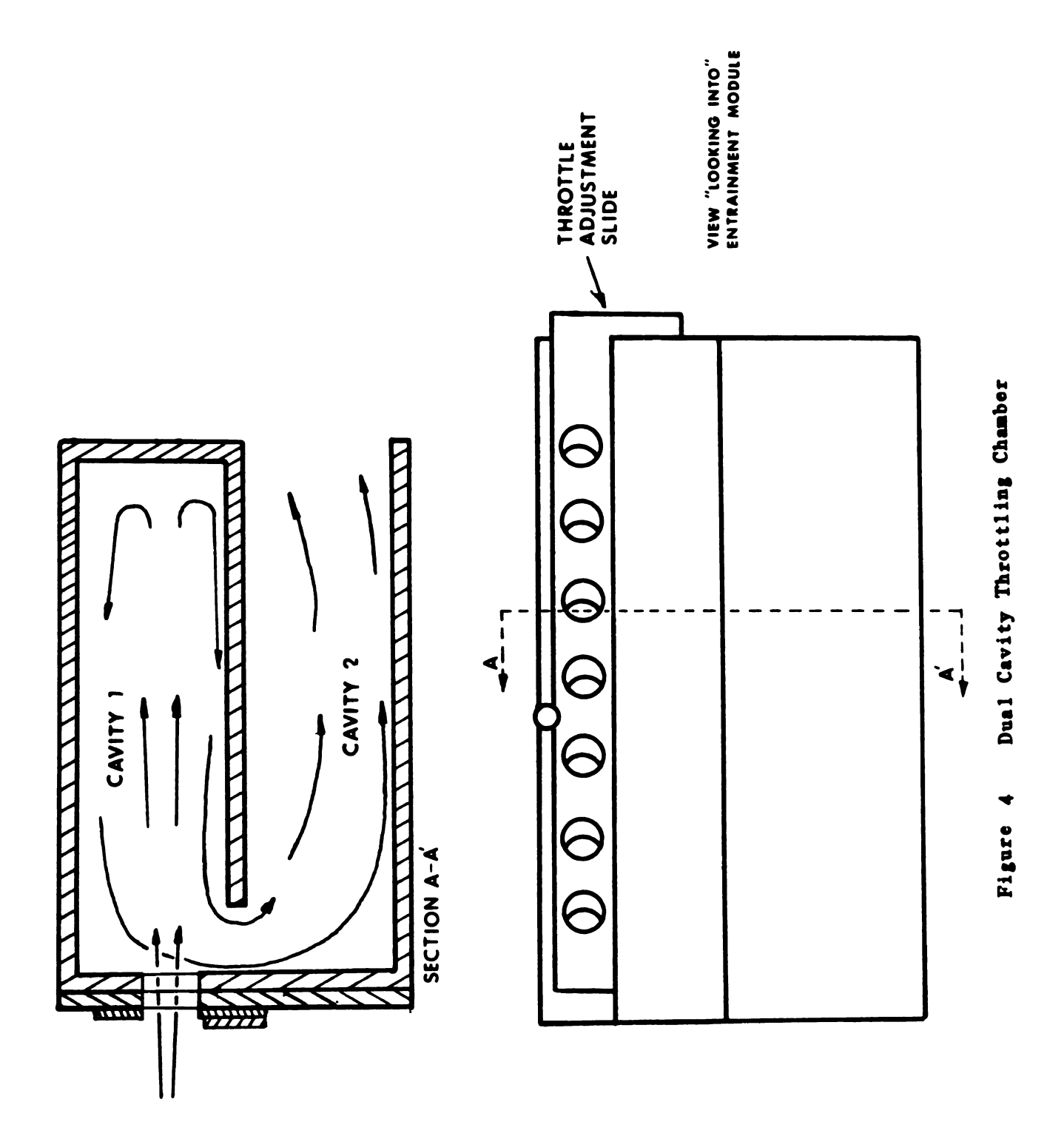


Figure 3 Entrainment Module



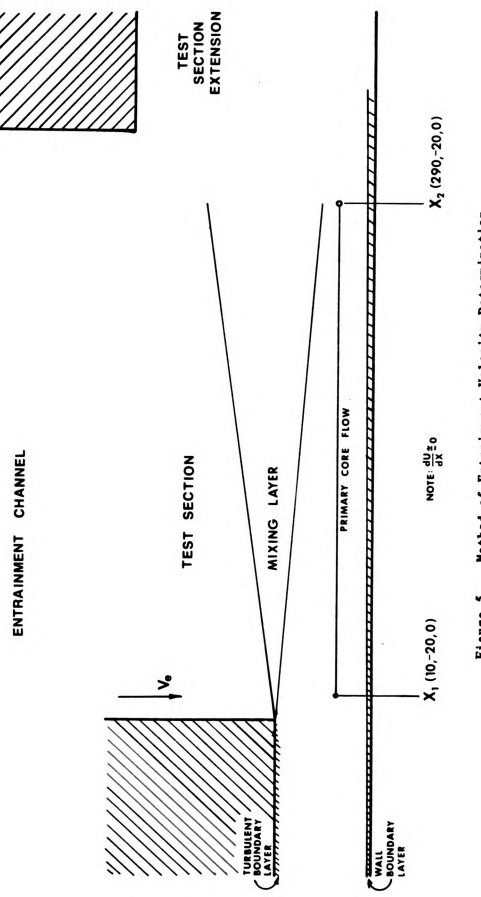


Figure 5 Method of Entrainment Velocity Determination

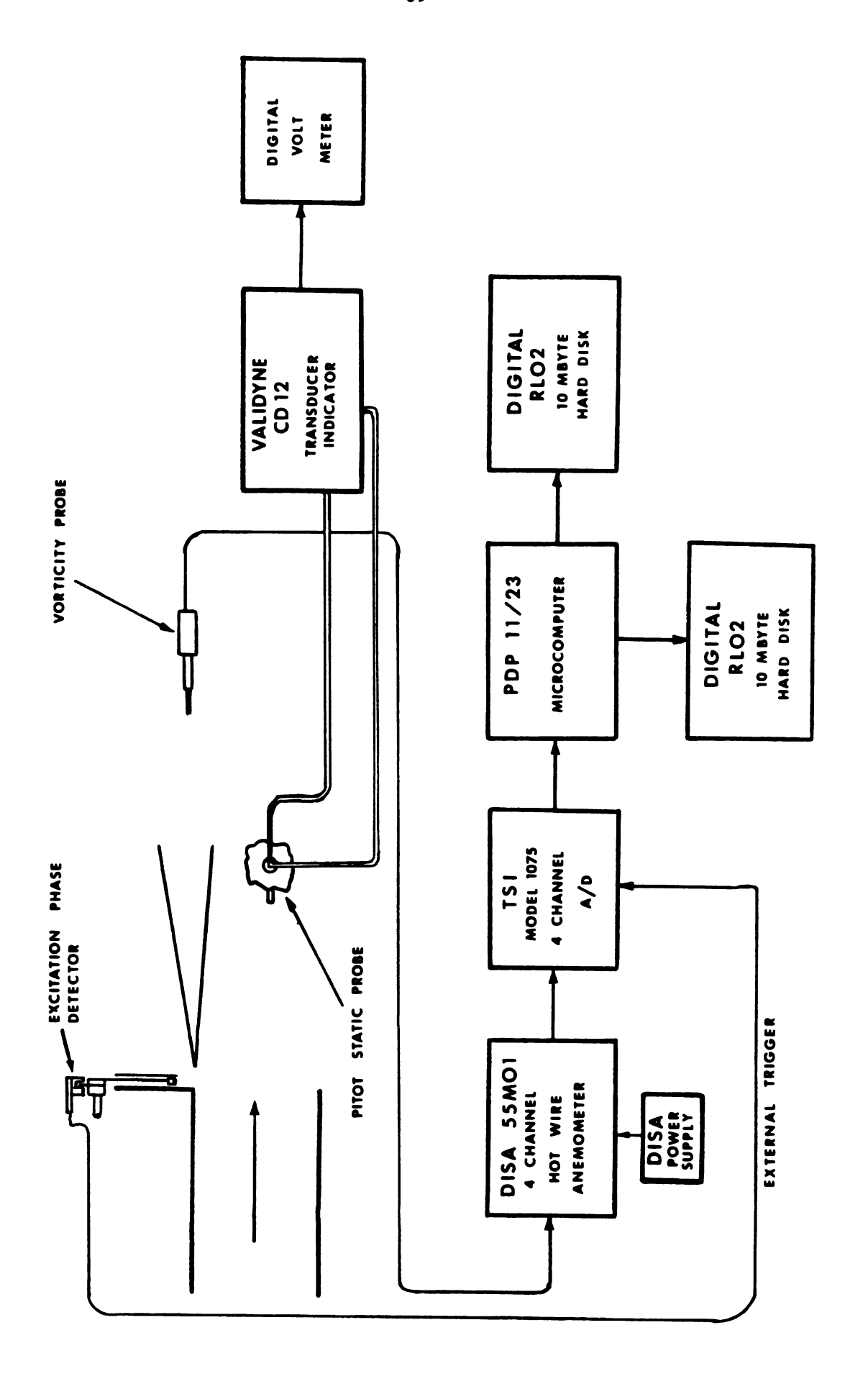


Figure 6 Data Aquisition Facility

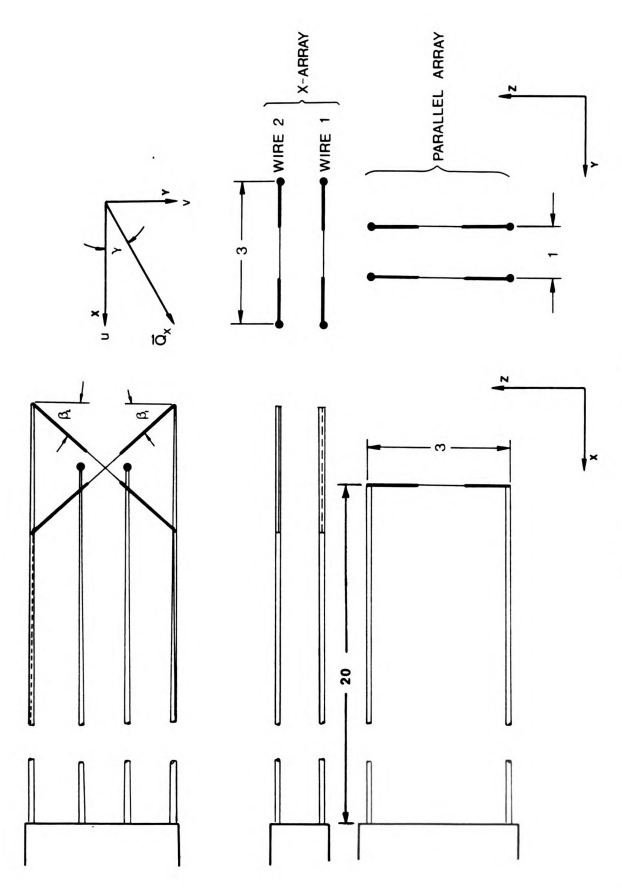


Figure 7a The Vorticity Probe

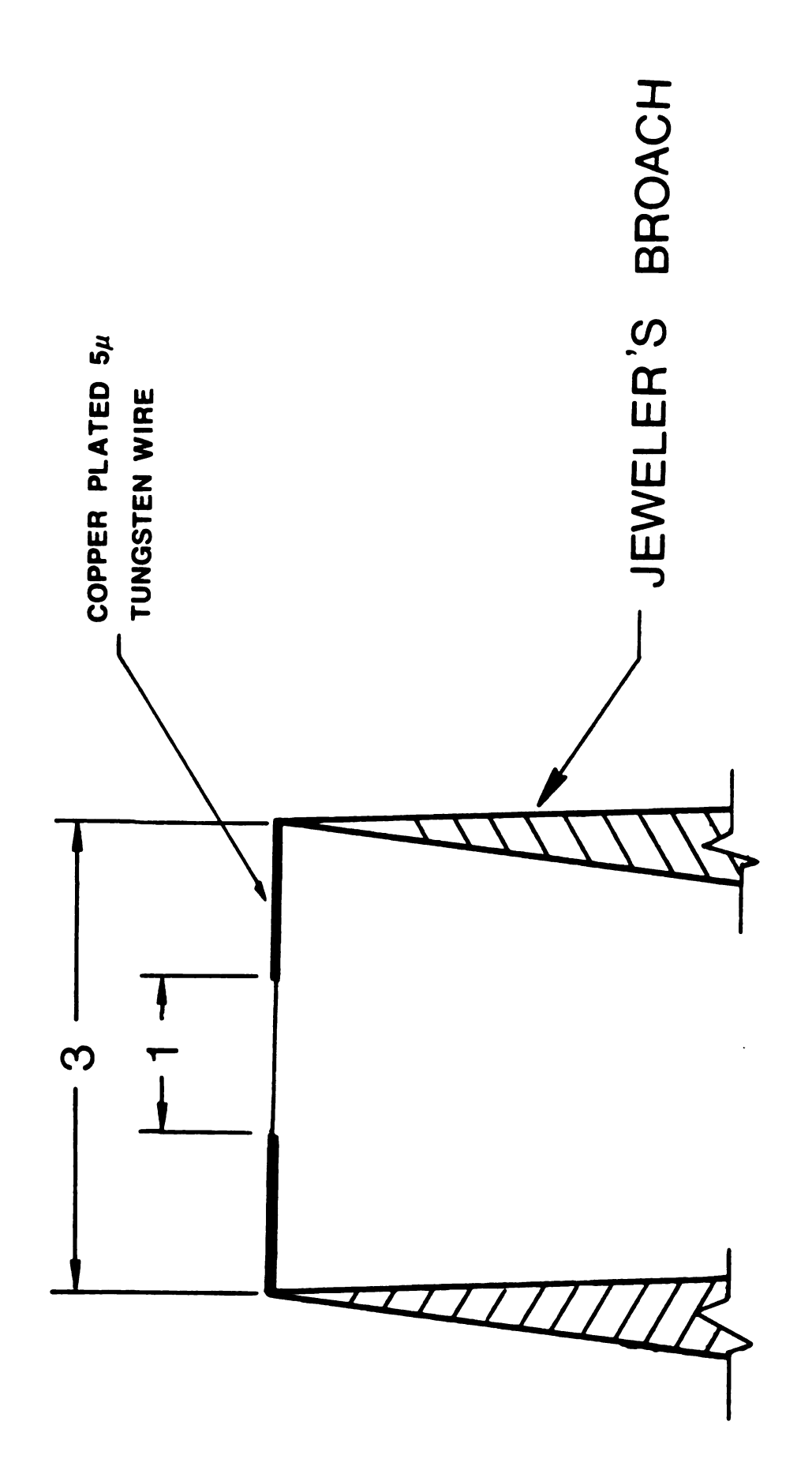


Figure 7b A Typical Hot-Wire Probe

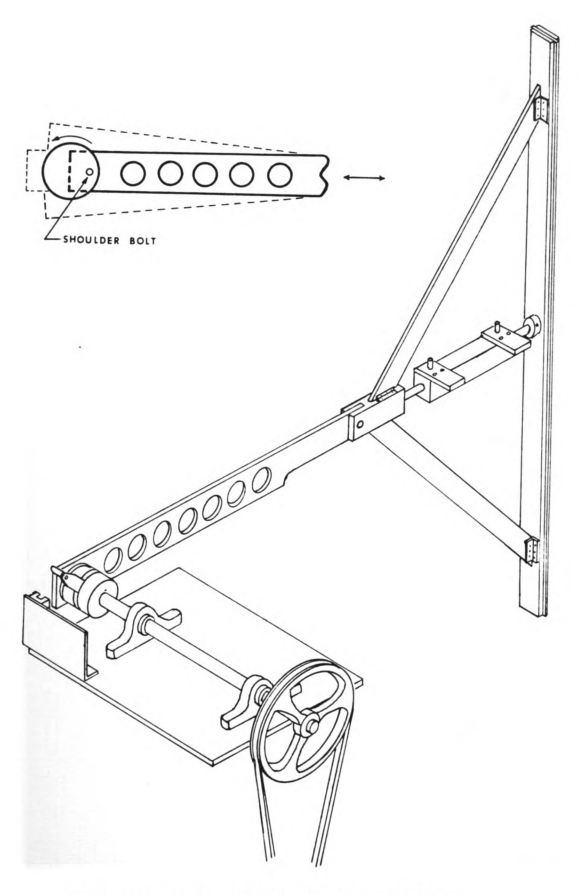


Figure 8a Excitation Mechanism (Isometric View)

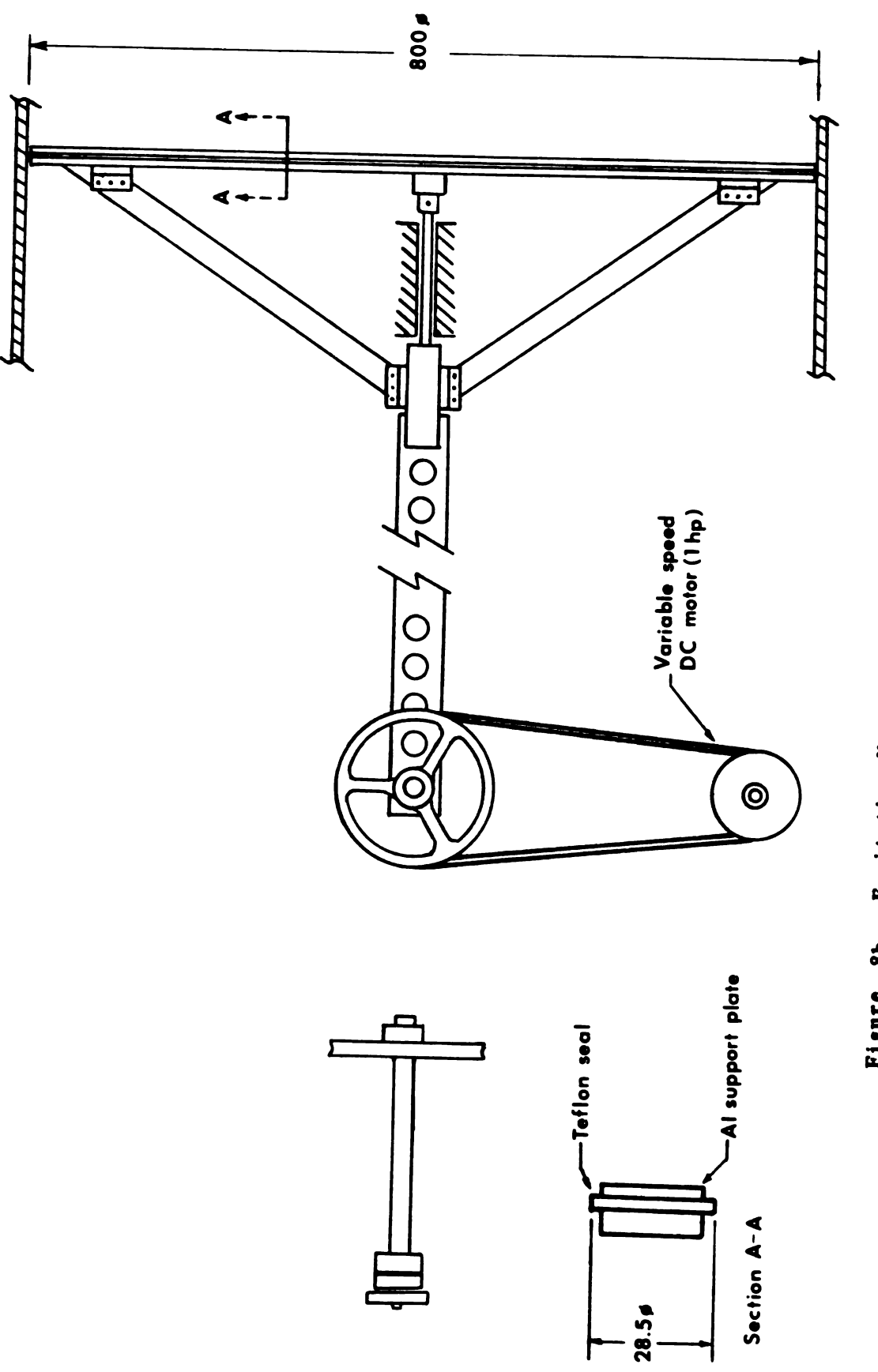


Figure 8b Excitation Mechanism (Side View)

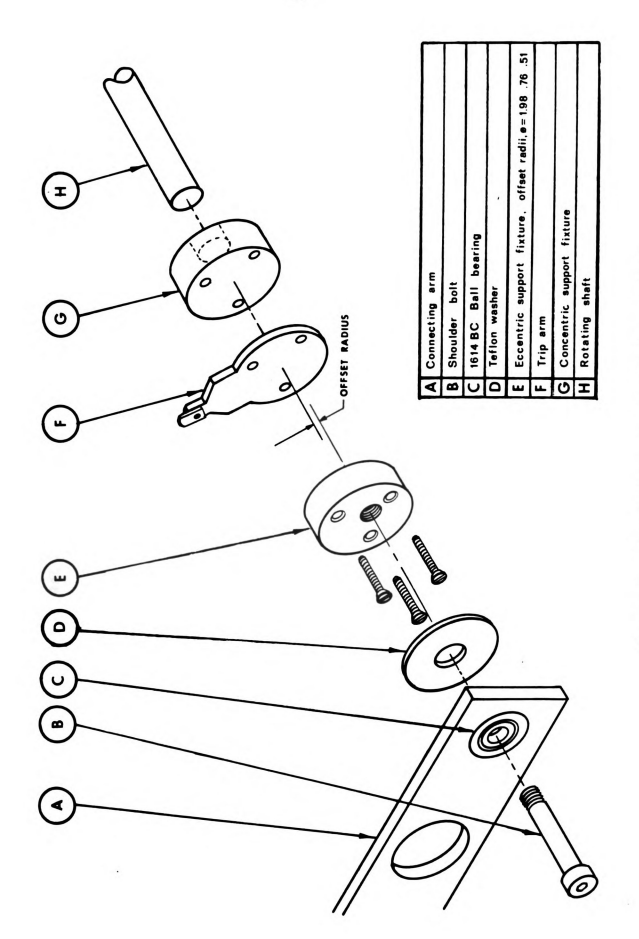


Figure 8c Excitation Mechanism (Support Fixture)

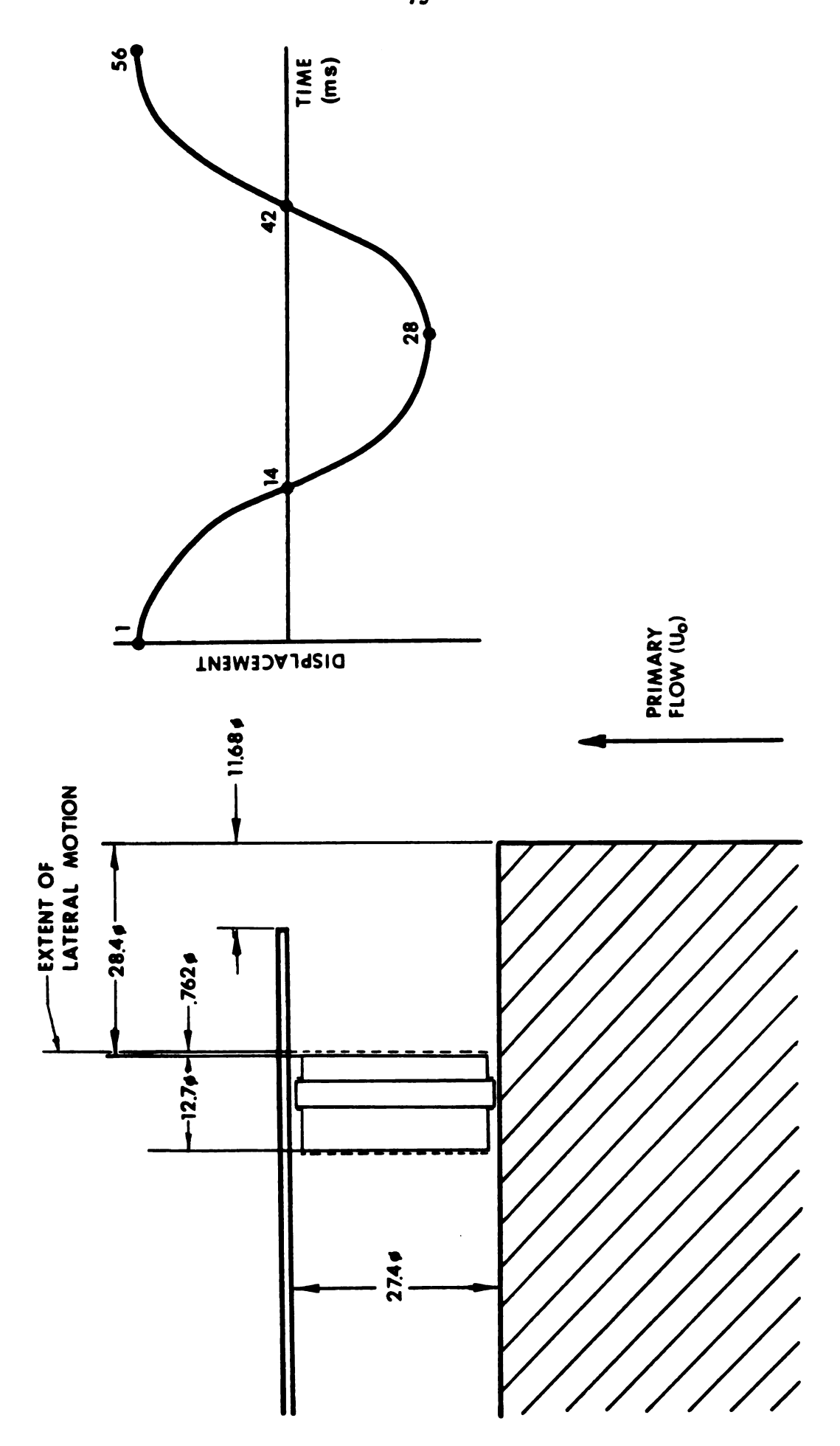


Figure 9a Schematic Representation of Excitation Intensity Determination

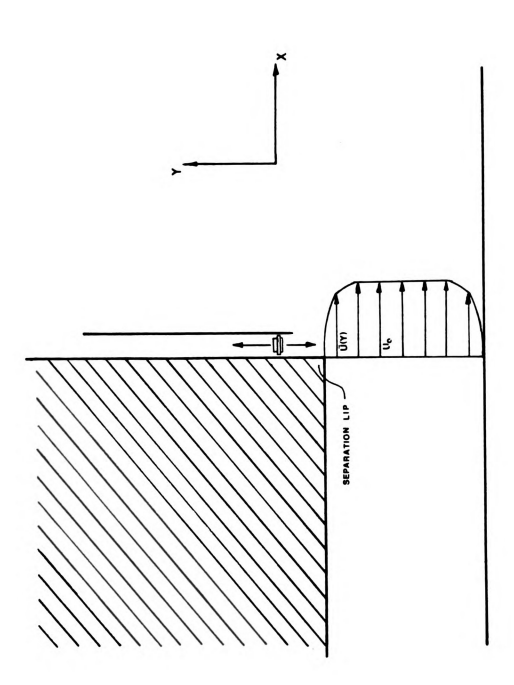
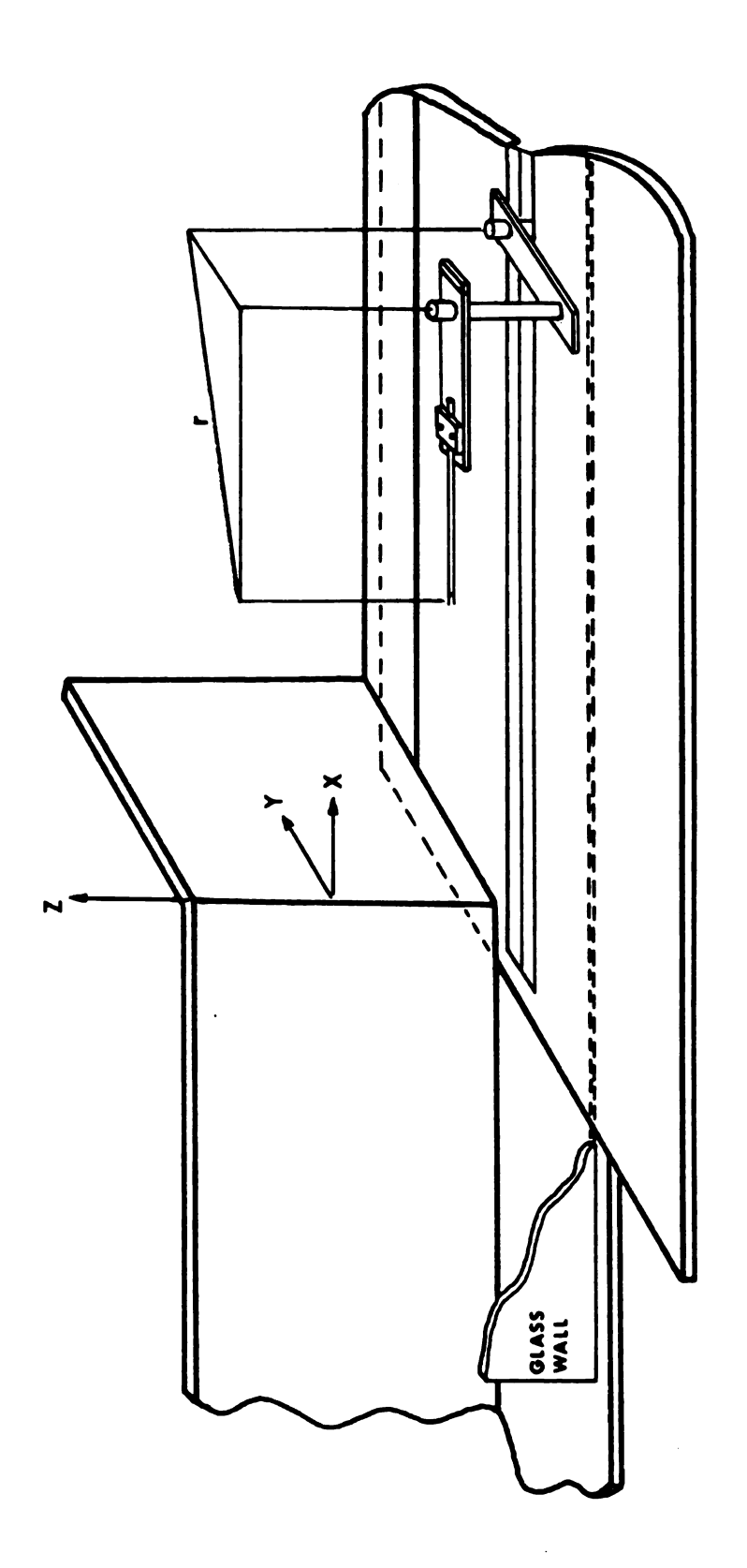


Figure 9b Schematic Representation of Excitation Placement and Movement



Schematic Representation of Probe and Support Arm used for low speed calibration Figure 10s

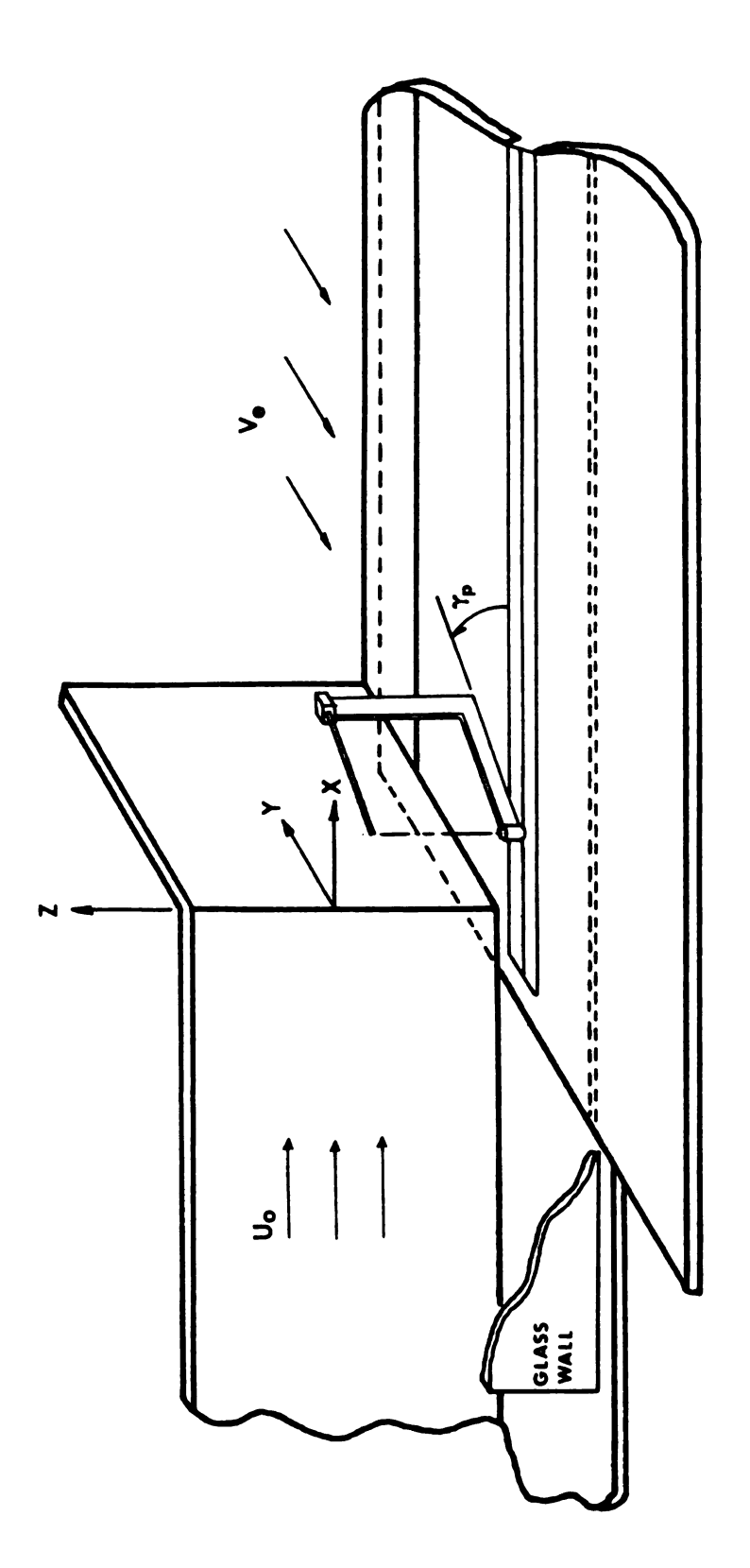


Figure 10b Schematic Representation of the Probe Positioning Unit

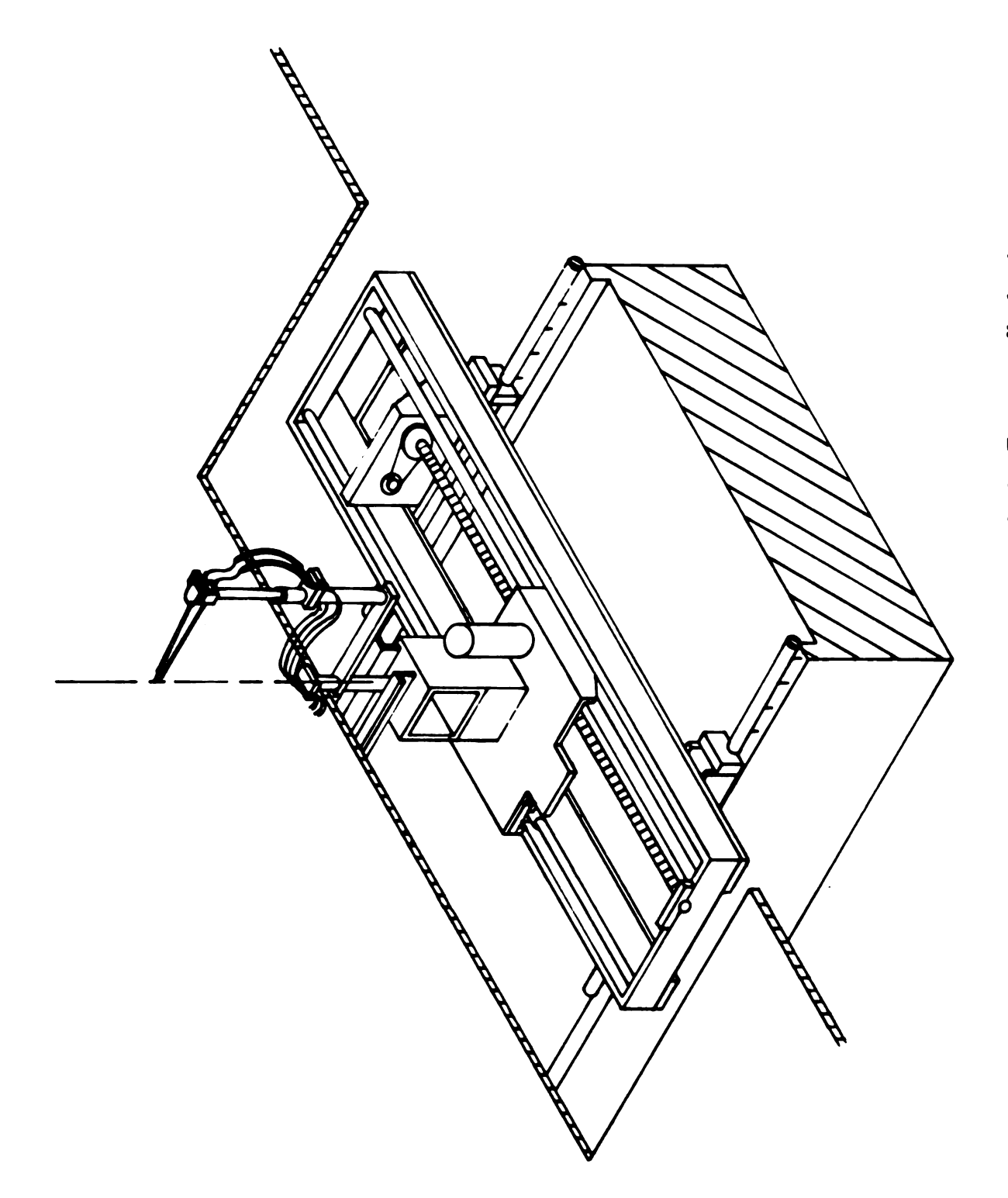


Figure 10c Schematic Representation of the Traverse Mechanism

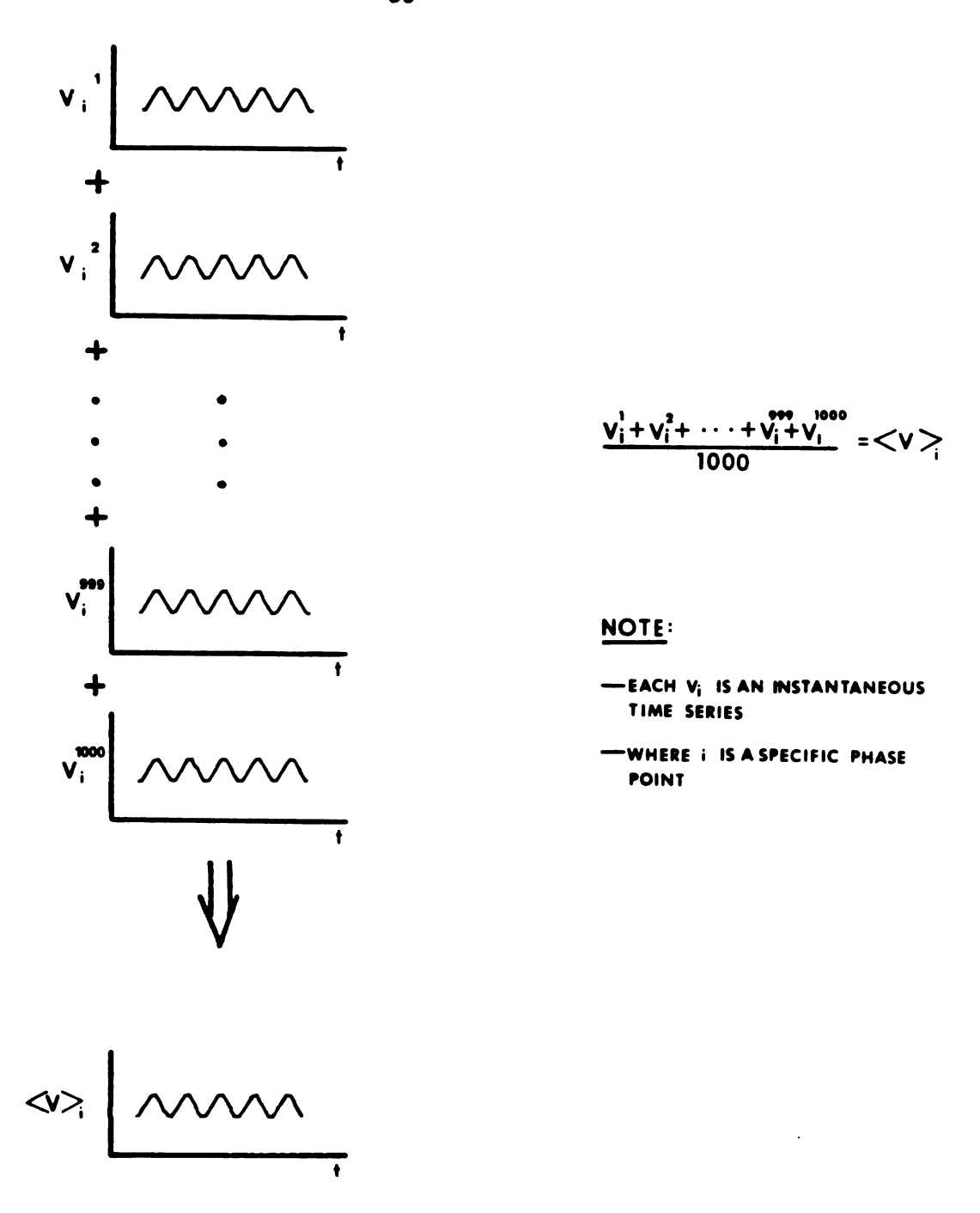
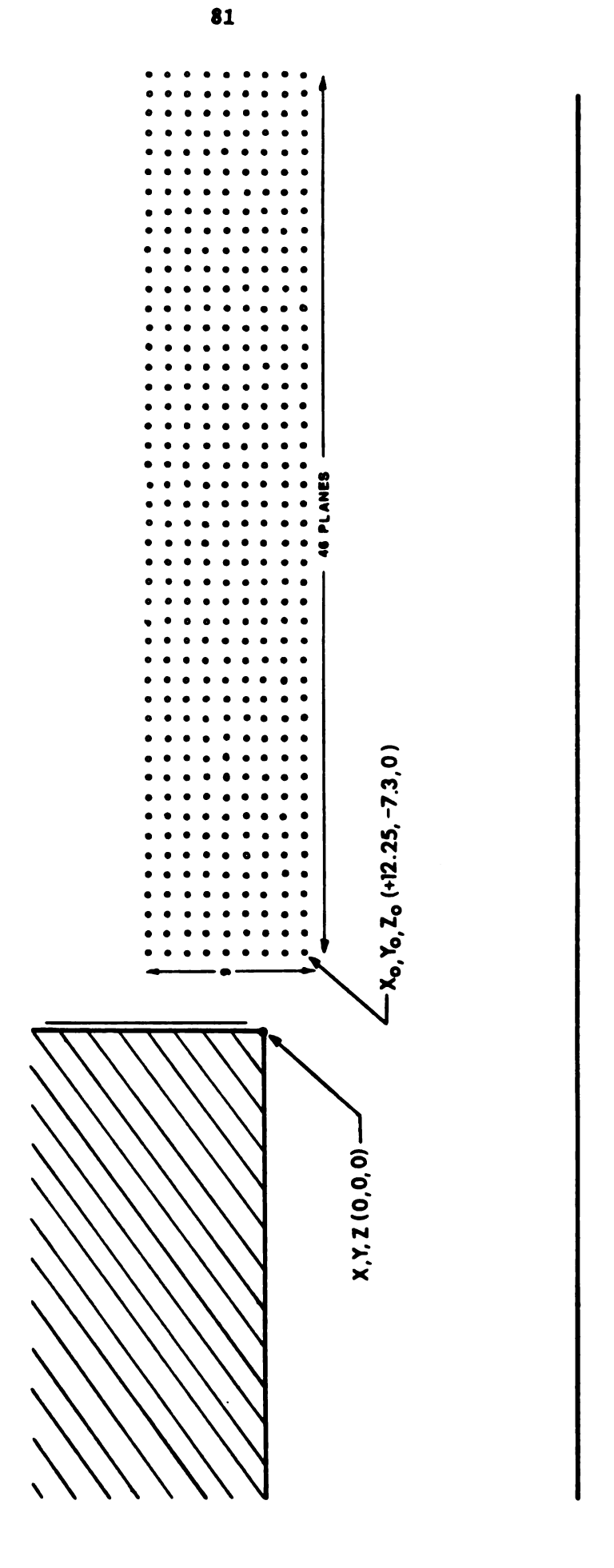


Figure 11 A Visual Representation of the Phase Averaging Technique



Schematic Representation of the Measurement Grid Figure 12

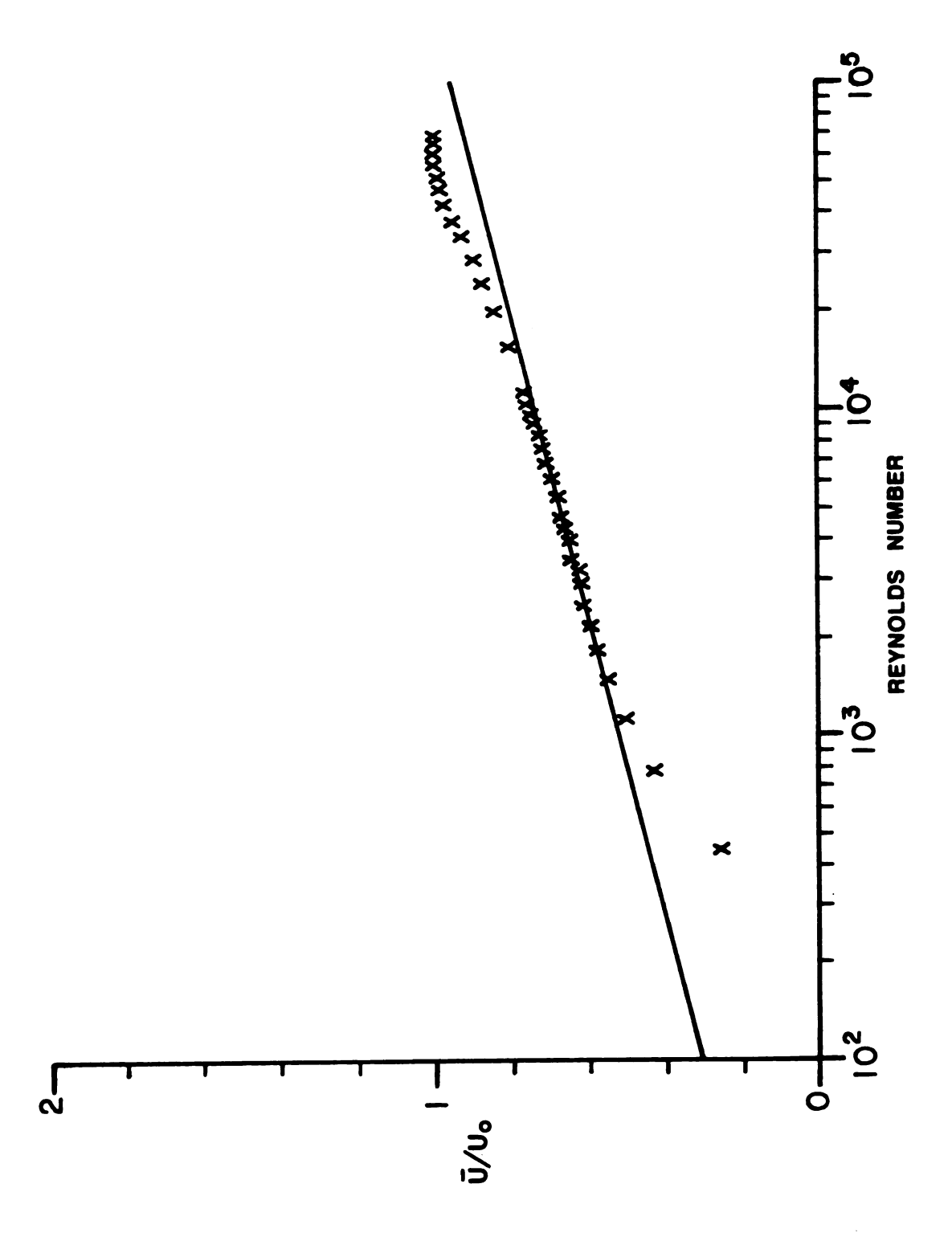
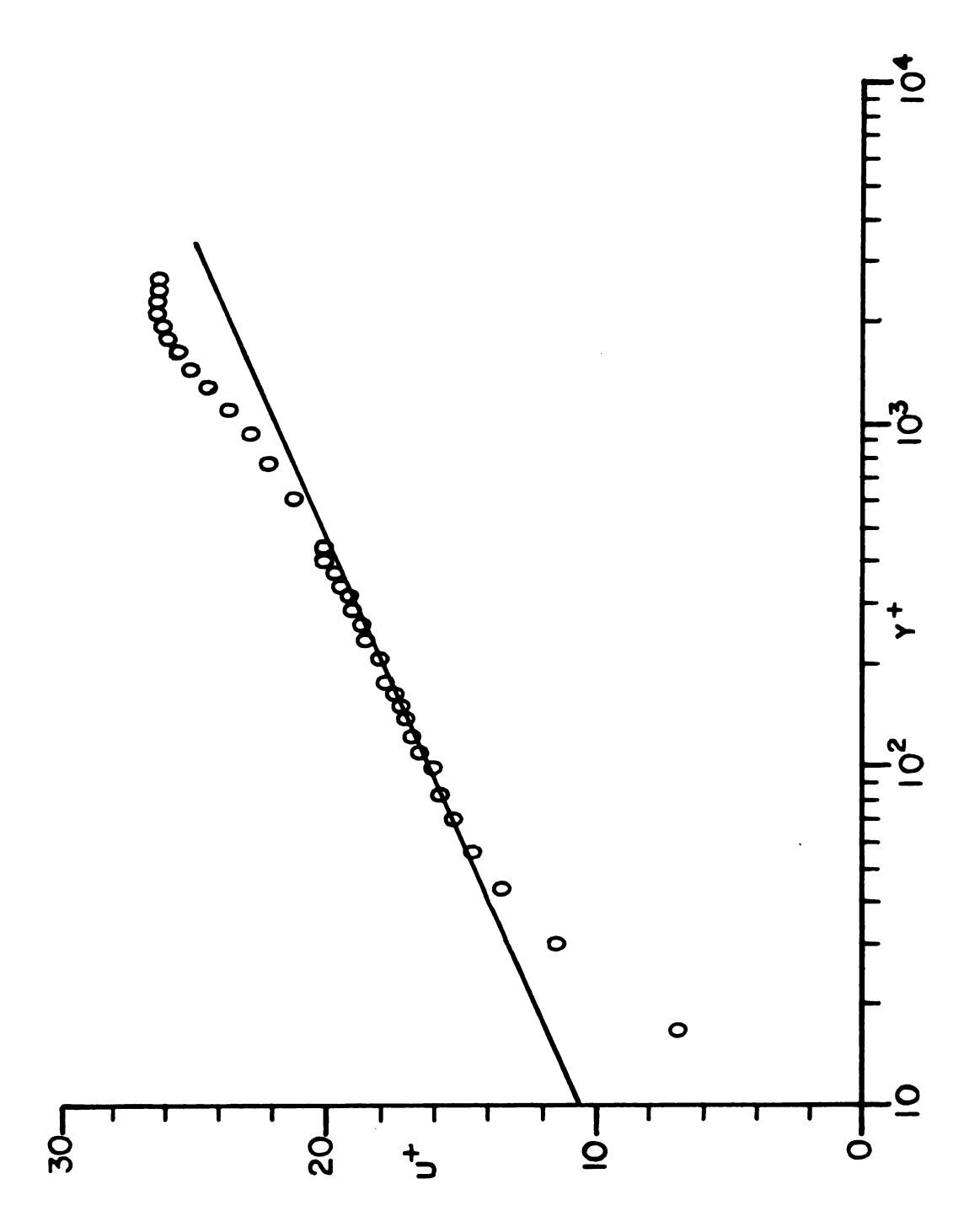
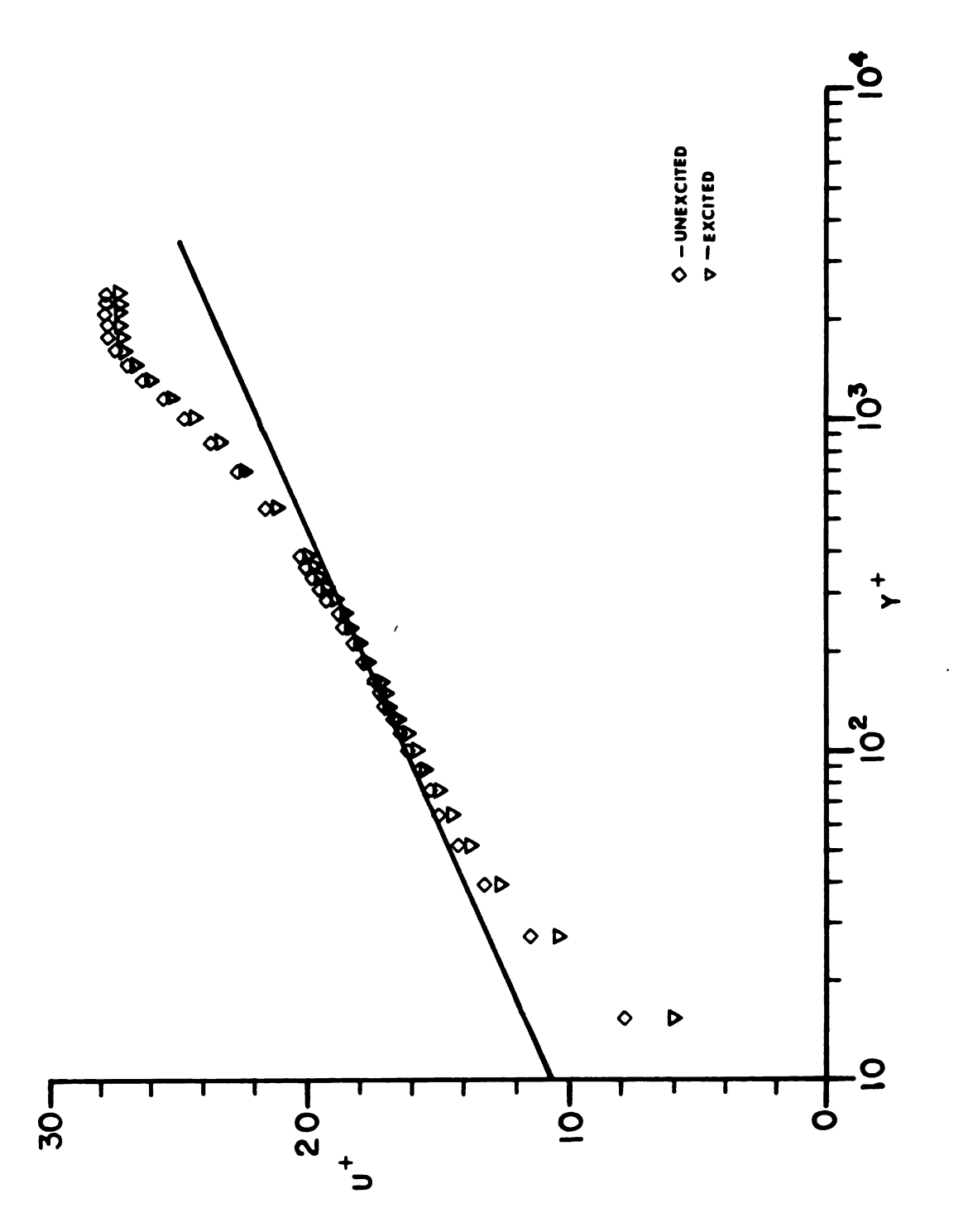


Figure 13a Clauser Plot of Data at X=-4.5 cm, Z=0.0 cm



13b Law of the Wall Plot of Data at X=-4.5 cm, Z=0.0 cm



Law of the Wall Plot of Data at X=-25 cm, Z=0.0 cm Figure 14

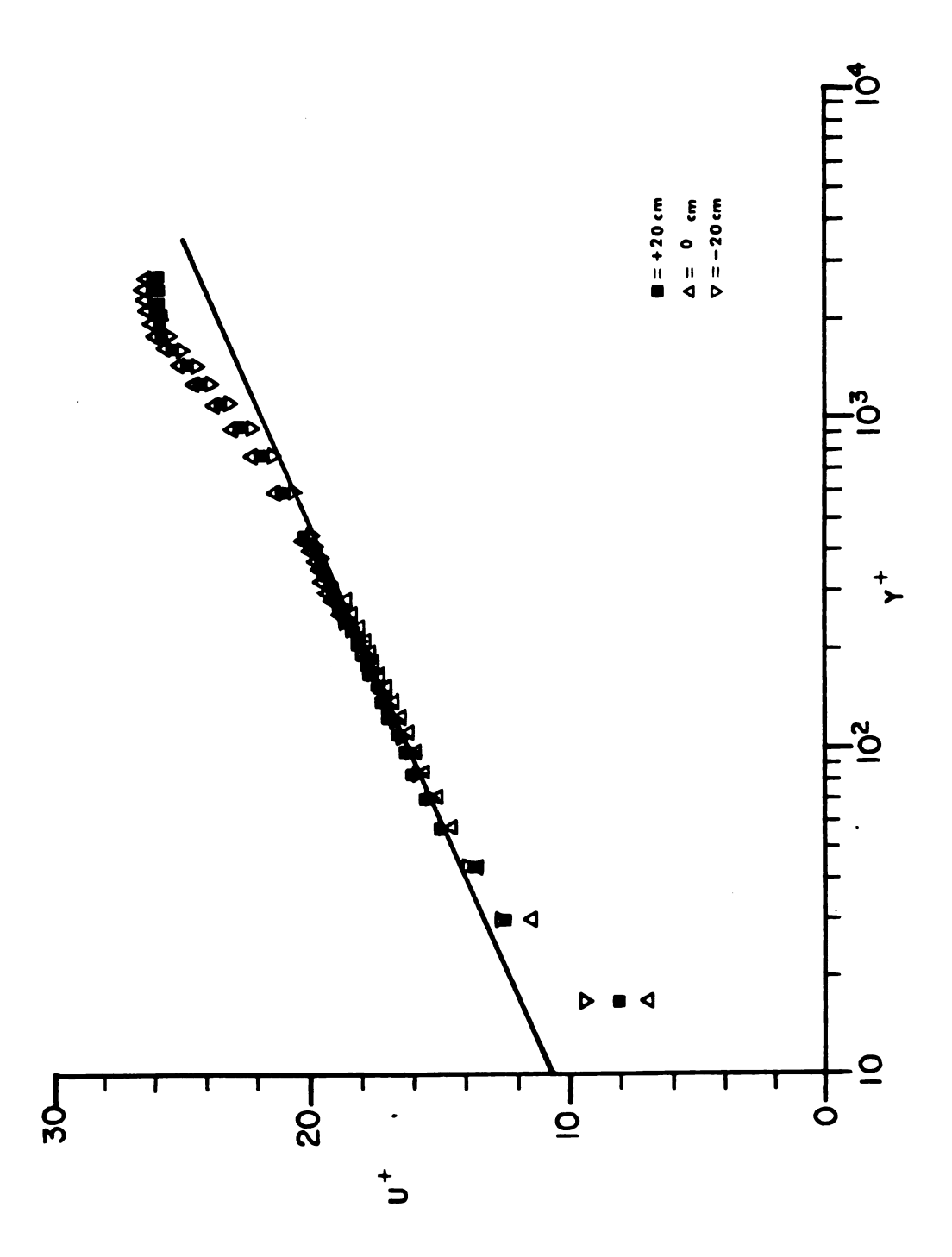
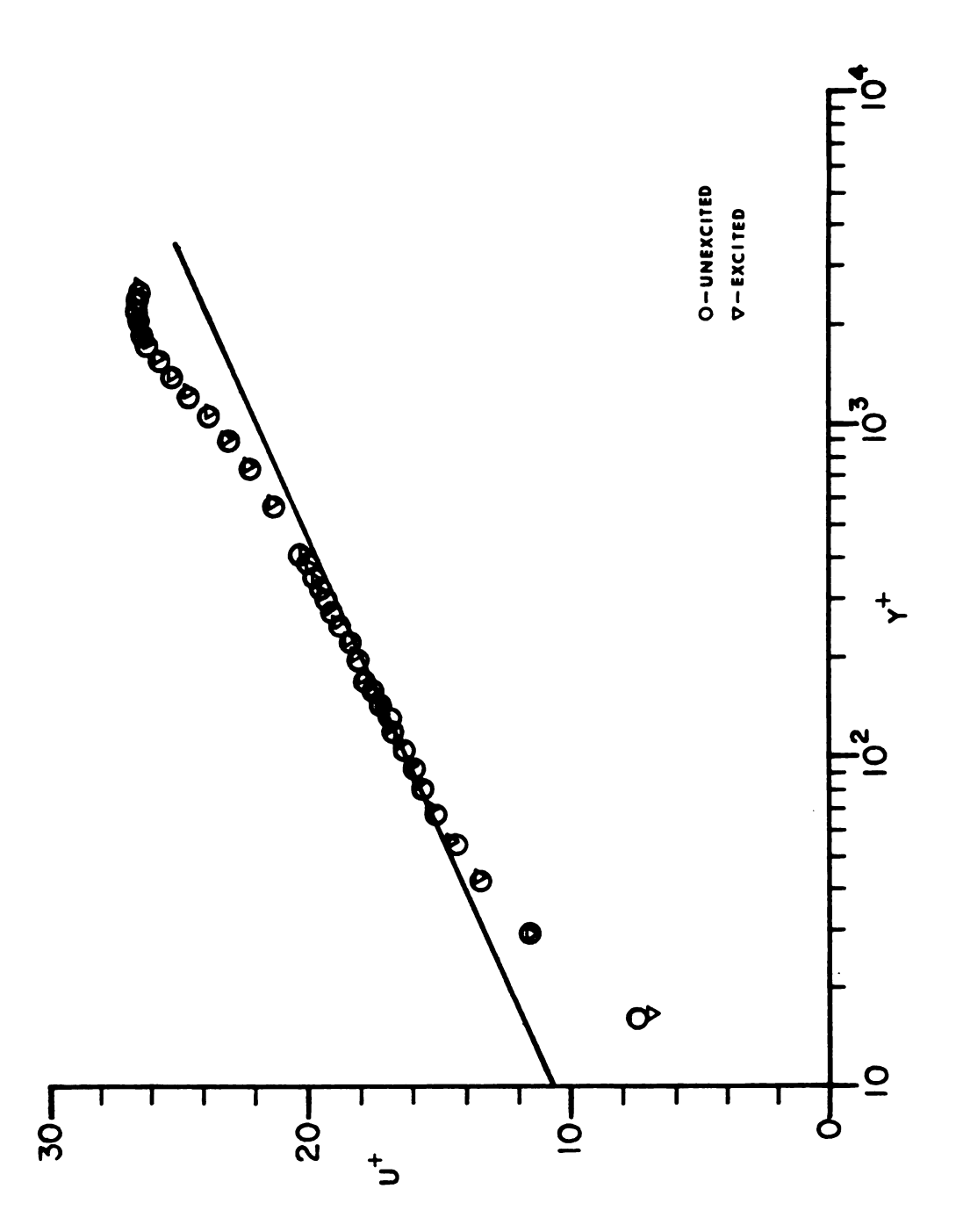
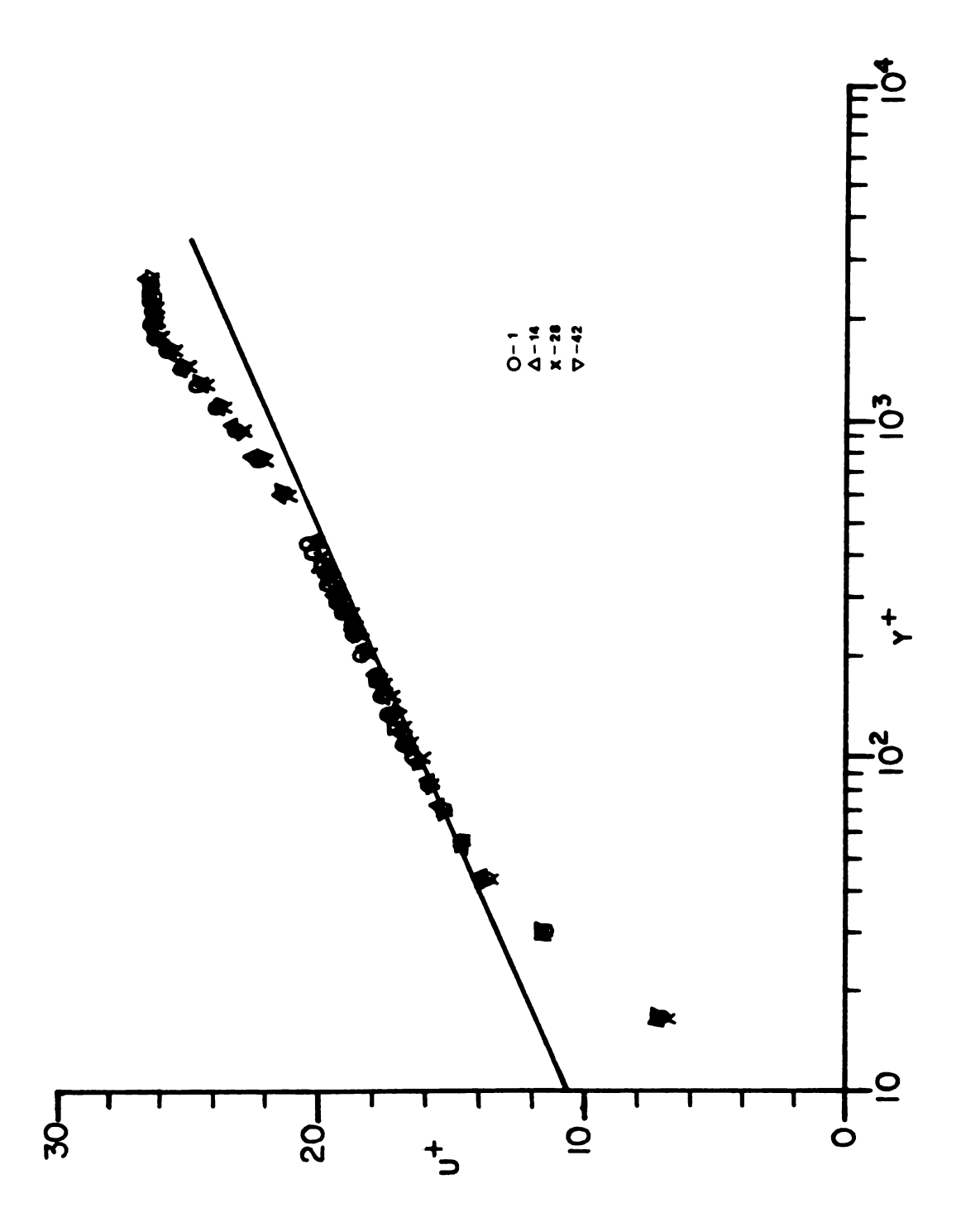


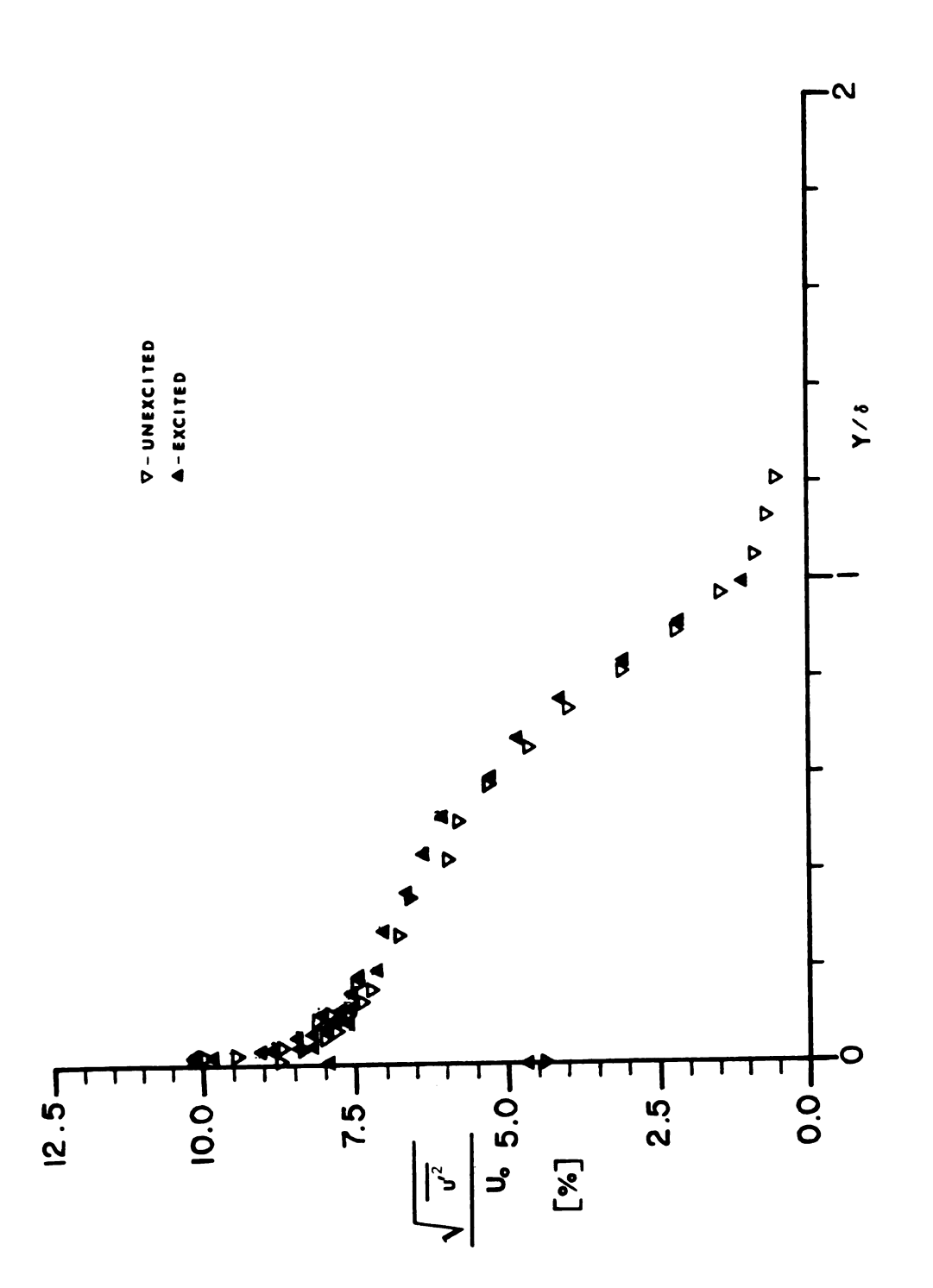
Figure 15 Law of the Wall Plot of Data at X=-4.5 cm, Z=0.0, ±20 cm



Law of the Wall Plot for Data at X=-4.5 cm, Z=0.0 cm, Excited and Unexcited Figure 16



Law of the Wall Plot for Data at X=-4.5 cm, Z=0.0 cm; Phase Points: 1, 14, 28 and 42 Figure 17



Streamwise Component of Turbulent Intensity for Data at X=-4.5 cm, Z=0.0 cm, Excited and Unexcited Figure 18

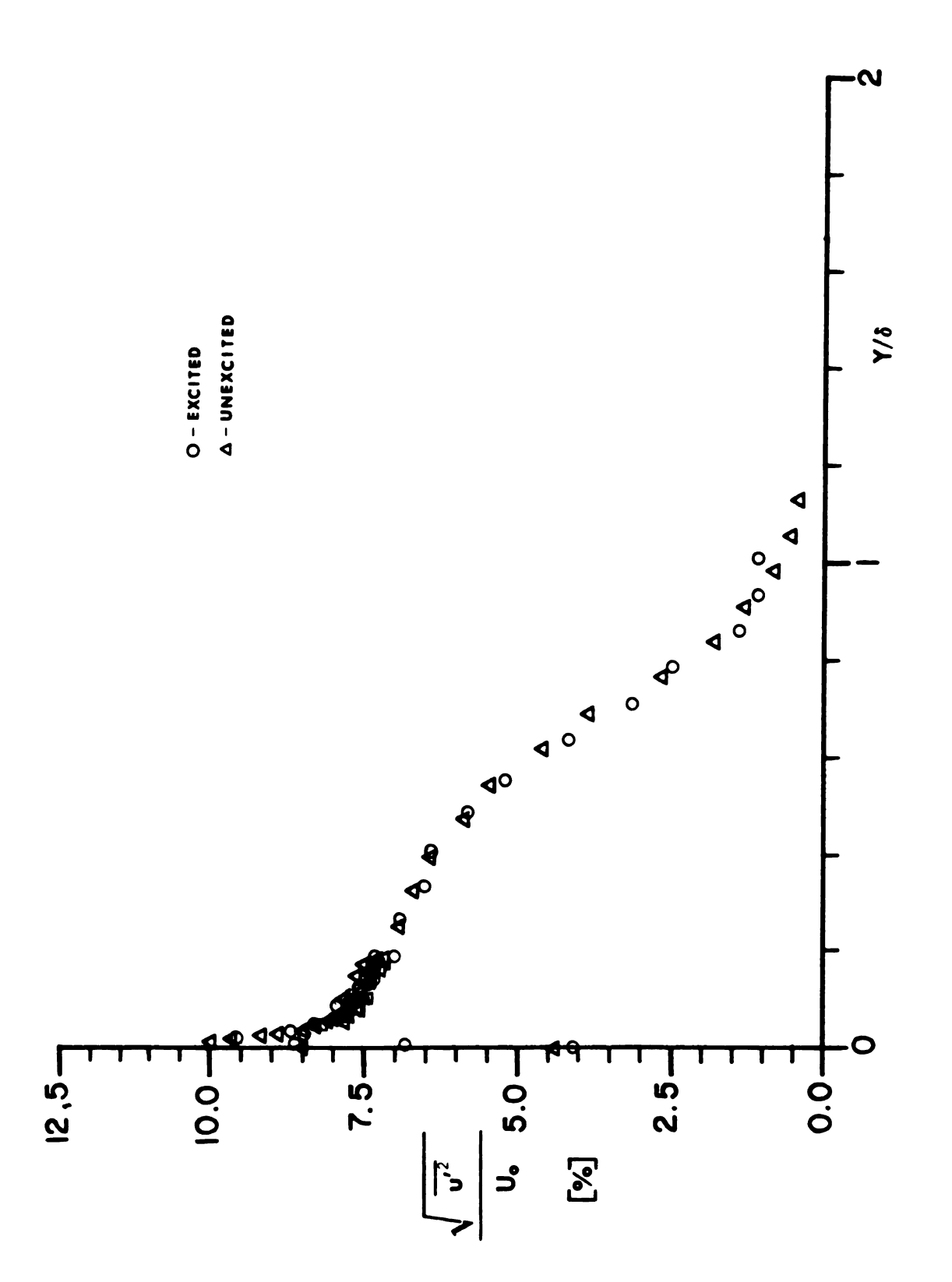


Figure 19 Streamwise Component of Turbulent Intensity for Data at X=-25 cm, Z=0.0 cm, Excited and Unexcited

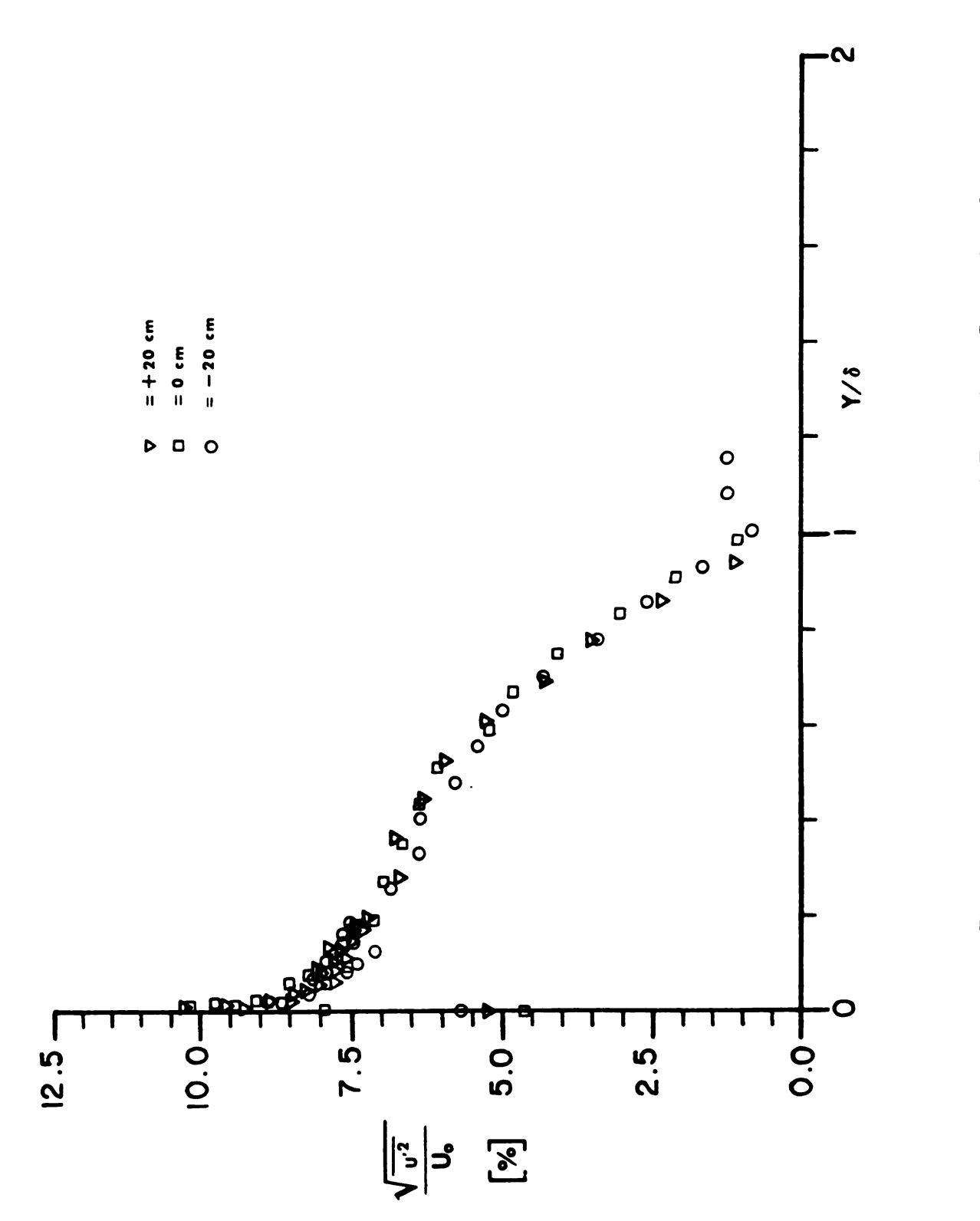
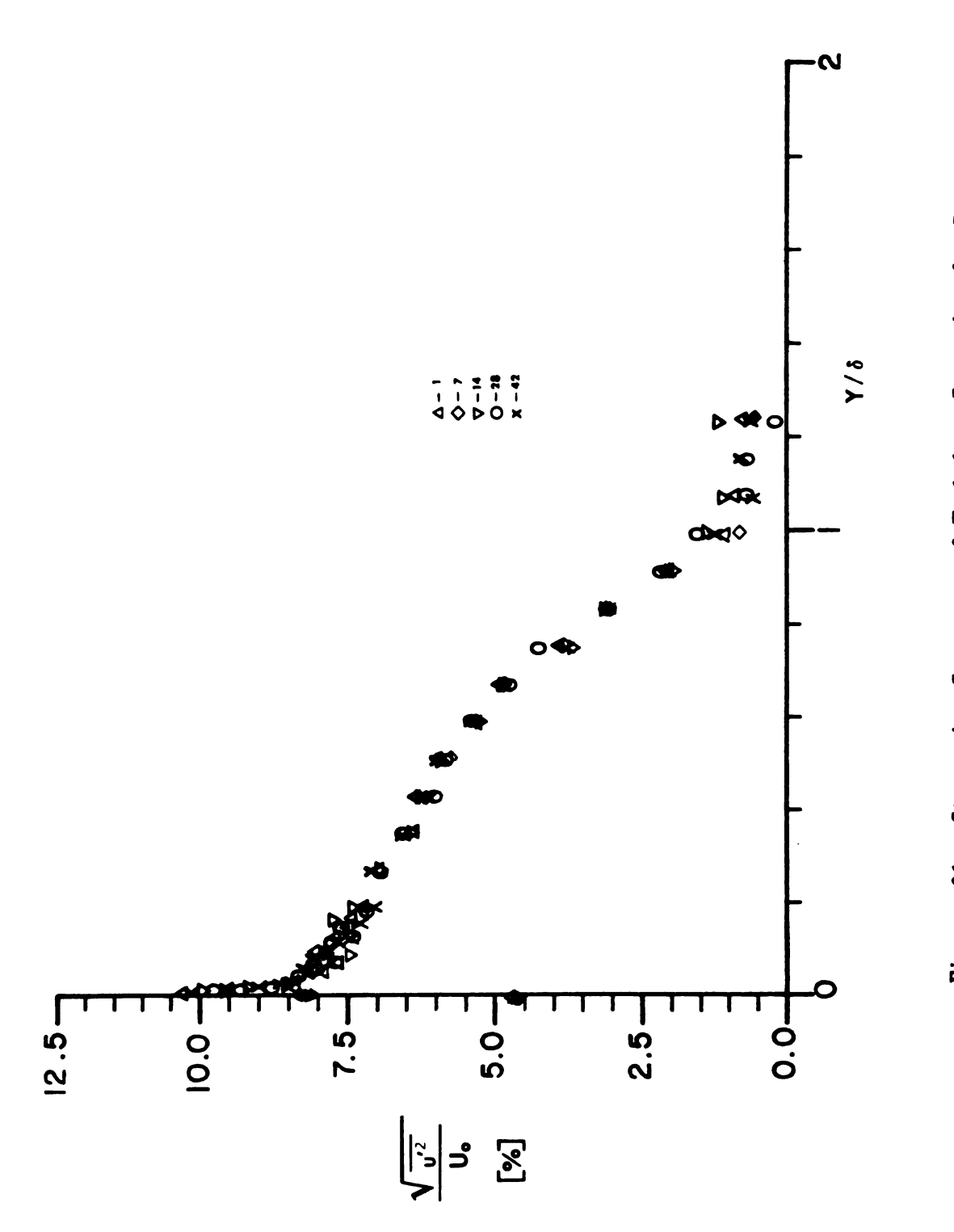


Figure 20 Streamwise Component of Turbulent Intensity for Data at X=-4.5 cm, Z=0.0 cm, ±20 cm



Streamwise Component of Turbulent Intensity for Data at X=-4.5 cm, Z=0.0 cm; Phase Points: 1, 7, 14, 28 and 42 Figure 21

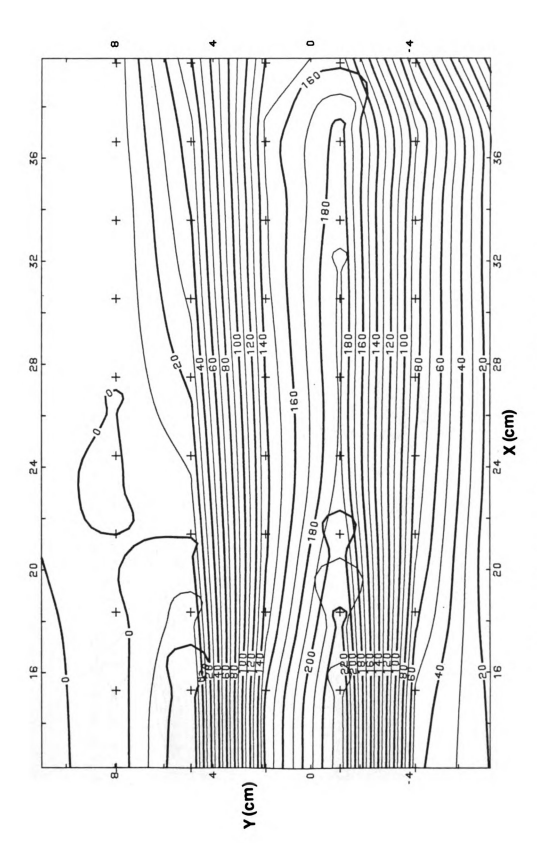


Figure 22 Phase Averaged Transverse Vorticity  $\langle \omega_{\rm g} \rangle_{1,i}$ Expanded Initial Region for W1

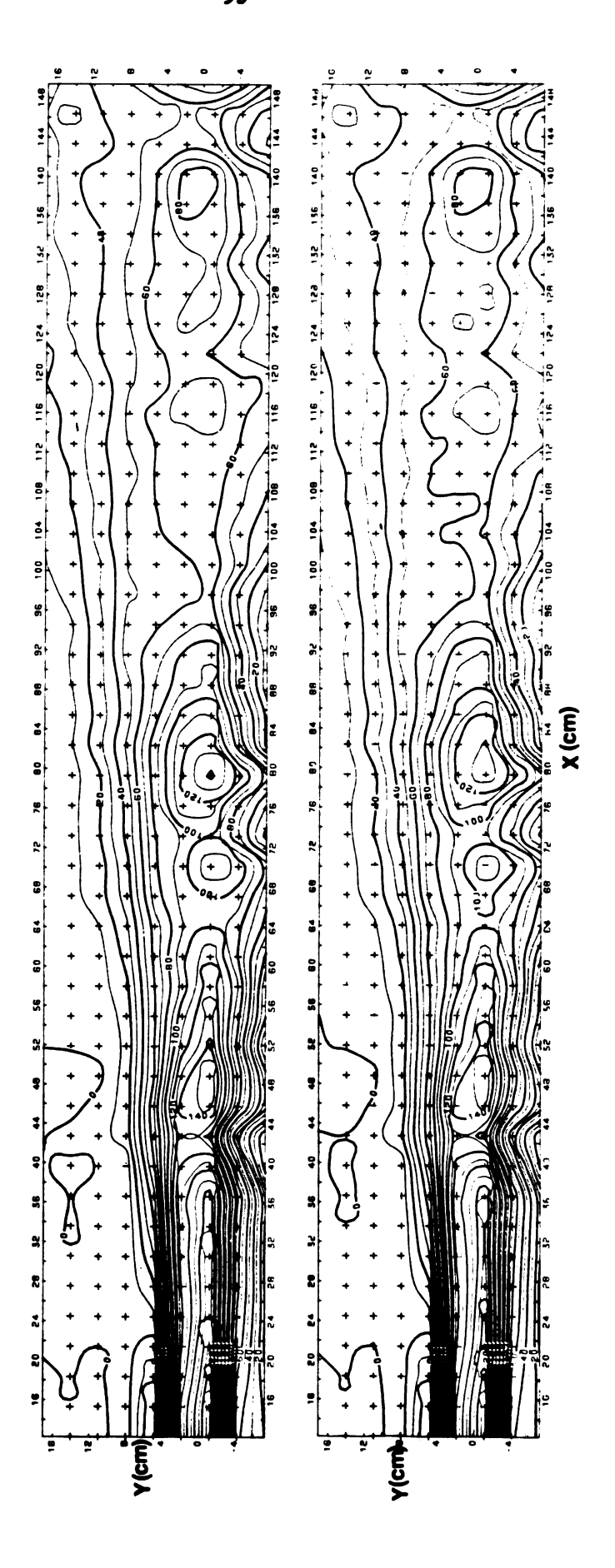


Figure 23 Phase Averaged Transverse Vorticity  $\langle \omega_{\rm Z} \rangle_{1}$ ; a)W1 and b)W63

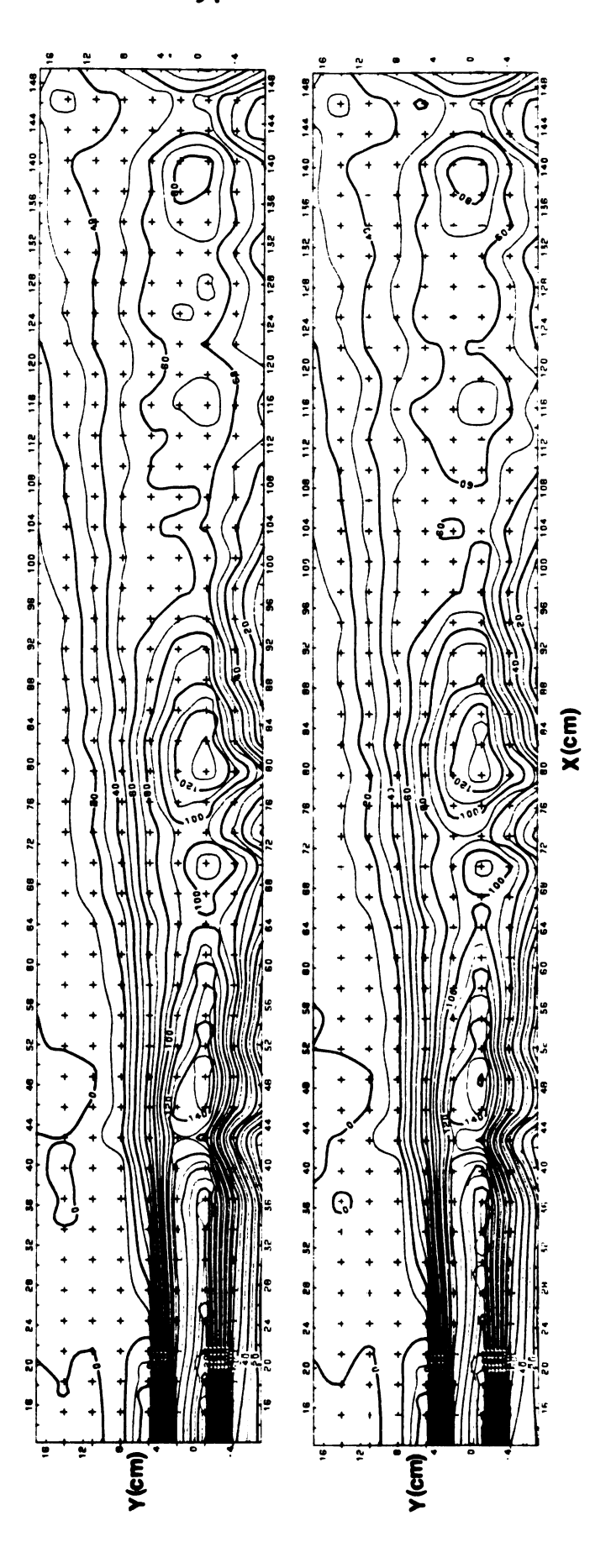


Figure 24 Phase Averaged Transverse Vorticity  $\langle \omega_{\mathbf{z}} \rangle_{\frac{1}{2}}$ ; a)W63 and b)W125

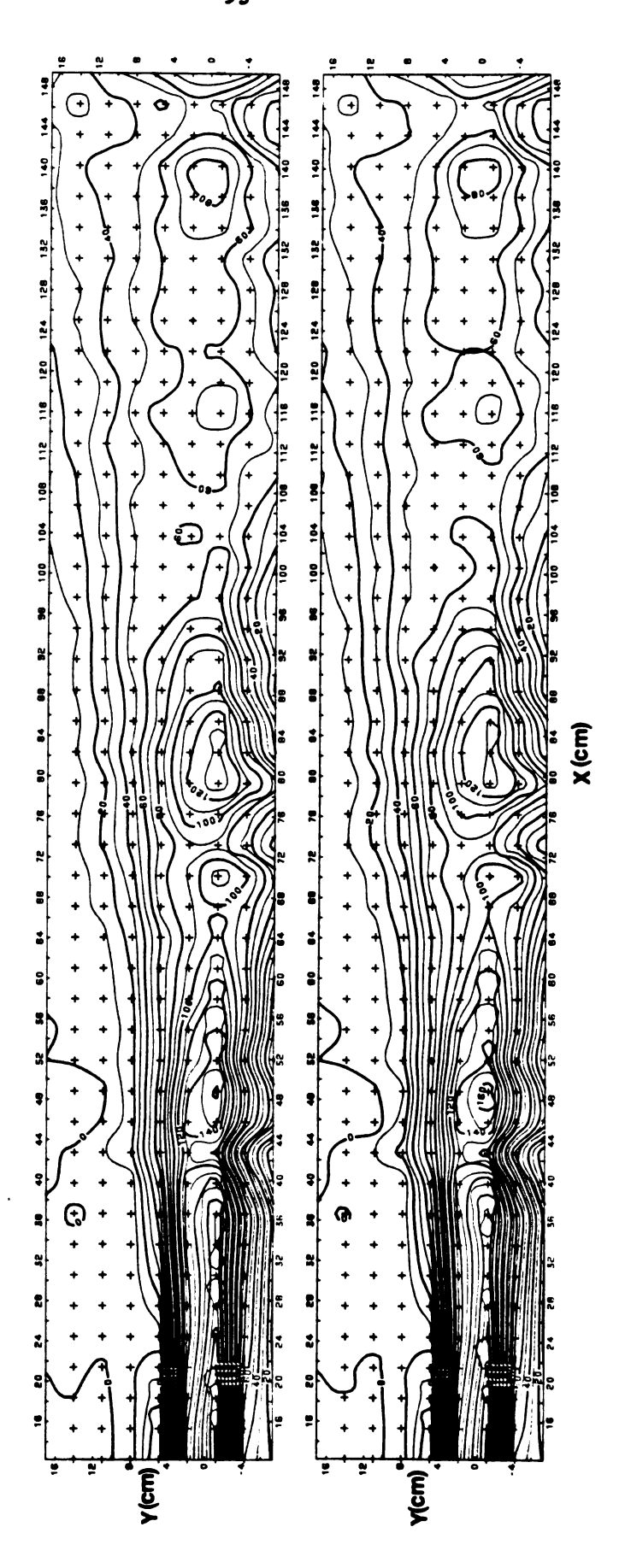


Figure 25 Phase Averaged Transverse Vorticity  $\langle \omega_{\rm Z} \rangle_{1}$ ; a) W125 and b) W187

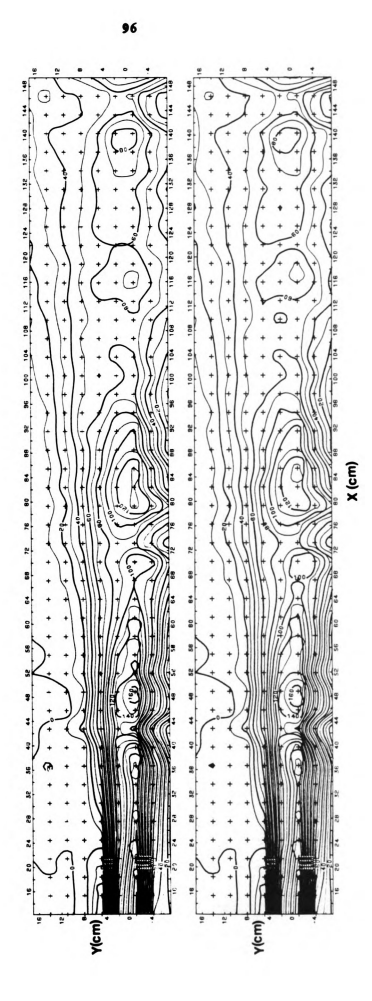


Figure 26 Phase Averaged Transverse Vorticity  $\langle \omega_{\rm z} \rangle_{\rm j}$ ; a) W187 and b)W227

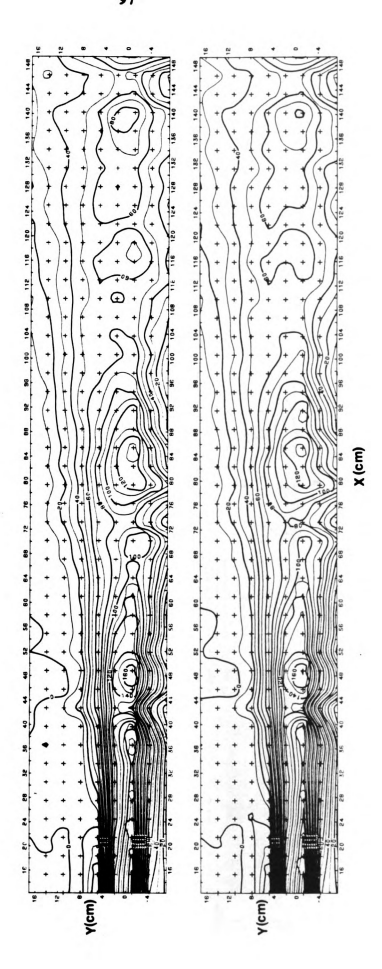


Figure 27 Phase Averaged Transverse Vorticity  $\langle \omega_{\rm z} \rangle_{1}$ ; a) W227 and b) W289

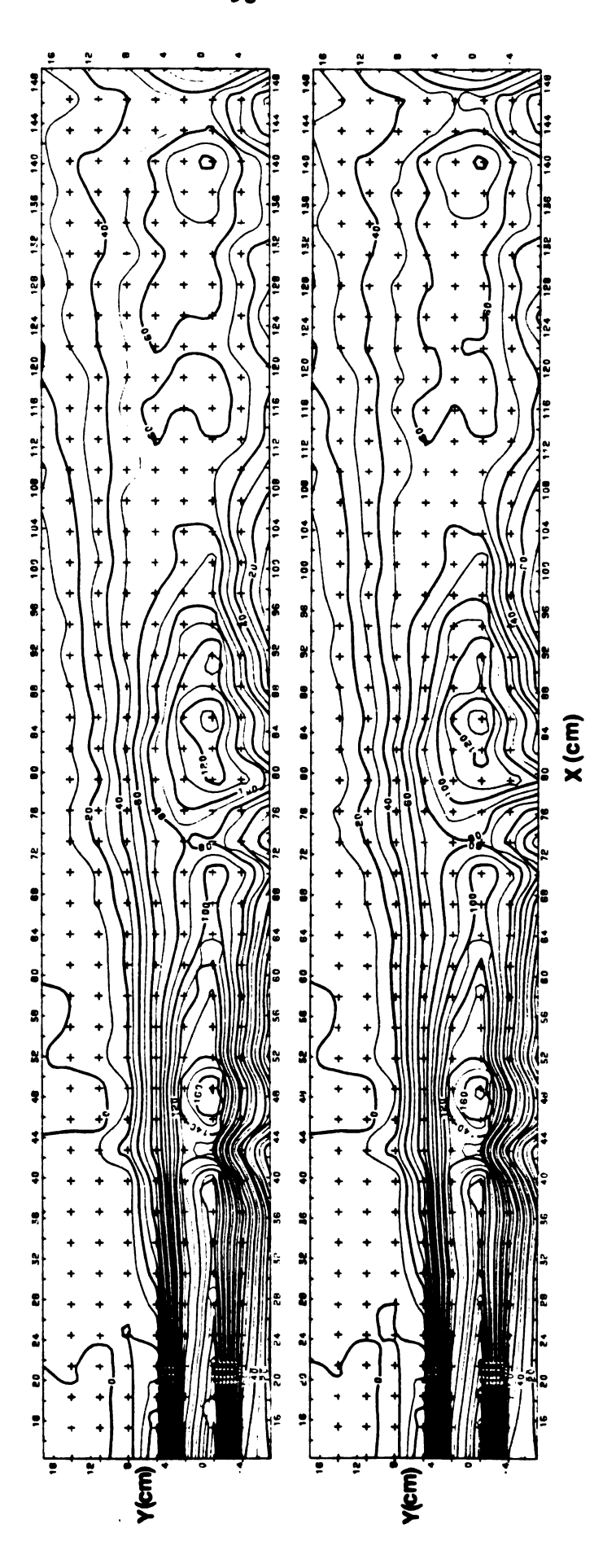


Figure 28 Phase Averaged Transverse Vorticity  $\langle \omega_{\rm Z} \rangle_{1}$ ; a) W289 and b) W320

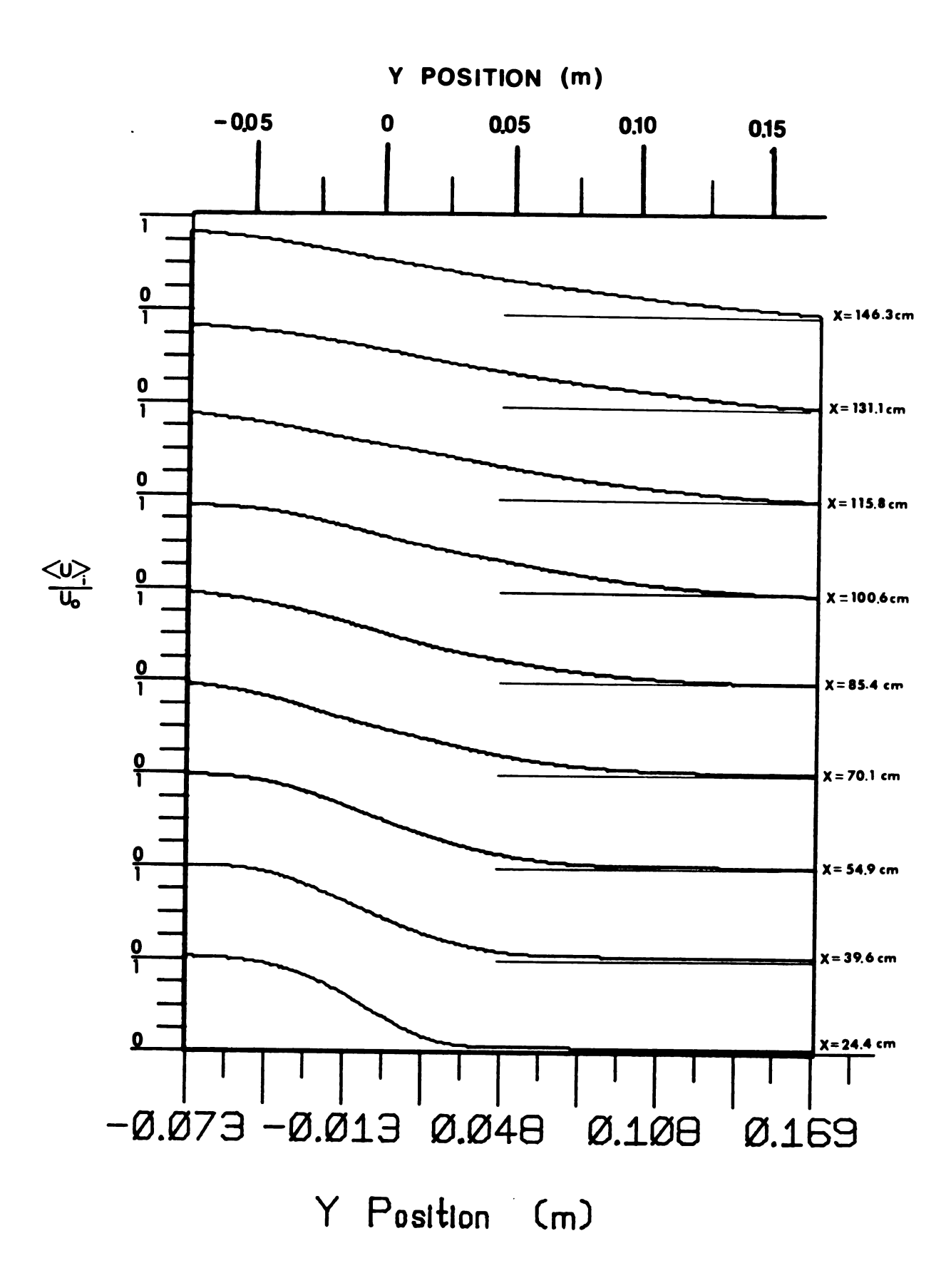


Figure 29 Phase Averaged Non-dimensional Velocity Profiles; For Phase Point, i=320 and at X=24.4, 39.6, 54.9, 70.1, 85.4, 100.6, 115.8, 131.1, 146.3 cm

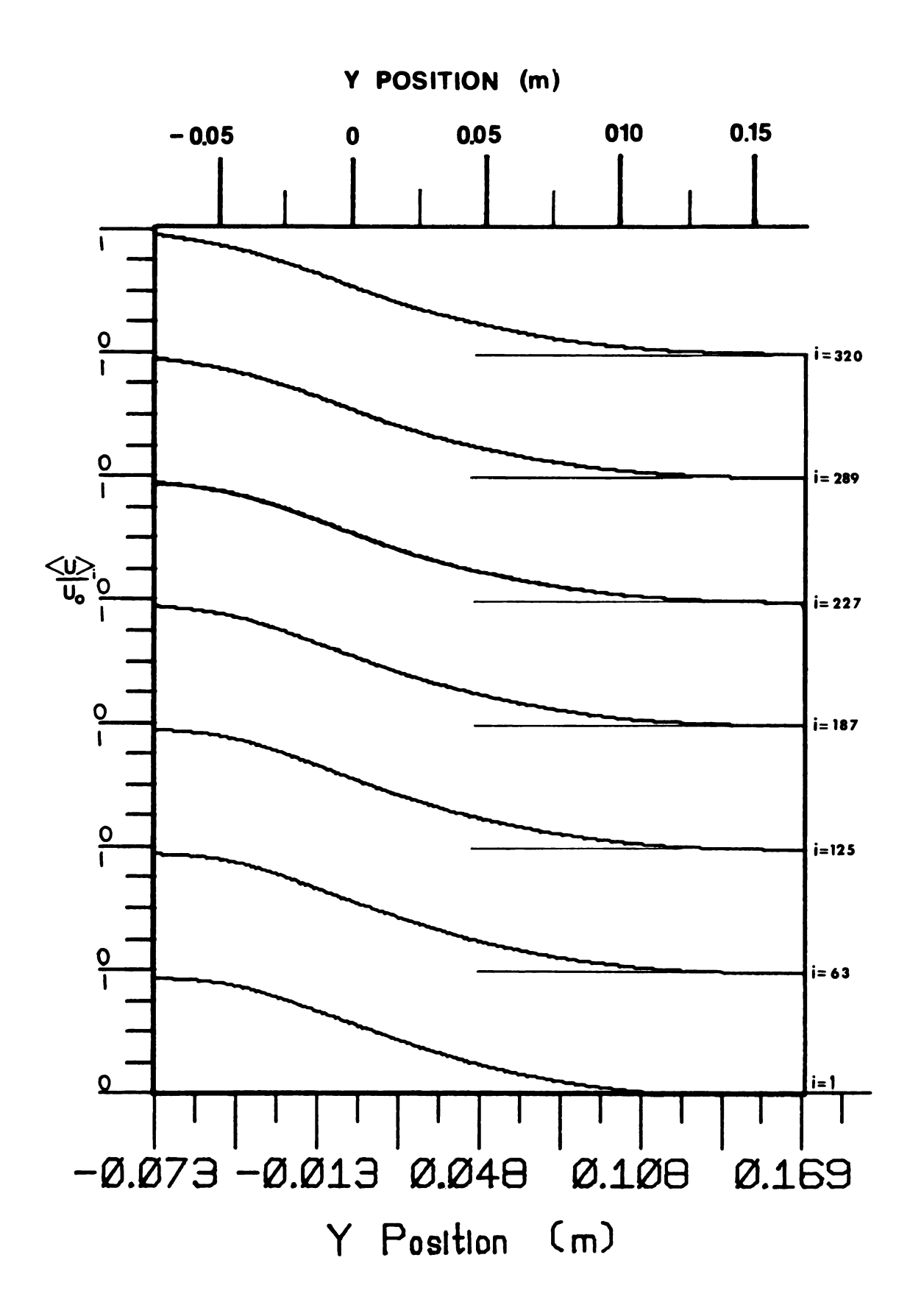
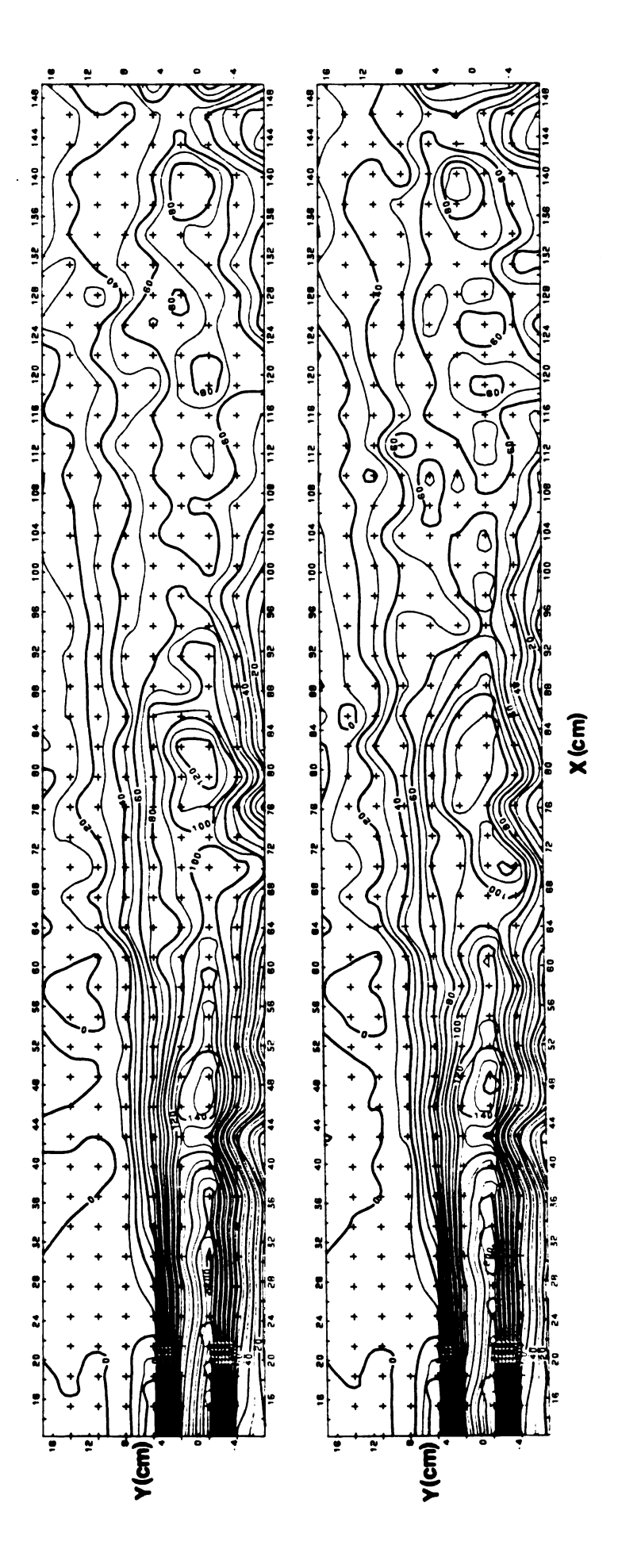
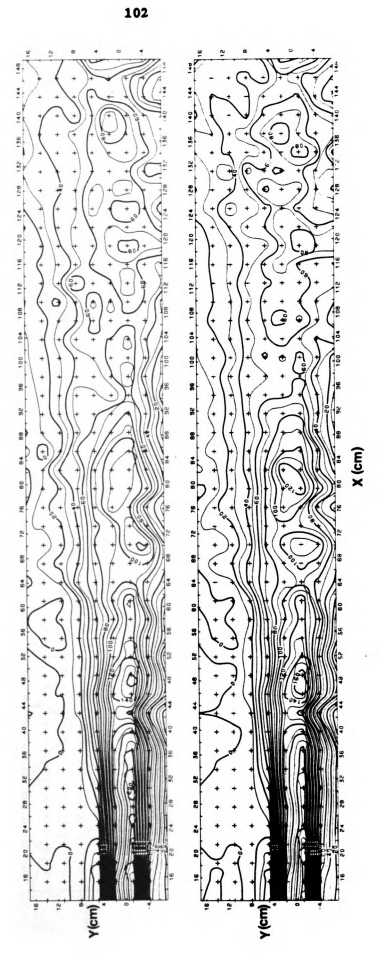


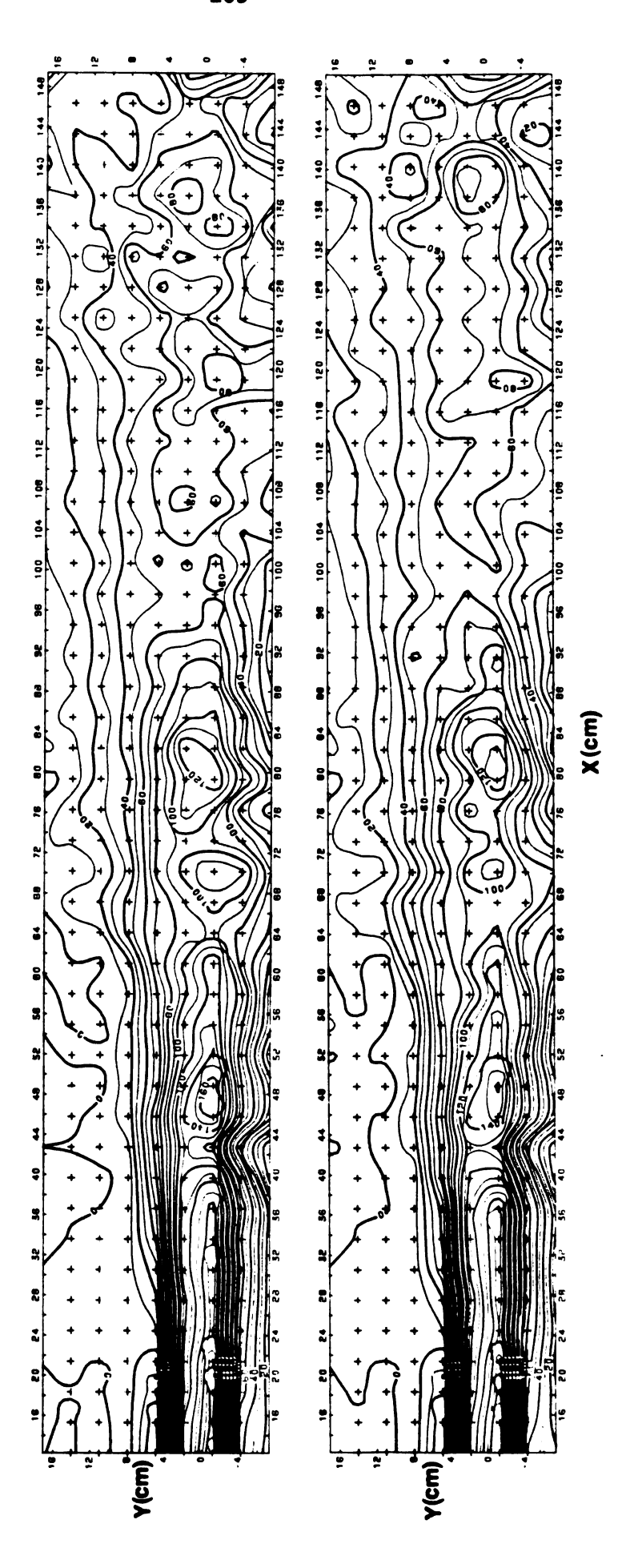
Figure 30 Phase Averaged Non-dimensional Velocity Profiles; at X=85.4 cm and i=1, 63, 125, 187, 227, 289 and 320.



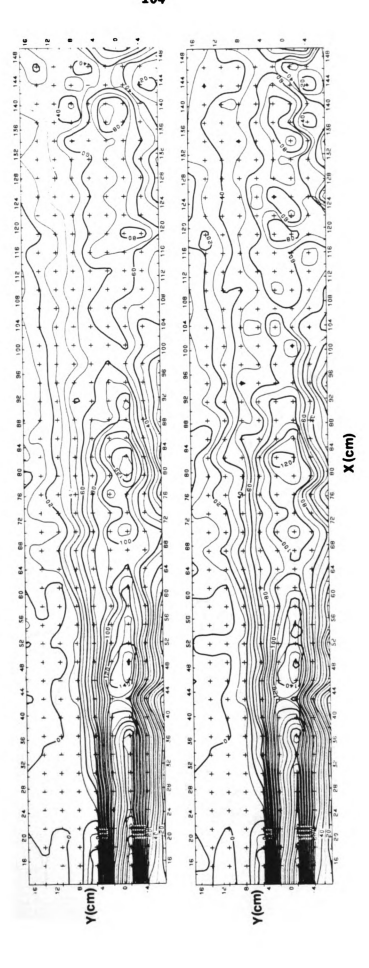
Perturbed Phase Averaged Transverse Vorticity,  $\langle \omega_z^D \rangle_i$ ; a) WP1 and b) WP63 Figure 31



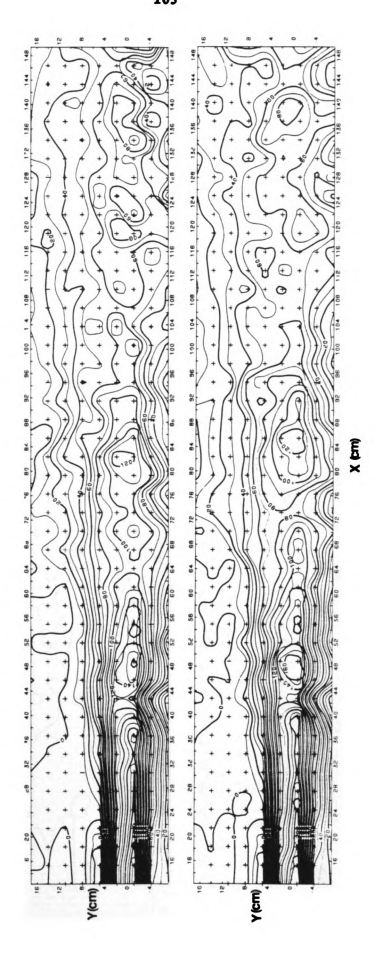
Perturbed Phase Averaged Transverse Vorticity,  $\langle \omega_{\rm L}^{\rm D} \rangle_{1}$ ; a)WP63 and b)WP125 Figure 32



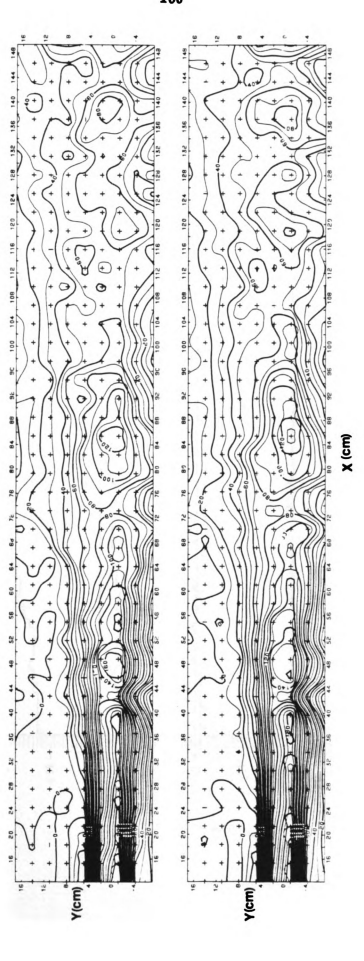
Perturbed Phase Averaged Transverse Vorticity,  $\langle\omega_z^D\rangle_{1}$  ; a) WP125 and b) WP187 Figure 33



Perturbed Phase Averaged Transverse Vorticity,  $\langle \omega_2^2 \rangle_{\frac{1}{2}}$ ; a) WP187 and b) WP27 Figure 34



Perturbed Phase Averaged Transverse Vorticity,  $\langle\omega_{L}^{D}\rangle_{\frac{1}{2}};$  a)#P227 and b)#P289 Figure 35



Perturbed Phase Averaged Transverse Vorticity,  $\langle \omega_{Z}^{p} \rangle_{1};$  a)WP289 and b)WP320 Figure 36

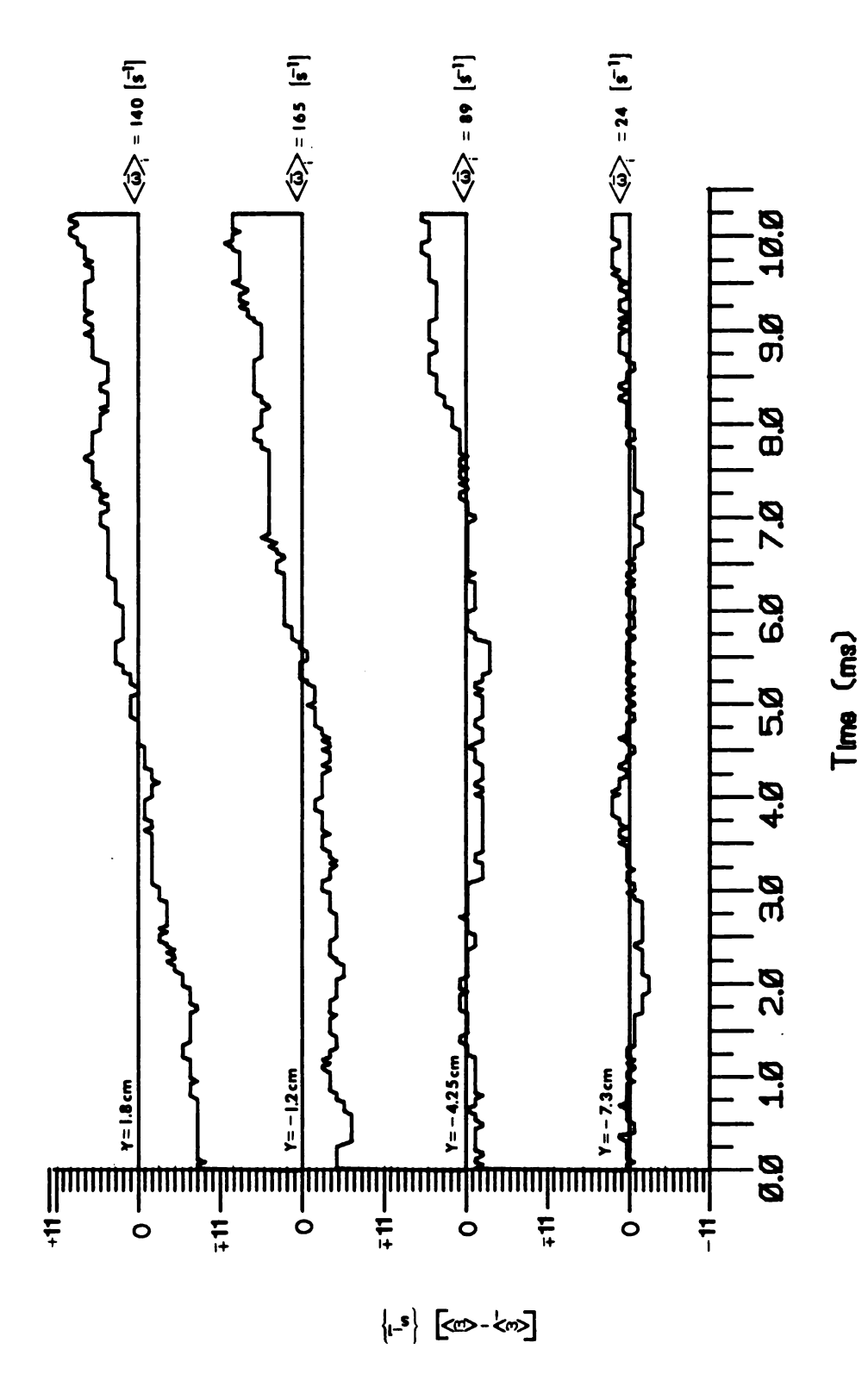


Figure 37a Phase Averaged Transverse Vorticity Time Series at X=48.8 cm and Y= -7.3, -4.3, -1.2 and 1.8 cm

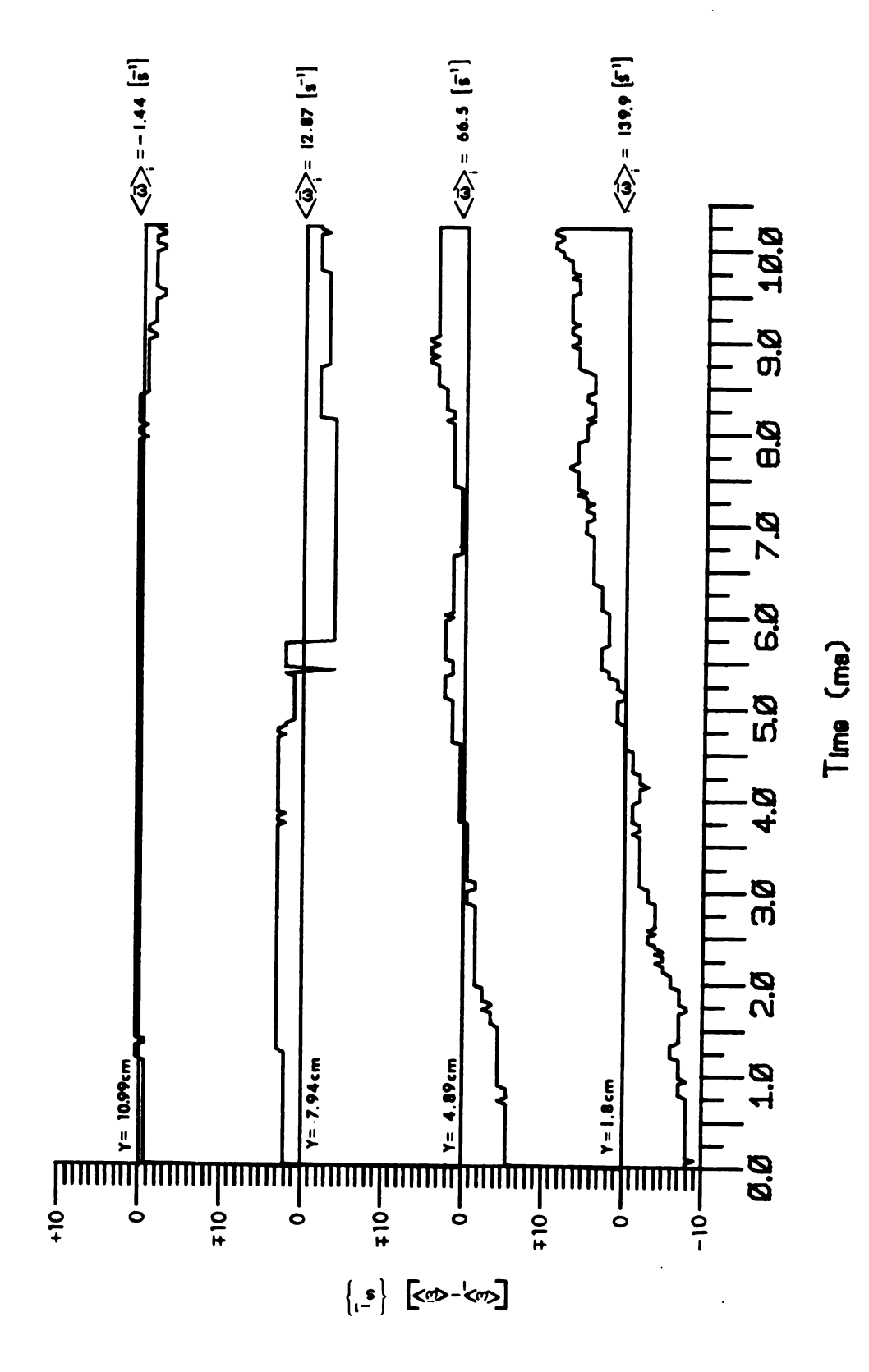


Figure 37b Phase Averaged Transverse Vorticity Time Series at X=48.8 cm and Y= 1.8, 4.9, 7.9 and 11.0 cm

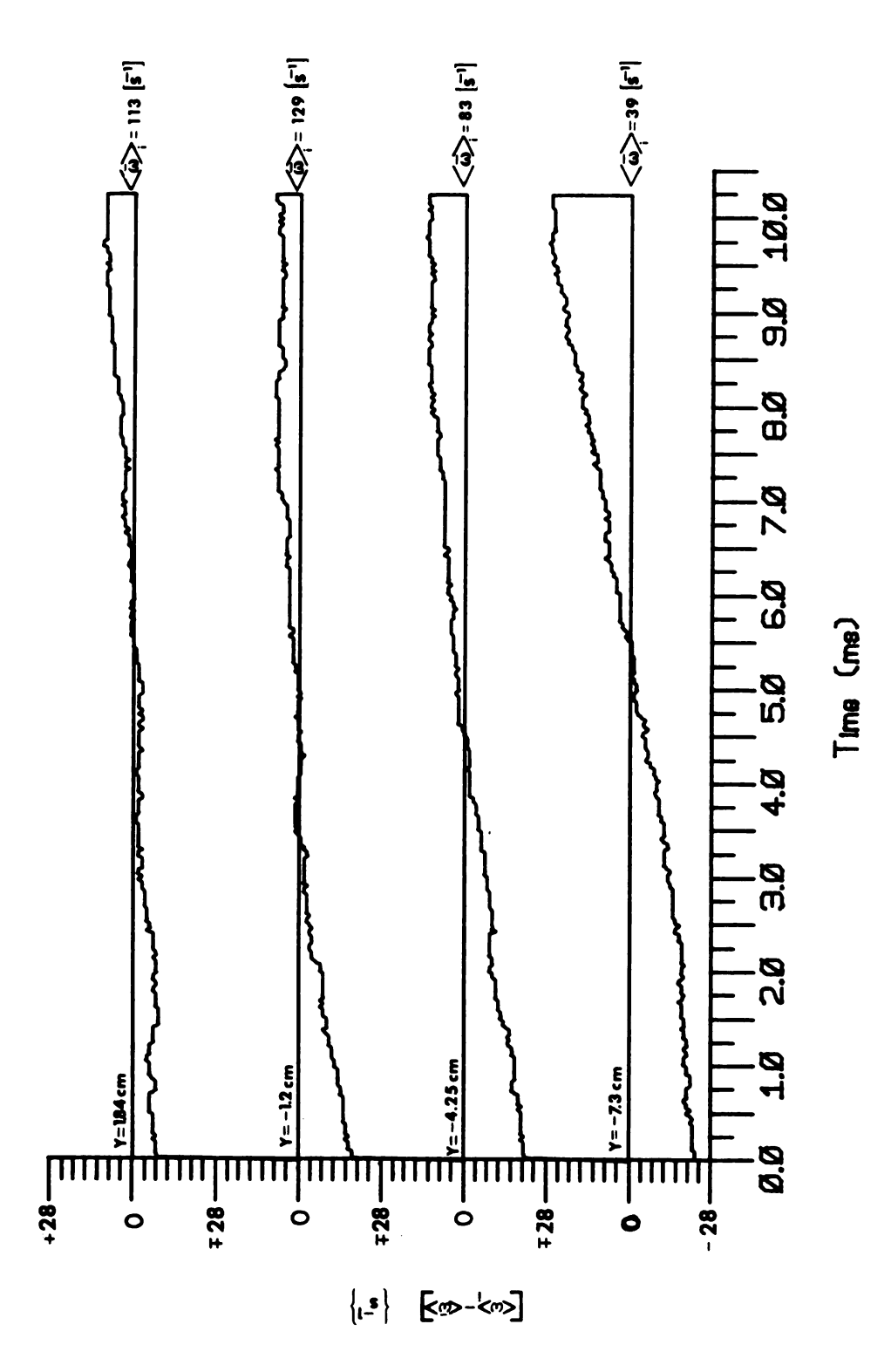


Figure 38a Phase Averaged Transverse Vorticity Time Series at X=85.4 cm and Y= -7.3, -4.3, -1.2 and 1.8 cm

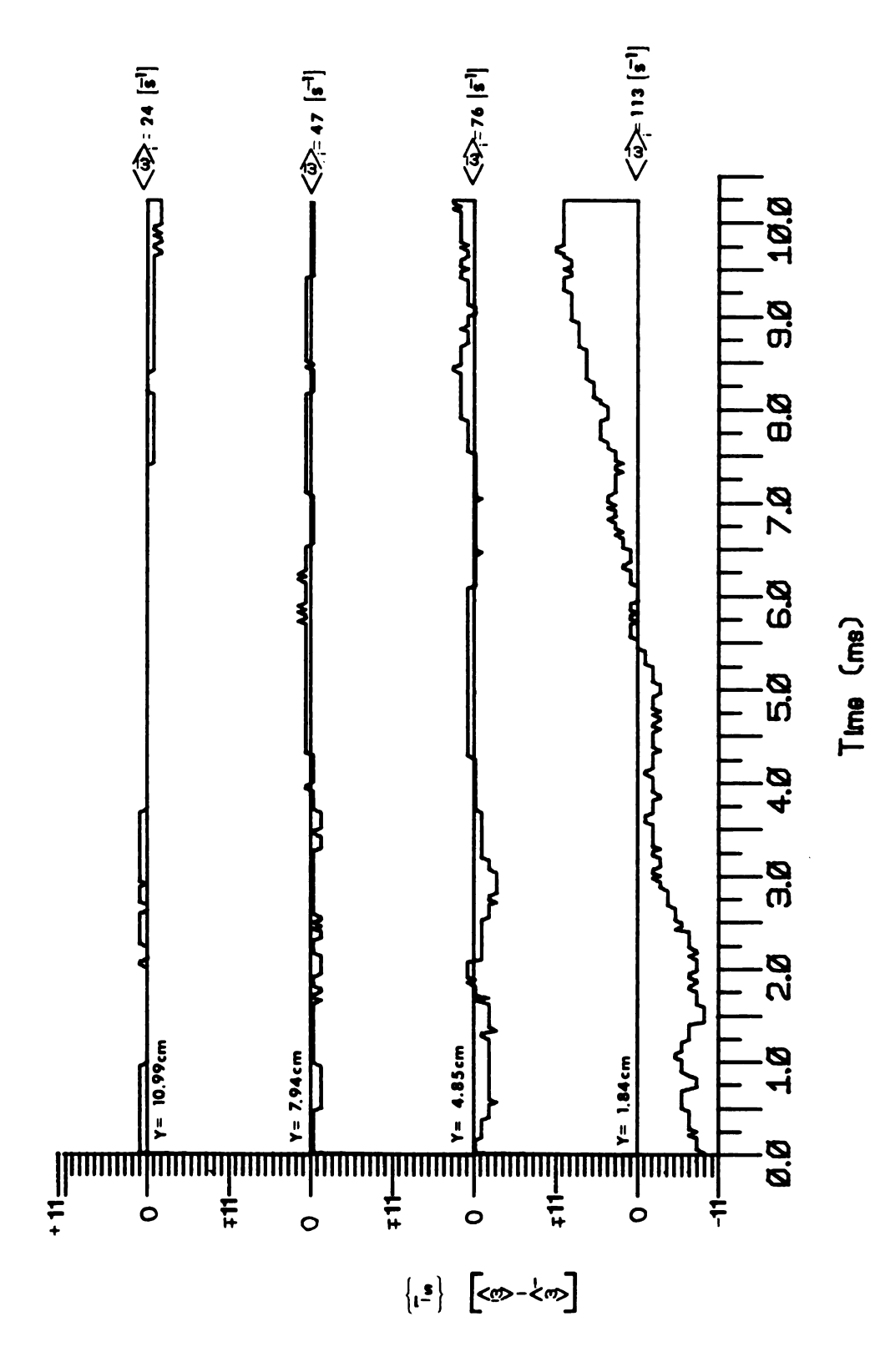
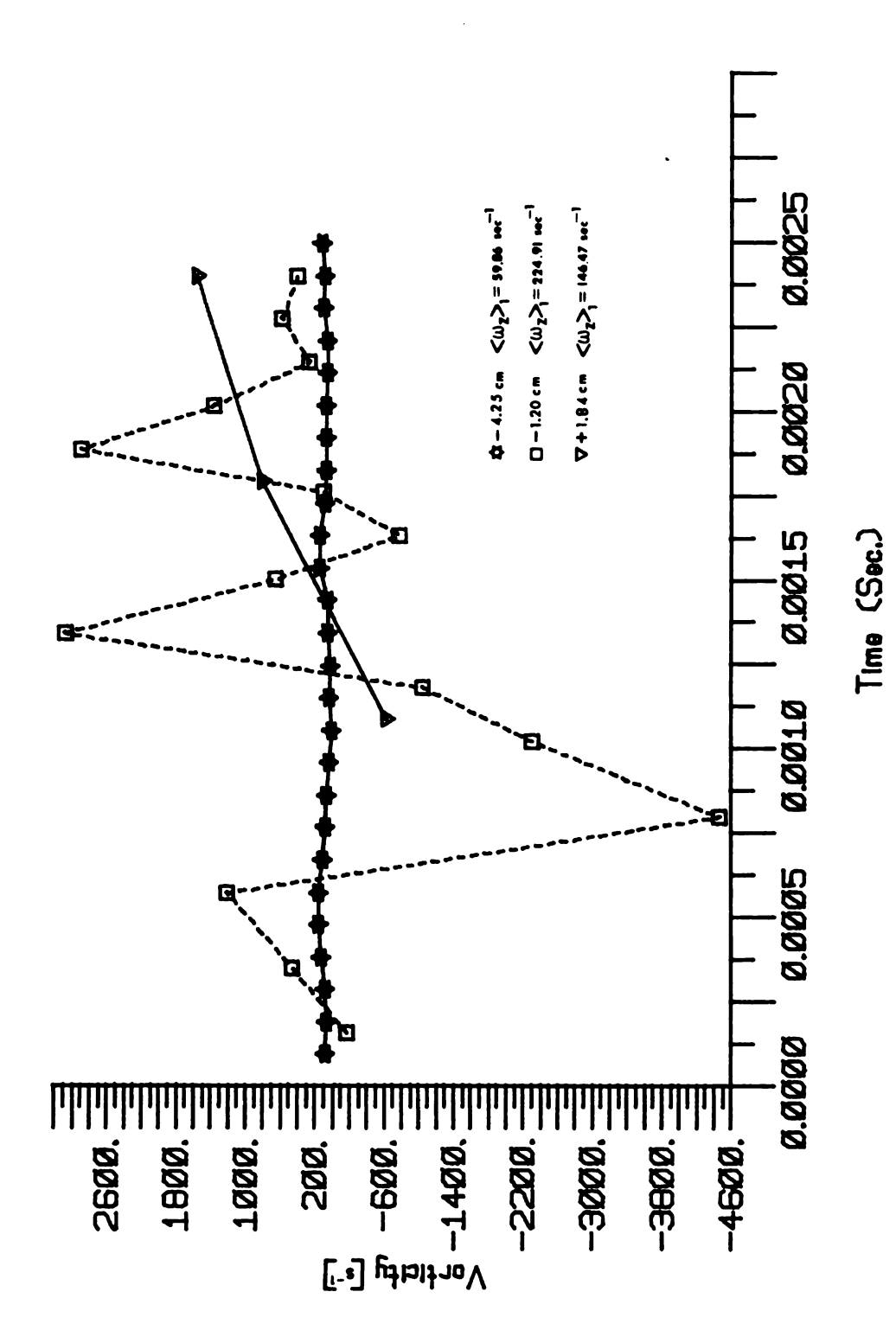
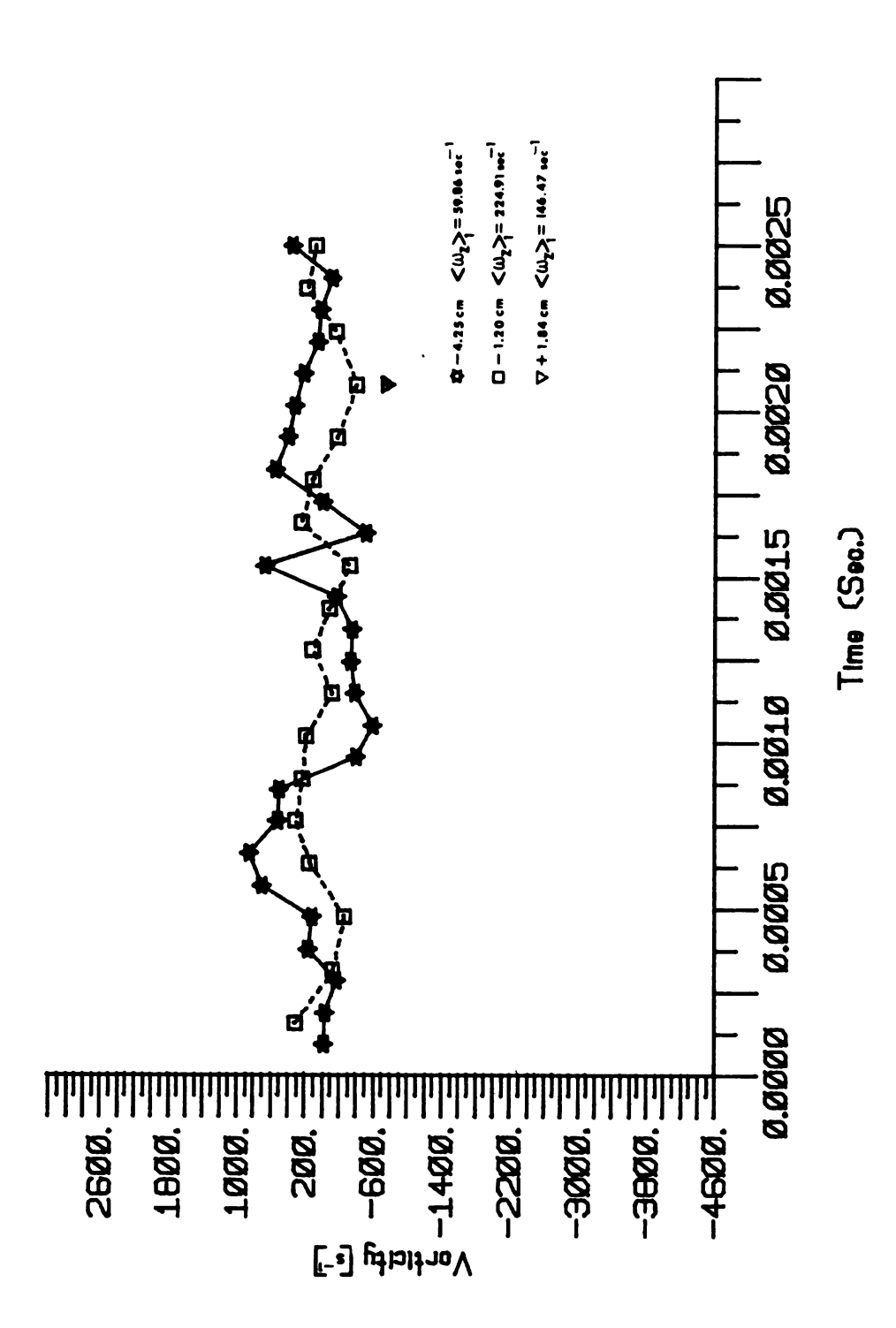


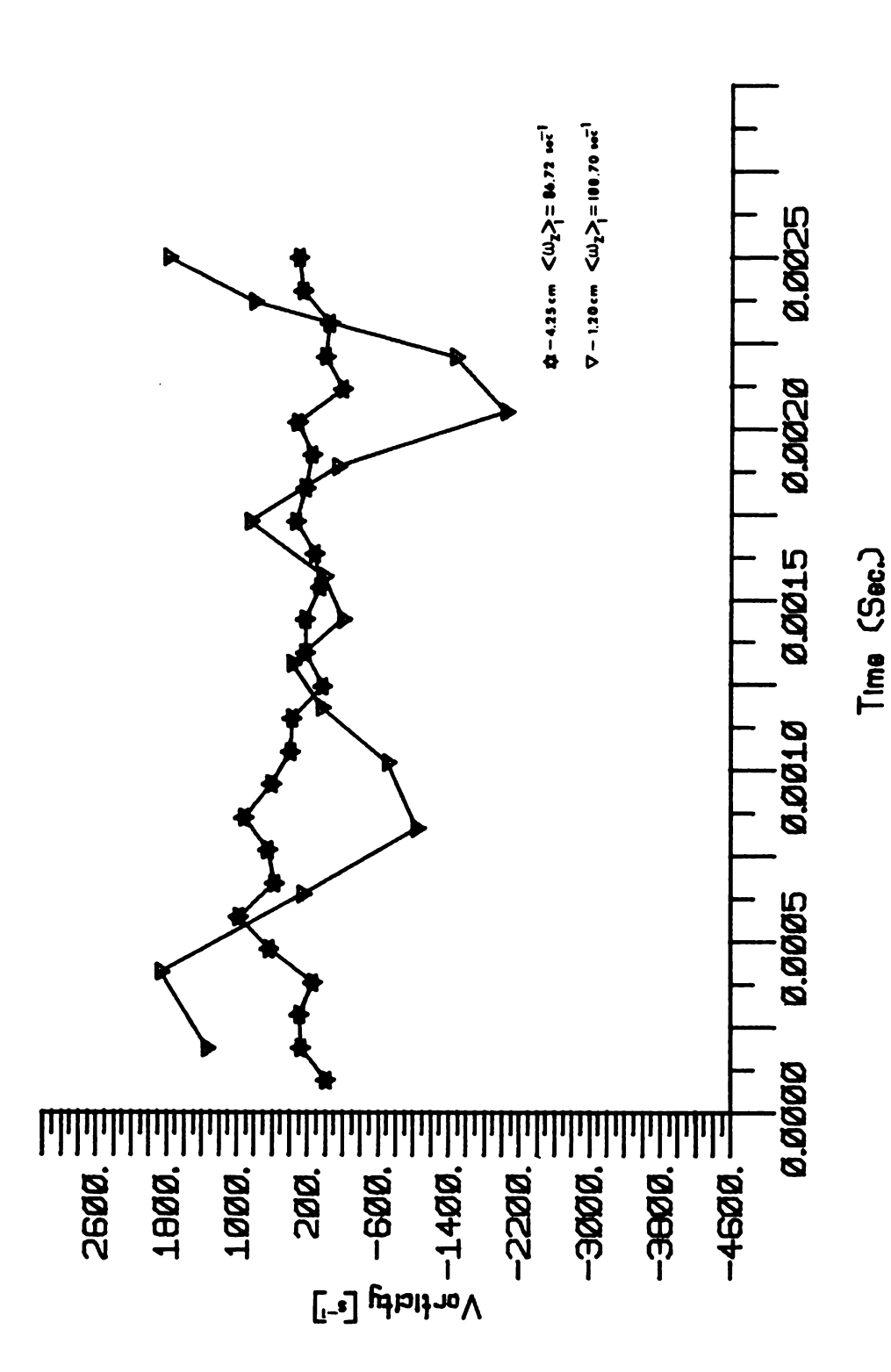
Figure 38b Phase Averaged Transverse Vorticity Time Series at X=85.4 cm and Y= 1.8, 4.9, 7.9 and 11.0 cm



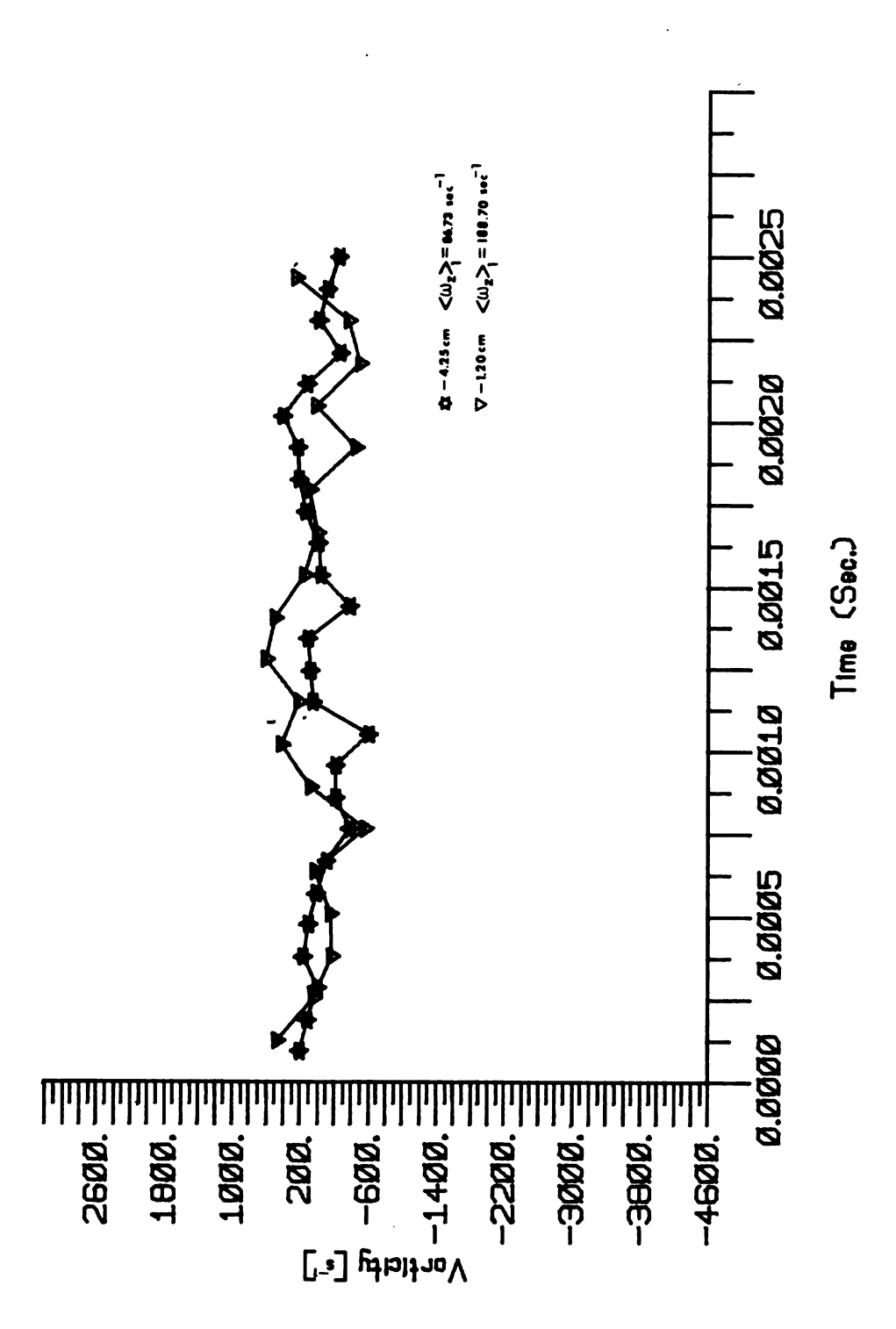
Quasi-Instantaneous Transverse Vorticity at X=18.3 cm and Y= -4.3, -1.2 and 1.8 cm Figure 39



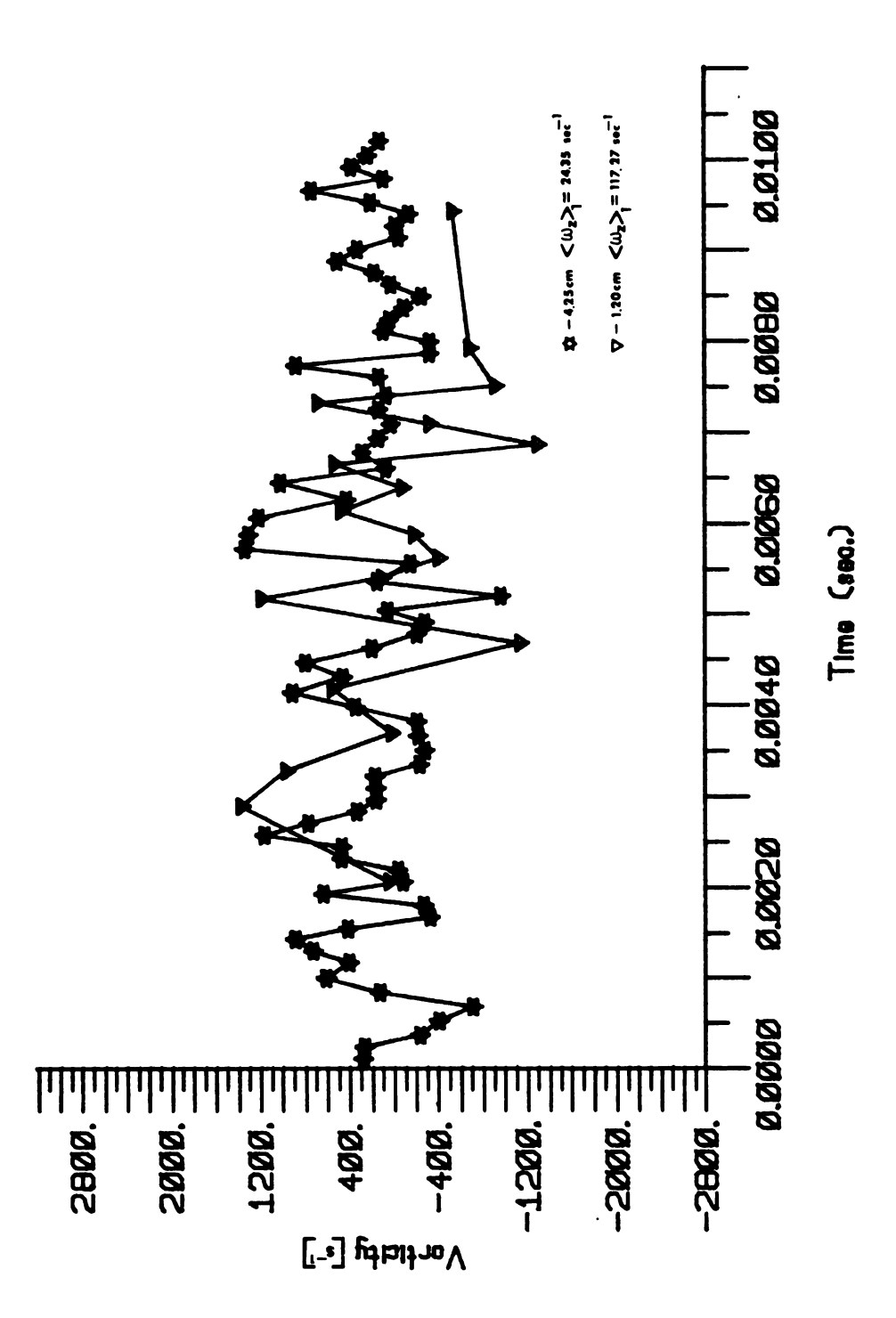
Quasi-Instantaneous Transverse Vorticity at X=18.3 cm and Y= -4.3, -1.2 and 1.8 cm Figure 40



Quasi-Instantaneous Transverse Vorticity at X=33.6 cm and Y= -4.3 and -1.2 cm Figure 41

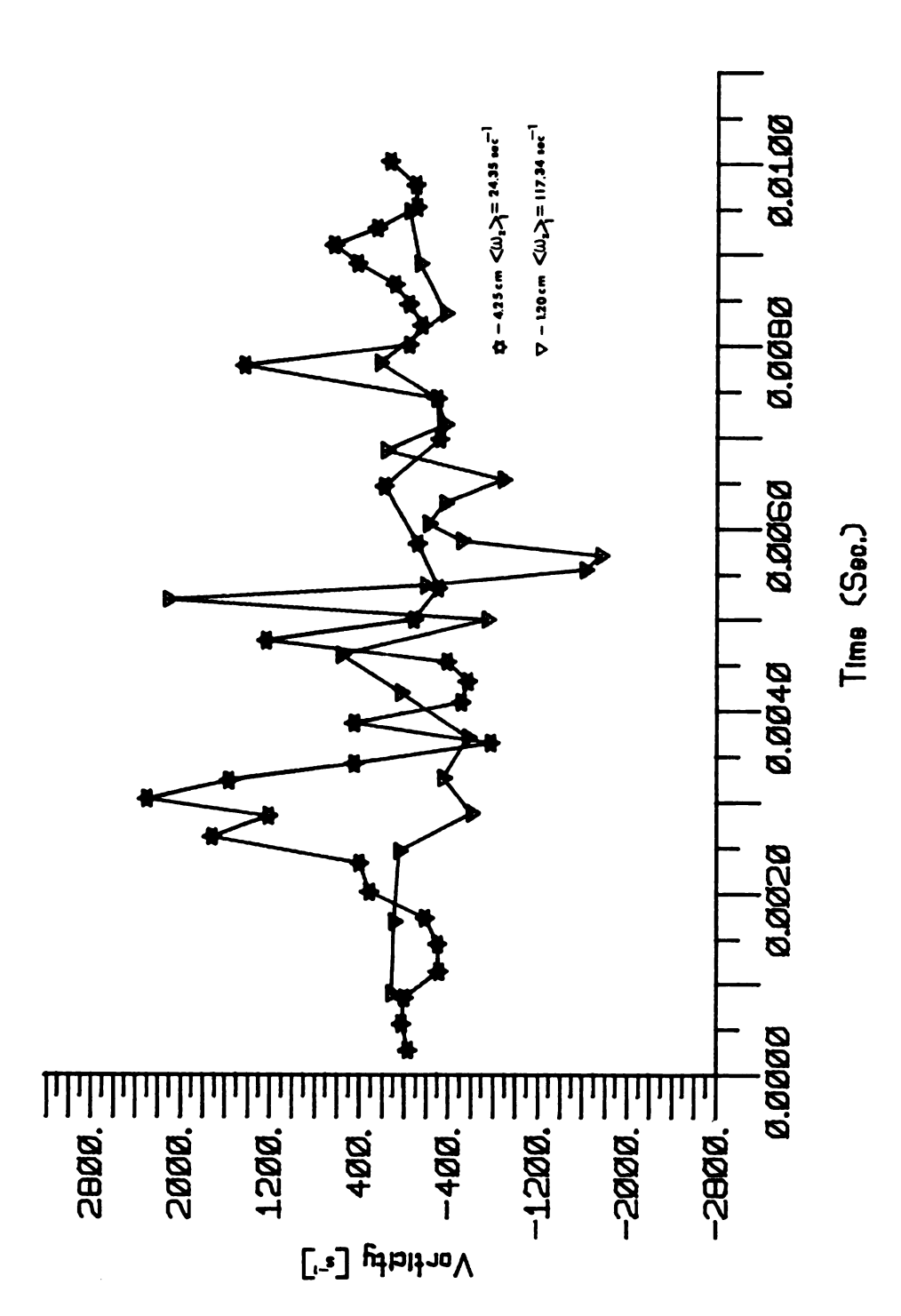


Quasi-Instantaneous Transverse Vorticity at X=33.6 cm and Y= -4.3 and -1.2 cm Figure 42

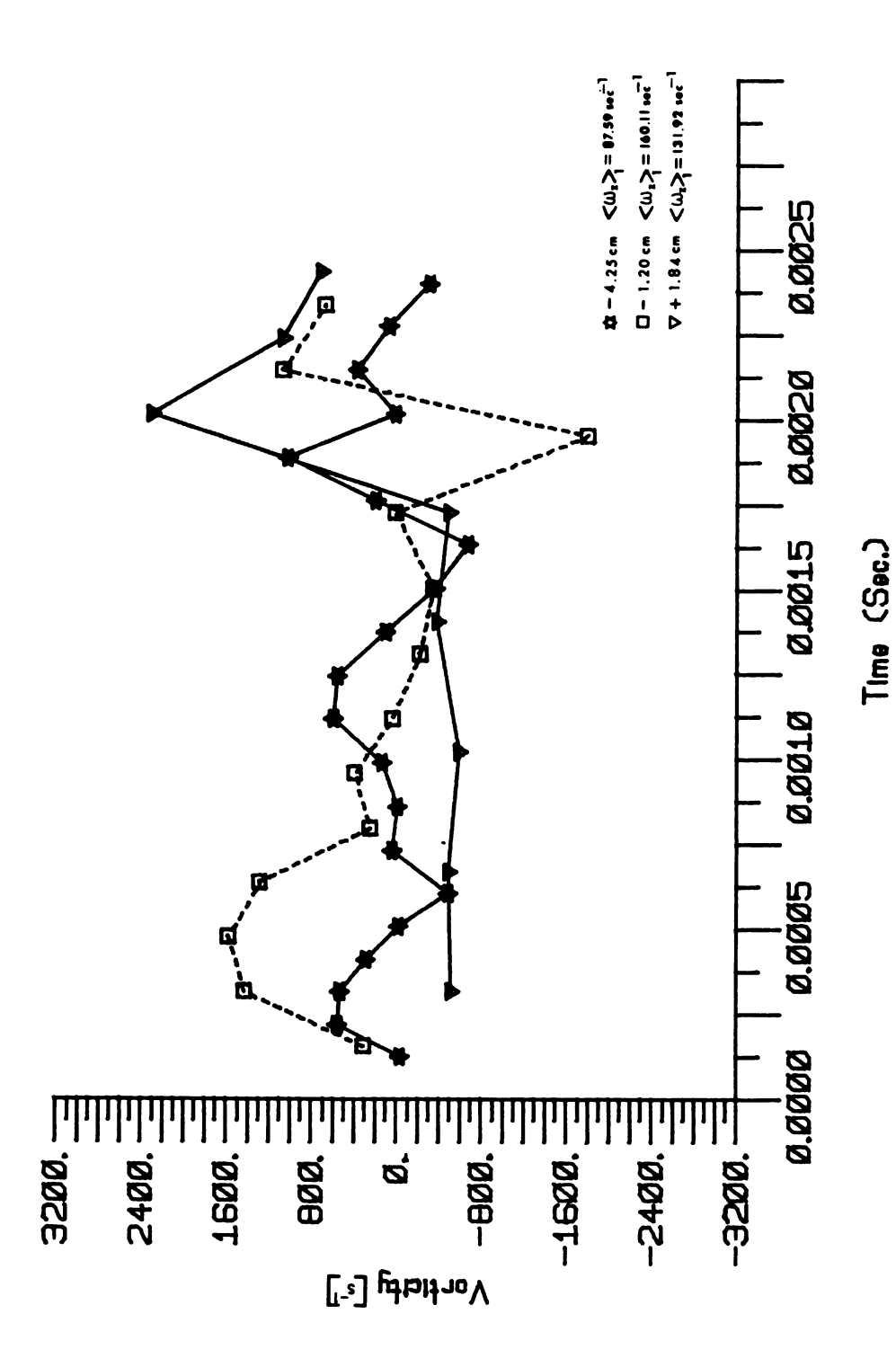


Quesi-Instantaneous Transverse Vorticity at X=42.7 cm and Y= -4.3 and -1.2 cm Figure 43

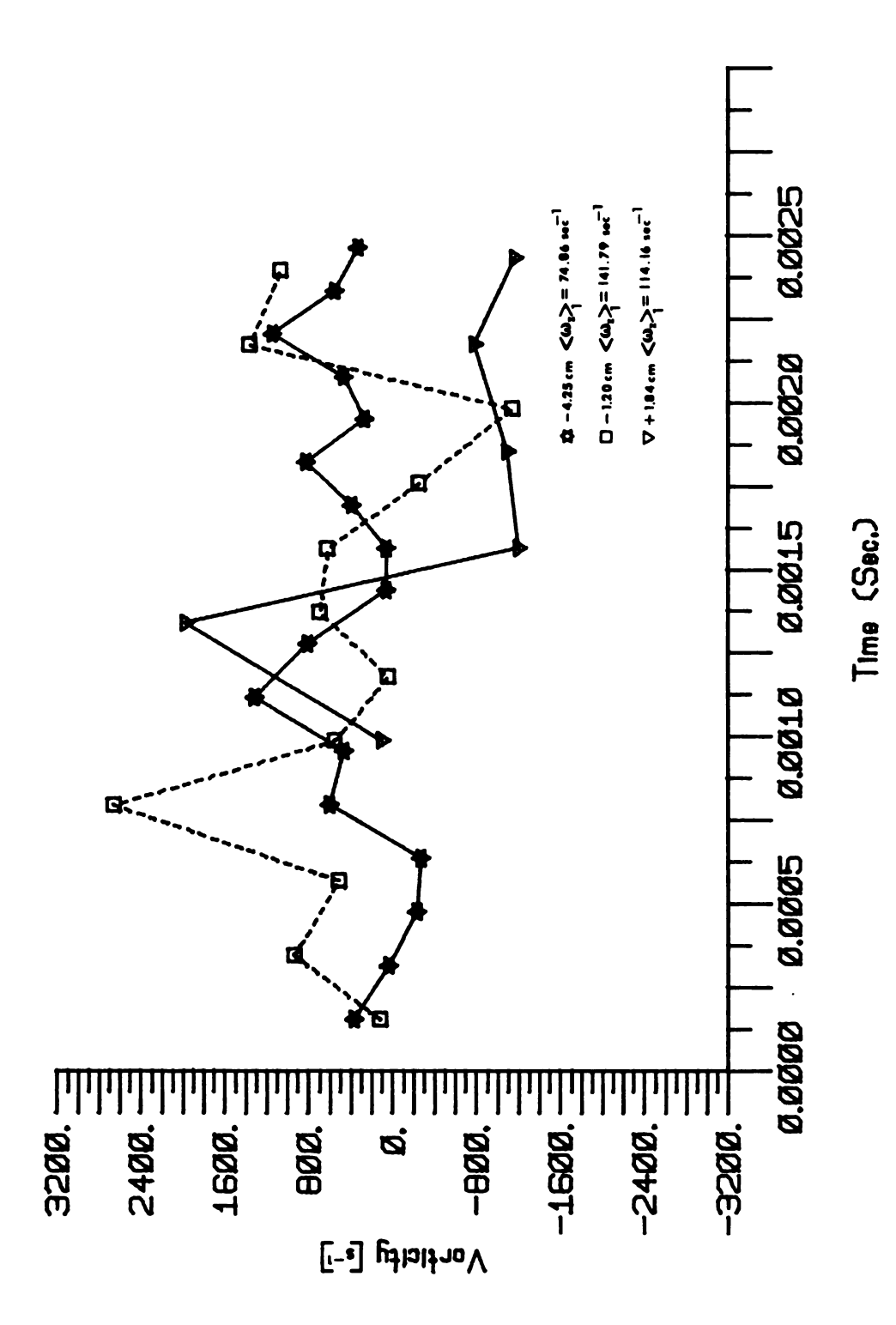
-				



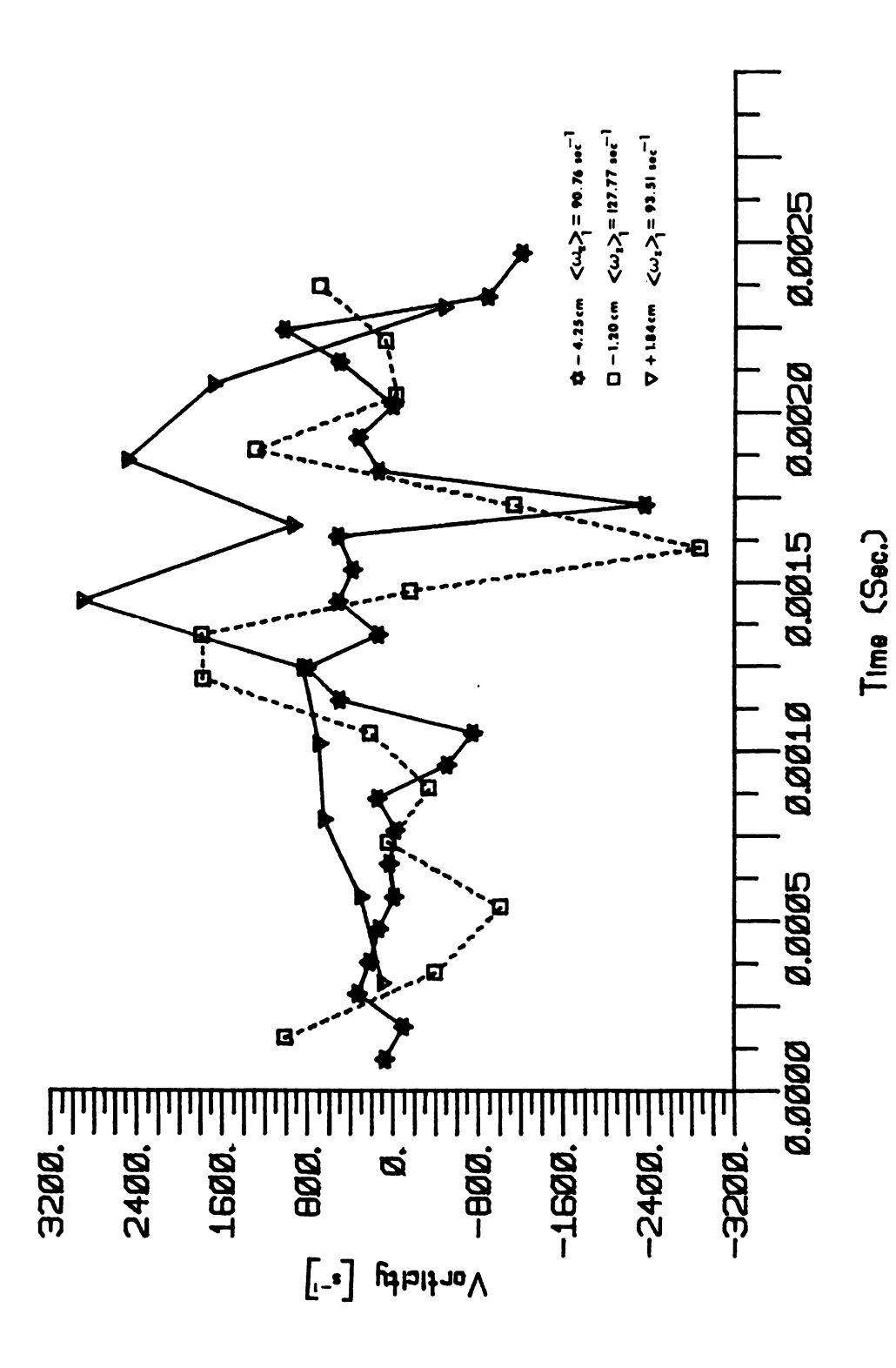
Quasi-Instantaneous Transverse Vorticity at X=42.7 cm and Y= -4.3 and -1.2 cm Figure 44



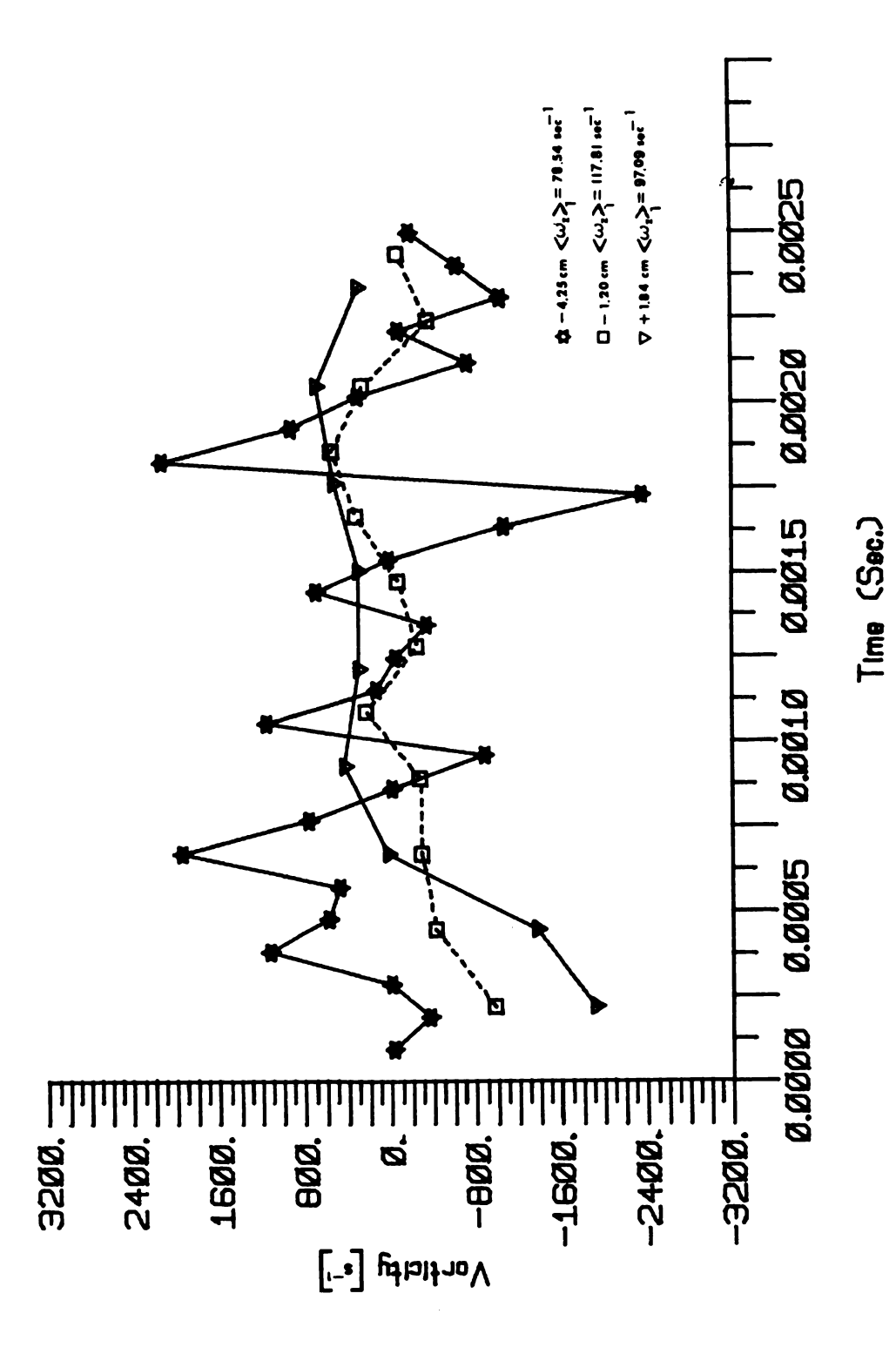
Quasi-Instantaneous Transverse Vorticity at X=48.8 cm and Y= -4.3, -1.2 and 1.8 cm Figure 45



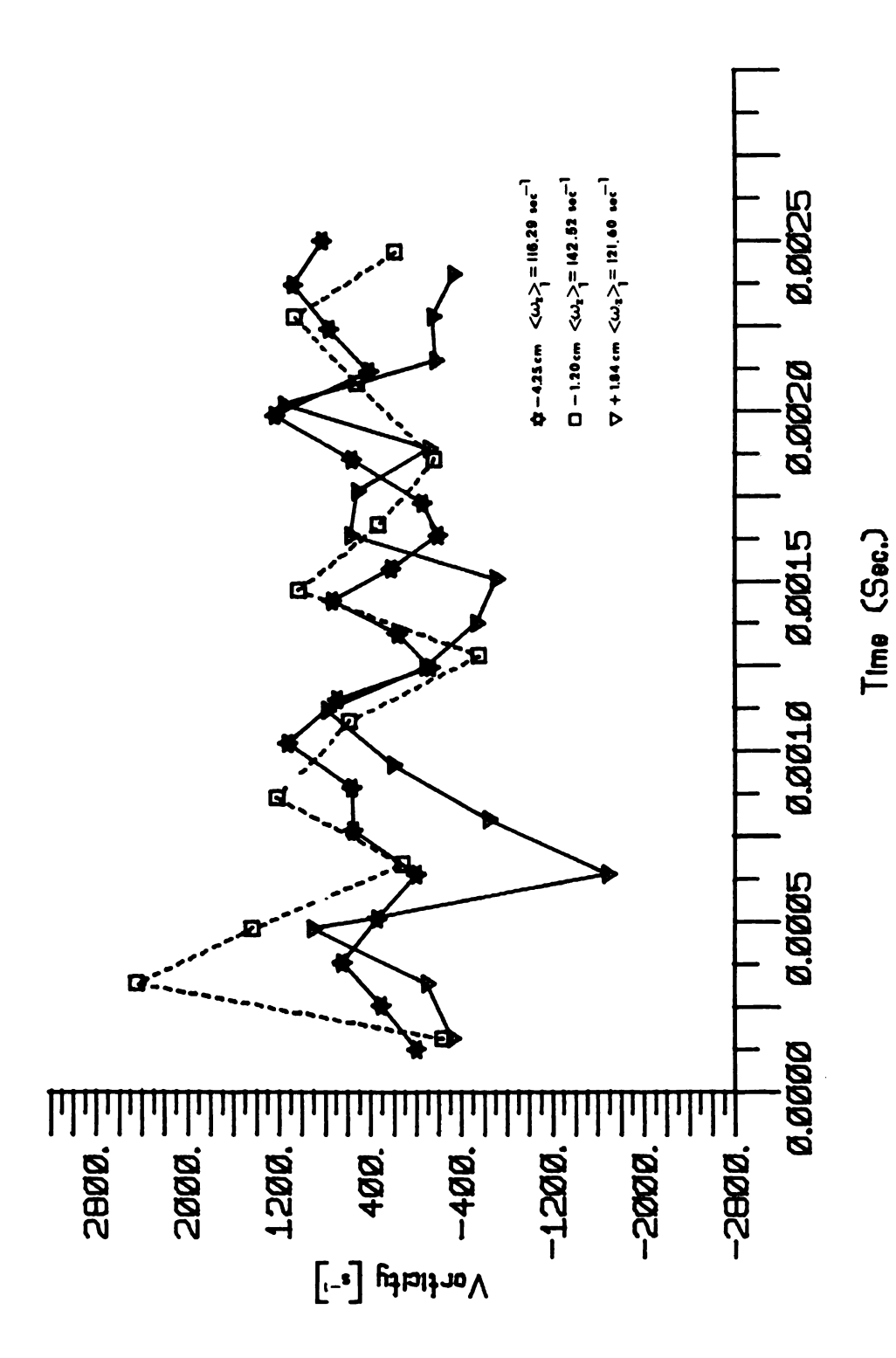
Quasi-Instantaneous Transverse Vorticity at X=51.9 cm and Y= -4.3, -1.2 and 1.8 cm Figure 46



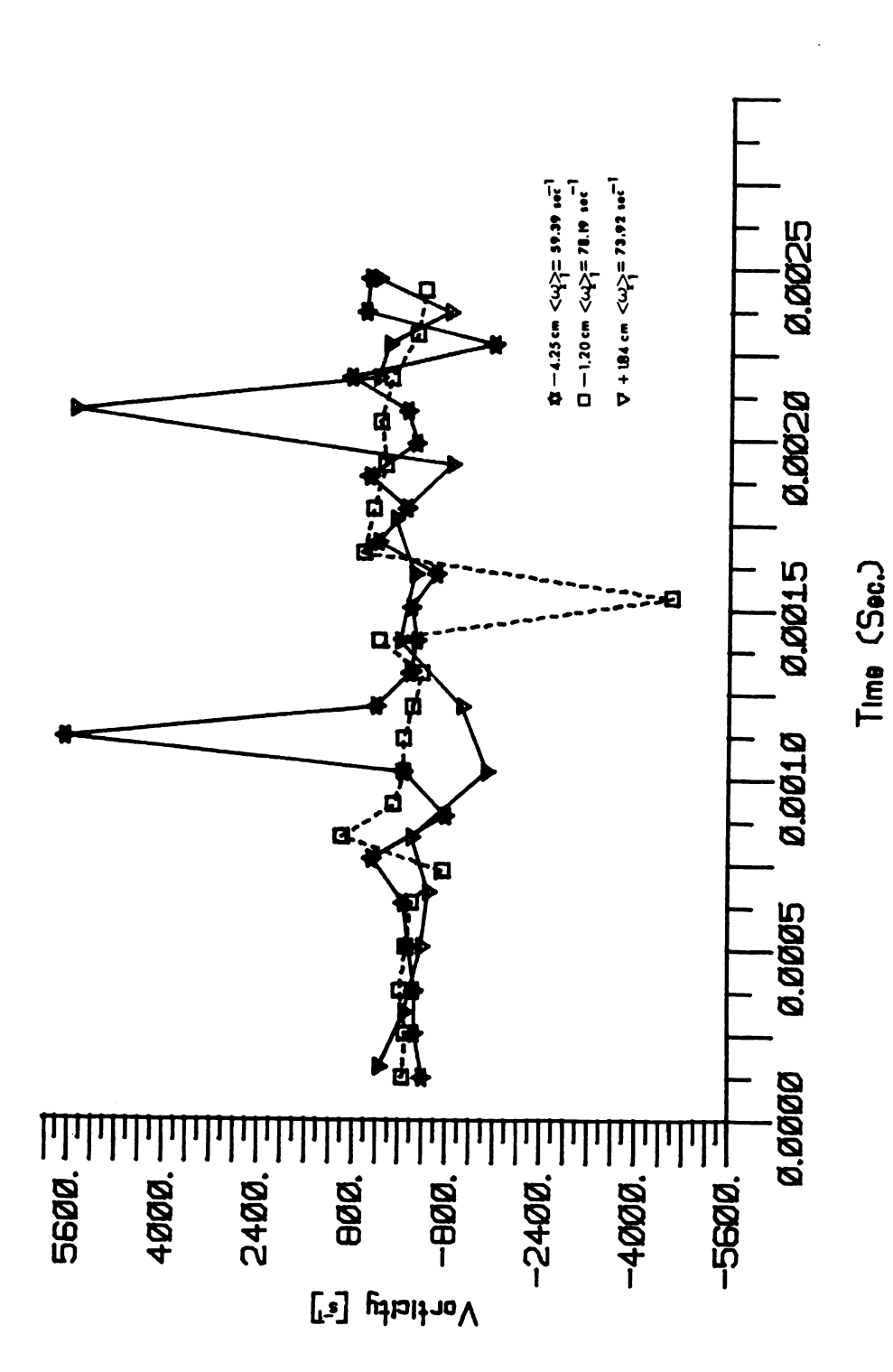
Quasi-Instantaneous Transverse Vorticity at X=58.0 cm and Y= -4.3, -1.2 and 1.8 cm Figure 47



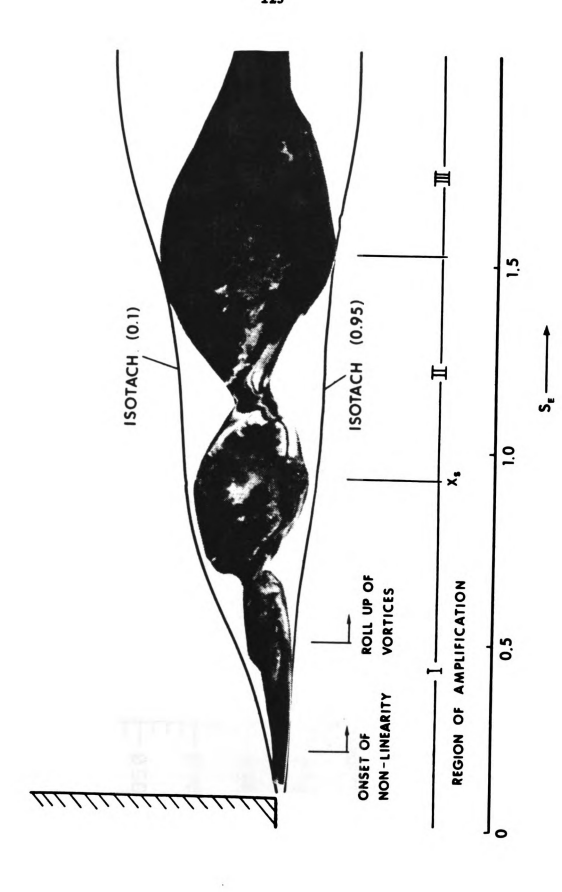
Quasi-Instantaneous Transverse Vorticity at X=61.0 cm and Y= -4.3, -1.2 and 1.8 cm Figure 48



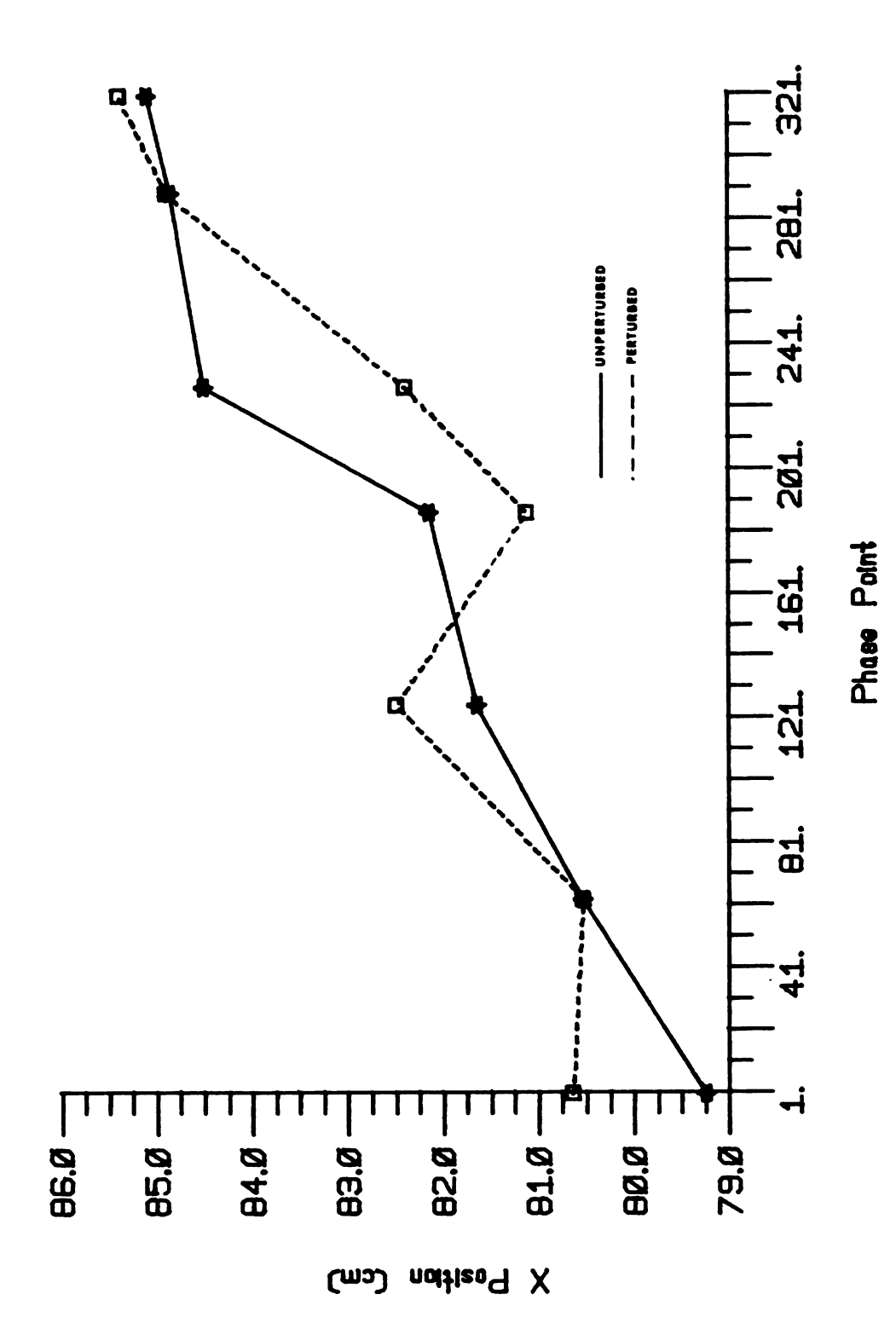
Quasi-Instantaneous Transverse Vorticity at X=79.3 cm and Y= -4.3, -1.2 and 1.8 cm Figure 49



Quasi-Instantaneous Transverse Vorticity at X=134.2 cm and Y= -4.3, -1.2 and 1.8 cm Figure 50



Velocity Isotach and Smoke Photography (Photograph 3,Taken From P.Mensing, Dissertation,1981) Figure 51



Streamwise Position of Saturated Structure Over 10.24 ms For Both the Unperturbed and Perturbed Data Figure 52



#### APPENDIX A

#### CUBIC SPLINE END CONDITIONS

This Appendix presents the results of an investigation into the affect of cubic spline end conditions. In the present cubic spline subroutine, the user is required to select various end conditions.

The following end conditions were selected for testing;

- a] the slope set equal to zero,
- b] the second derivative set equal to zero and
- c] the Not-a-Knot condition. This condition forces the change in the third derivative across the measurement point adjacent to the boundary to be equal to zero.

The first and third end conditions were eliminated for the following reasons:

a) the slope set to zero indicates U(Y) at the high speed side of the mixing layer has reached the free stream velocity and on the low speed side an asymptote has reached. This condition was not met in the present study and therfore this end condition is a poor choice.

b) the third end condition produced many relatively large regions of negative vorticity on the high speed side of the mixing layer. This would imply the existence of a region of fluid between the mixing layer and the primary flow which has a speed greater than that of the primary core fluid. Reviewing the unprocessed velocities it has been determined that this condition is unphysical in the present work.

The selection of the second end condition, the second derivative set equal to zero (or the slope set equal to a constant), allows the spline subroutine to adjust to the changing slope of the velocity profile as the calculation moves downstream within the present measurement grid.

In the following table, the spatial vorticity distribution obtained at the first phase point using the second end condition is taken as a reference and listed under  $\langle w_1 \rangle_1$  in inverse seconds. In addition, the percent deviation in the magnitude of vorticity calculated using the first and third end conditions are also compared to the reference (the second end condition) and listed in percent under  $\langle w_1 \rangle_1 / \langle w_2 \rangle_1$  and  $\langle w_3 \rangle_1 / \langle w_3 \rangle_1$  respectively.

Table A.1 Effect of Cubic Spline End Condition on the Calculated Vorticity

I(cm)	Y(cm)	$\langle w_2 \rangle (s^{-1})$	<w<sub>1&gt;/<w<sub>2&gt; %</w<sub></w<sub>	<w<sub>3&gt;/<w<sub>2&gt; %</w<sub></w<sub>
12.3	-7.3	19.38	100.00	-235.50
12.3	-4.3	42.73	-12.31	27.76
12.3	-1.2	237.63	0.57	-1.58
12.3	1.8	162.13	0.16	0.76
12.3	4.9	-32.44	-4.01	-1.11
12.3	7.9	6.99	-24.46	5.44
12.3	11.0	-4.21	-33.49	9.74
12.3	14.0	-0.73	-227.40	41.10
12.3	17.1	-0.61	-100.00	290.16
15.3	-7.3	17.35	104.38	-207.38
15.3	-4.3	47.15	-10.24	20.66
15.3	-1.2	236.15	0.55	-1.04
15.3	1.8	160.94	-0.32	0.37
15.3	4.9	-29.10	1.62	-0.48
15.3	7.9	6.40	6.56	-1.25
15.3	11.0	-3.08	12.66	0.97
15.3	14.0	-0.07	628.57	-942.86
15.3	17.1	-0.85	21.18	198.82
18.3	-7.3	11.79	104.66	-57.76
18.3	-4.3	59.86	-5.53	3.01
18.3	-1.2	224.91	0.40	-0.23
18.3	1.8	146.47	-0.14	0.10
18.3	4.9	-18.04	-0.22	-0,22
18.3	7.9	5.08	-2.56	0.20
18.3	11.0	-1.32	-9.09	8.33
18.3	14.0	0.27	-11.11	-114.81
18.3	17.1	-0.50	-76.00	266.00
21.4	-7.3	7.22	101.80	259.97
21.4	-4.3	70.58	-2.79	-7.11
21.4	-1.2	213.01	0.25	0.64
21.4	1.8	137.48	-0.12	-0.27
21.4	4.9	-4.35	1.38	2.30
21.4	7.9	2.90	0.34	-1.72
21.4	11.0	0.05	80.00	100.00
21.4	14.0	0.75	-4.00	-29.33
21.4	17.1	0.73	68.75	234.37
24.4	-7.3	9.31	93.56	307.20
24.4	-4.3	77.39	-3.01	<b>-9.9</b> 0
24.4	-1.2	199.40	0.32	1.03
24.4	1.8	136.13	-0.12	-0.40
24.4	4.9	7.61	0.53	
24.4	7.9	1.97	-1.02	1.84 -1.52
24.4	11.0	1.35	-1.02 0.74	-1.52 0.74
24.4	14.0	0.81	-9.88	1.23
24.4		0.67	38.81	-4.48
	17.1 -7.3	8.16	66.91	466.54
27.5		83.91		
27.5	-4.3	93.AT	-1.74	-12.16

27.5	-1.2	198.87	0.20	1.38
27.5	1.8	139.64	-0.07	-0.52
27.5	4.9	19.09	0.21	1.05
27.5	7.9	2.05	-0.49	-1.95
27.5	11.0	3.09	0.97	-1.29
27.5	14.0	1.08	-10.19	14.81
27.5	17.1	0.80	50.00	-78.75
30.5	-7.3	6.61	34.49	628.90
30.5	-4.3	84.10	-0.73	-13.25
30.5	-1.2	198.52	0.09	1.51
30.5	1.8	146.24	-0.03	-0.55
30.5	4.9	30.10	0.03	0.70
30.5	7.9	1.41	-0.71	-2.84
30.5	11.0	2.62	1.15	-0.38
30.5	14.0	0.33	-27.27	63.64
30.5	17.1	0.70	47.14	-105.71
33.6	-7.3	8.16	71.69	572.79
33.6	-4.3	86.73	-1.80	-14.44
33.6	-1.2	188.70	0.22	1.78
33.6	1.8	148.05	-0.08	-0.60
33.6	4.9	39.33	0.10	0.56
33.6	7.9	0.66	-7.58	0.00
33.6	11.0	1.76	9.09	-16.48
33.6	14.0	-0.54	-107.41	151.85
33.6	17.1	2.41	89.63	-136.93
36.6	-7.3	8.75	-0.46	592.46
36.6	-4.3	91.98	0.01	-15.10
36.6	-1.2	186.19	-0.01	2.00
36.6	1.8	152.58	0.00	-0.65
36.6	4.9	46.65	0.02	0.54
36.6	7.9	2.95	-1.02	-0.34
36.6 36.6	11.0 14.0	1.57	8.28	5.10
36.6	17.1	-0.16 1.77	-281.25 95.48	643.75 -170.06
39.7	-7.3	-27.52	-10.86	228.71
39.7	-4.3	60.88	1.33	-27.69
39.7	-1.2	156.21	-0.14	2.89
39.7	1.8	140.66	0.04	-0.86
39.7	4.9	59.79	-0.02	0.52
39.7	7.9	4.16	-0.48	-0.72
39.7	11.0	0.34	23.53	-352.94
39.7	14.0	-1.72	-18.02	-6.40
39.7	17.1	0.54	212.96	-524.07
42.7	<b>-7.3</b>	-32.24	-8.56	87.44
42.7	-4.3	24.35	3.04	-31.01
42.7	-1.2	117.27	-0.16	1.73
42.7	1.8	129.91	0.04	-0.42
42.7	4.9	66.49	-0.03	0.21
42.7	7.9	14.67	0.14	-0.27
42.7	11.0	5.93	-1.18	64.59
42.7	14.0	3.73	6.97	85.52
42.7	17.1	-0.51	-186.27	5.88
45.8	-7.3	24.97	-19.38	136.44

45.8	-4.3	80.59	1.61	-11.32
45.8	-1.2	153.15	-0.23	1.57
45.8	1.8	144.89	0.07	-0.35
45.8	4.9	69.38	-0.07	-0.53
45.8	7.9	13.97	0.72	14.24
45.8	11.0	3.99	-9.02	49.37
45.8	14.0	-3.34	40.12	-75.15
45.8	17.1	-5.65	-88.85	-26.55
48.8	-7.3	24.17	30.04	185.31
48.8	-4.3	87.59	-2.21	-13.70
48.8	-1.2	160.17	0.32	2.01
48.8	1.8	131.92	-0.11	-0.65
48.8	4.9	60.86	0.05	0.38
48.8	7.9	14.78	0.07	-0.41
48.8	11.0	-2.44	-2.87	-154.51
48.8	14.0	-4.97	5.43	-66.60
48.8	17.1	-3.21	-31.46	
51.9	-7.3	-0.93	1013.98	12.15 6515.05
51.9	-4.3	74.86	-3.38	
51.9	-1.2			-21.69
51.9	1.8	141.79	0.48 -0.16	3.07
51.9	4.9	114.16		-1.02
		60.26	0.08	0.51
51.9	7.9	11.87	-0.25	-0.76
51.9	11.0	2.76	1.45	37.68
51.9	14.0	1.01	-10.89	86.14
51.9	17.1	0.28	157.14	-14.29
54.9	-7.3	19.94	115.05	257.17
54.9	-4.3	83.02	-7.40	-16.55
54.9	-1.2	134.67	1.23	2.73
54.9	1.8	106.11	-0.42	-0.93
54.9	4.9	58.99	0.20	0.46
54.9	7.9	14.21	-0.28	-0.70
54.9	11.0	2.15	1.40	-5.58
54.9	14.0	1.71	-6.43	-43.86
54.9	17.1	0.09	455.56	2166.67
58.0	-7.3	22.48	117.79	277.05
58.0	-4.3	90.76	-7.81	-18.39
58.0	-1.2	127.77	1.49	3.50
58.0	1.8	93.51	-0.55	-1.28
58.0	4.9	59.96	0.23	0.53
58.0	7.9	18.37	-0.38	-0.54
58.0	11.0	4.98	2.41	2.61
58.0	14.0	2.26	-17.70	-3.54
58.0	17.1	1.06	138.68	45.28
61.0	-7.3	37.37	115.17	98.05
61.0	-4.3	78.54	-14.69	-12.50
61.0	-1.2	117.81	2.62	2.23
61.0	1.8	97.09	-0.85	-0.72
61.0	4.9	63.67	0.38	0.30
61.0	7.9	23.74	-0.51	-0.21
61.0	11.0	5.93	3.71	-0.51
61.0	14.0	3.40	-22.35	2.35
61.0	17.1	2.31	122.08	-15.58
	- <del>-</del>	<del></del>		

64.1	-7.3	55.81	106.09	43.15
64.1	-4.3	82.32	-19.27	-7.84
64.1	-1.2	99.67	4.26	1.74
64.1	1.8	89.26	-1.28	-0.52
64.1	4.9	65.33	0.49	0.18
64.1	7.9	28.54	-0.49	-0.14
64.1	11.0	9.94	2.31	0.30
64.1	14.0	5.28	-14.58	-0.57
64.1	17.1	3.67	77.66	3.54
67.1	-7.3	63.26	102.21	44.12
67.1	-4.3	95.13	-18.22	-7.86
67.1	-1.2	99.96	4.65	2.01
67.1	1.8	93.61	-1.34	-0.58
67.1	4.9	74.95	0.47	0.19
67.1	7.9	34.68	-0.40	-0.09
67.1	11.0	15.71	1.27	-0.09
67.1	14.0	6.70	-9.55	3.13
67.1	17.1			
	-7.3	4.58	51.75	-17.25
70.2		75.69	75.95	44.30
70.2	-4.3	107.11	-14.39	-8.39
70.2	-1.2	117.84	3.50	2.05
70.2	1.8	95.90	-1.16	-0.68
70.2	4.9	78.01	0.40	0.21
70.2	7.9	38.02	-0.37	-0.08
70.2	11.0	15.09	1.52	-0.27
70.2	14.0	7.63	-10.35	2.75
70.2	17.1	4.60	63.91	-17.61
73.2	-7.3	36.05	192.07	73.01
73.2	-4.3	71.56	-25.92	-9.85
73.2	-1.2	99.20	5.01	1.90
73.2	1.8	91.84	-1.46	-0.56
73.2	4.9	79.14	0.47	0.15
73.2	7.9	43.11	-0.39	0.02
73.2	11.0	19.79	1.52	-0.86
73.2	14.0	6.73	-15.60	9.51
73.2	17.1	5.42	71.96	-44.10
76.3	-7.3	49.21	103.13	18.55
76.3	-4.3	78.15	-17.40	-3.13
76.3	-1.2	115.21	3.17	0.57
76.3	1.8	118.42	<b>-0.8</b> 3	-0.14
76.3	4.9	83.53	0.34	0.06
76.3	7.9	43.77	-0.30	-0.02
76.3	11.0	19.62	1.33	-0.05
76.3	14.0	6.94	-12.82	0.86
76.3	17.1	2.35	141.70	-9.36
79.3	-7.3	73.41	42.60	41.11
79.3	-4.3	116.29	-7.21	-6.95
79.3	-1.2	142.52	1.58	1.52
79.3	1.8	121.60	-0.50	-0.48
79.3	4.9	85.84	0.21	0.17
79.3	7.9	48.90	-0.20	-0.02
79.3	11.0	19.91	1.26	-0.45
79.3	14.0	6.02	-15.28	6.15
		·	· · -	- · <del>-</del>

79.3	17.1	2.84	120.77	-49.30
82.4	-7.3	16.77	103.94	203.34
82.4	-4.3	72.64	-6.43	-12.58
82.4	-1.2	126.13	1.00	1.94
82.4	1.8	118.25	-0.29	-0.56
82.4	4.9	86.34	0.13	
82.4	7.9	51.93	-0.17	0.21
82.4	11.0	27.64	0.98	-0.10
82.4	14.0	9.35		0.14
82.4	17.1	4.06	-10.80	-1.39
85.4	-7.3	16.32	92.86	11.33
85.4	-4.3		80.27	192.71
85.4	-1.2	61.39	-5.72	-13.73
85.4	1.8	109.75	0.87	2.06
85.4	4.9	103.93	-0.25	-0.58
85.4	7.9	76.06	0.12	0.20
85.4		46.77	-0.24	-0.02
85.4	11.0 14.0	24.86	1.37	-0.48
		8.04	-15.30	5.97
85.4	17.1	3.82	119.37	-47.91
88.4	-7.3	4.43	287.81	672.69
88.4	-4.3	44.83	-7.63	-17.80
88.4	-1.2	92.04	1.00	2.33
88.4	1.8	86.90	-0.29	-0.66
88.4	4.9	70.68	0.13	0.21
88.4	7.9	47.63	-0.25	-0.08
88.4	11.0	27.25	1.28	0.00
88.4	14.0	10.30	-12.72	0.39
88.4	17.1	4.53	107.95	-3.53
91.5	-7.3	5.17	248.94	473.89
91.5	-4.3	43.26	-7.98	-15.16
91.5	-1.2	89.17	1.04	1.97
91.5	1.8	81.46	-0.31	-0.58
91.5	4.9	64.99	0.15	0.18
91.5	7.9	55.09	-0.27	0.00
91.5	11.0	27.30	1.87	-0.40
91.5	14.0	10.56	-17.90	4.26
91.5	17.1	6.27	112.12	-26.95
94.5	-7.3	-0.74	2167.57	2951.35
94.5	-4.3	30.77	-13.94	-19.01
94.5	-1.2	69.39	1.66	2.26
94.5	1.8	64.90	-0.49	-0.65
94.5	4.9	59.01	0.20	0.19
94.5	7.9	53.13	-0.30	-0.04
94.5	11.0	27.91	1.86	-0.18
94.5	14.0	10.00	-19.50	2.00
94.5	17.1	5.96	122.15	-12.25
97.6	-7.3	7.47	300.54	220.75
97.6	-4.3	27.79	-21.66	-15.90
97.6	-1.2	61.69	2.61	1.91
97.6	1.8	57.13	-0.77	-0.56
97.6	4.9	53.01	0.30	0.17
97.6	7.9	48.55	-0.37	-0.12
97.6	11.0	30.98	1.81	0.42
71.0	11.0	30.78	1.01	V.72

97.6	14.0	13.55	-15.42	-3.62
97.6	17.1	6.40	121.56	28.44
100.6	-7.3	19.31	144.17	114.03
100.6	-4.3	45.96	-16.23	-12.84
100.6	-1.2	66.32	3.02	2.38
100.6	1.8	56.56	-0.95	-0.74
100.6	4.9	57.74	0.35	0.23
100.6	7.9	50.57	-0.44	-0.16
100.6	11.0	30.20	2.32	0.66
100.6	14.0	16.14	-15.86	-4.58
100.6	17.1	9.65	98.86	28.19
103.7	-7.3	35.33	114.21	
103.7	-4.3	42.57	-25.39	7.33
103.7	-1.2			-1.62
103.7		62.21	4.66	0.29
103.7	1.8	67.65	-1.17	-0.09
103.7	4.9	57.90	0.45	0.03
	7.9	50.80	-0.49	-0.04
103.7	11.0	35.35	2.15	0.20
103.7	14.0	17.60	-15.74	-1.48
103.7	17.1	10.70	96.26	8.79
106.7	-7.3	37.18	110.81	22.73
106.7	-4.3	51.22	-21.55	-4.41
106.7	-1.2	63.51	4.66	0.96
106.7	1.8	62.19	-1.30	-0.27
106.7	4.9	60.60	0.45	0.12
106.7	7.9	51.40	-0.53	-0.23
106.7	11.0	33.25	2.44	1.17
106.7	14.0	21.12	-13.97	-6.91
106.7	17.1	10.78	102.13	50.46
109.8	-7.3	43.00	99.74	25.35
109.8	-4.3	53.66	-21.41	-5.44
109.8	-1.2	66.18	4.65	1.19
109.8	1.8	67.25	-1.25	-0.33
109.8	4.9	62.06	0.42	0.15
109.8	7.9	44.76	-0.54	-0.34
109.8	11.0	37.97	1.82	1.32
109.8	14.0	22.00	-11.45	-8.32
109.8	17.1	9.81	95.41	69.52
112.8	-7.3	50.11	97.63	18.50
112.8	-4.3	59.69	-21.96	-4.17
112.8	-1.2	66.69	5.28	1.00
112.8	1.8	60.60	-1.60	-0.31
112.8	4.9	61.07	0.54	0.11
112.8	7.9	50.53	-0.67	-0.20
112.8	11.0	38.11	2.78	0.94
112.8	14.0	24.69	-15.80	-5.43
112.8	17.1	15.81	92.03	31.56
115.9	-7.3	55.97	85.03	1.57
115.9	-4.3	61.18	-20.84	-0.38
115.9	-1.2	76.49	4.47	0.08
115.9	1.8	74.75	-1.24	-0.03
115.9	4.9	66.24	0.48	0.05
115.9	7.9	52.36	-0.67	-0.19
	1.00	J & . J U	-V.U/	-0.13

115.9	11 0	24 76	2 06	1 04
	11.0	34.76	3.05	1.04
115.9	14.0	23.99	-16.22	-5.54
115.9	17.1	16.25	89.29	30.40
118.9	-7.3	58.87	86.22	7.90
118.9	-4.3	63.55	-21.40	-1.97
118.9	-1.2	72.99	5.01	0.47
118.9	1.8	69.95	-1.44	-0.13
118.9	4.9	53.33	0.69	0.00
118.9	7.9	49.38	-0.95	0.14
118.9	11.0	35.11	4.22	-0.83
118.9	14.0	20.60	-26.50	5.34
118.9	17.1	20.08	101.44	-20.42
122.0	-7.3	42.35	101.02	-4.58
122.0	-4.3			
		49.52	-23.14	1.05
122.0	-1.2	58.56	5.26	-0.22
122.0	1.8	65.52	-1.30	0.03
122.0	4.9	58.40	0.53	0.05
122.0	7.9	47.56	-0.86	-0.38
122.0	11.0	40.79	3.19	1.62
122.0	14.0	28.81	-16.73	-8.61
122.0	17.1	17.29	103.93	53.50
125.0	-7.3	41.25	79.42	35.22
125.0	-4.3	56.72	-15.48	-6.86
125.0	-1.2	68.14	3.46	1.53
125.0	1.8	71.91	-0.93	-0.40
125.0	4.9	65.74	0.46	0.12
125.0	7.9	50.12	-1.06	-0.08
125.0	11.0			
		42.04	4.26	0.14
125.0	14.0	31.56	-21.07	-0.70
125.0	17.1	25.40	97.64	3.11
128.1	-7.3	43.80	76.94	26.14
128.1	-4.3	59.52	-15.17	-5.14
128.1	-1.2	73.55	3.29	1.13
128.1	1.8	69.24	-0.98	-0.33
128.1	4.9	66.69	0.42	0.15
128.1	7.9	51.83	-0.87	-0.29
128.1	11.0	40.49	3.83	1.28
128.1	14.0	31.42	-18.30	-6.05
128.1	17.1	21.70	98.85	32.76
131.1	<b>-7.3</b>	32.64	87.65	26.23
131.1	-4.3	48.56	-15.77	-4.76
131.1	-1.2	72.01	2.87	0.83
131.1	1.8			
131.1		65.27	-0.89	-0.28
	4.9	61.34	0.47	0.08
131.1	7.9	52.35	-1.03	-0.13
131.1	11.0	39.90	4.69	0.50
131.1	14.0	31.78	-21.81	-2.30
131.1	17.1	26.98	95.92	10.16
134.2	-7.3	40.17	75.85	33.78
134.2	-4.3	59.39	-13.82	-6.01
134.2	-1.2	78.19	2.78	1.32
134.2	1.8	73.92	-0.87	-0.31
134.2	4.9	63.26	0.44	0.19

134.2	7.9	48.71	-1.17	-0.18
134.2	11.0	40.05	4.97	0.82
134.2	14.0	36.32	-20.37	-3.30
134.2	17.1	28.29	97.56	15.87
137.2	-7 <b>.</b> 3	41.40	77.63	12.51
137.2	-4.3	57.67	-14.70	-2.90
137.2	-1.2	77.99	3.08	0.22
137.2	1.8	85.94	-0.69	-0.30
137.2	4.9	61.86	0.57	-0.30
137.2	7.9	44.27	-1.15	-0.54
137.2	11.0	46.65	3.88	1.31
137.2	14.0	36.38	-18.31	-6.46
137.2	17.1	26.00	95.58	33.54
140.3	-7.3	38.98	76.86	2.46
140.3	-4.3	52.01	-16.42	1.50
140.3	-1.2	79.97	2.30	1.04
140.3	1.8	83.83	-1.04	0.61
140.3	4.9	61.38	0.13	0.85
140.3	7.9	44.24	-1.31	0.02
140.3	11.0	45.01	4.11	1.84
140.3	14.0	38.51	-18.15	-7.24
140.3	17.1	25.85	100.43	41.20
143.3	-7.3	7.75	289.81	88.52
143.3	<b>-4.3</b>	23.77	-17.25	-23.94
143.3	-1.2	51.40	5.49	-4.55
143.3	1.8	55.32	0.85	-3.90
143.3	4.9	52.91	2.00	-3.14
143.3	7.9	47.64	-0.97	-1.91
143.3	11.0	35.78	6.15	0.17
143.3	14.0	33.60	-23.21	-4.23
143.3	17.1	27.92	105.59	15.83
146.4	-7.3	13.91	182.53	150.32
146.4	<b>-4.3</b>	28.24	-49.36	31.13
146.4	-1.2	43.90	-5.92	27.54
146.4	1.8	52.70	-7.72	13.57
146.4	4.9	41.17	-6.46	15.72
146.4	7.9	40.90	-2.81	7.68
146.4	11.0	40.79	4.88	1.25
146.4	14.0	28.08	-31.13	9.44
146.4	17.1	30.96	100.61	-21.25
149.4	-7 <b>.</b> 3	40.28	100.00	-55.04
149.4	-4.3	65.11	24.30	-73.3 <b>8</b>
149.4	-1.2	80.20	24.25	-51.22
149.4	1.8	71.38	17.37	-38.86
149.4	4.9	65.71	17.27	-36.48
149.4	7.9	50.15	2.71	-22.89
149.4	11.0	43.38	6.50	-7.15
149.4	14.0	36.47	-15.00	-14.61
149.4	17.1	25.79	100.00	29.39

#### APPENDIX B

### STANDARD DEVIATION OF THE X-ARRAY VOLTAGES

An evalution of the sensitivity of the vorticity contours to perturbations in the measured voltages required the development of perturbation values for wires one and two of the X-array. The instantaneous time series voltages were used to create estimates of the standard deviation,  $(\overline{\sigma})$  values as shown in the following relationships. Note that  $\langle \sigma \rangle_i$  is the standard deviation based upon the phase averaged voltage  $\langle E \rangle_i$  and the instantaneous voltage,  $E_i$  for the i-th phase point.

$$\langle \sigma_1 \rangle_i = \left[ 1/30 \sum_{n=1}^{30} \left[ nE_1 - \langle E_1 \rangle \right]^3 \right]^{1/3}$$

$$\langle \sigma_{2} \rangle_{i} = \left[ 1/30 \sum_{n=1}^{30} \left[ nE_{2} - \langle E_{2} \rangle \right]^{2} \right]^{1/2}$$

The standard deviations at each phase point were then averaged over all phase points resulting in  $\sigma_1$  and  $\sigma_2$ , see Table B.1.

Table B.1 Standard Deviation for X-array Voltages

I cm	Y cm	σ <sub>1</sub> (mv)	- σ <sub>3</sub> (mv)
12.3	-7.3	5.99	6.66
12.3	-4.3	51.48	30.91
12.3	-1.2	100.85	78.16
12.3	1.8	193.03	146.61
12.3	4.9	87.78	117.98
12.3	7.9	109.83	95.70
12.3	11.0	113.52	101.29
12.3	14.0	102.32	116.19
12.3	17.1	120.81	130.81
15.3	-7.3	6.09	5.77
15.3	-4.3	40.13	31.12
15.3	-1.2	169.56	118.67
15.3	1.8	174.94	137.18
15.3	4.9	54.53	75.00
15.3	7.9	33.21	36.43
15.3	11.0	35.10	50.91
15.3	14.0	30.04	48.85
15.3	17.1	34.10	57.09
18.3	-7.3	10.15	6.42
18.3	-4.3	42.32	34.64
18.3	-1.2	143.41	79.82
18.3	1.8	236.84	170.64
18.3	4.9	52.14	98.69
18.3	7.9	40.64	59.67
18.3	11.0	29.78	42.05
18.3	14.0	28.39	36.09
18.3	17.1	31.34	47.02
21.4	<b>-7.3</b>	6.02	7.87
21.4	-4.3	53.67	40.43
21.4	-1.2	207.68	105.04
21.4	1.8	209.53	186.78
21.4	4.9	68.13	90.86
21.4	7.9	30.61	51.39
21.4	11.0	20.80	53.65
21.4	14.0	21.56	29.17
21.4	17.1	31.05	39.11
24.4	-7.3	9.92	9.67
24.4	-4.3	47.21	33.92
24.4	-1.2	138.13	110.28
24.4	1.8	250.32	191.77
24.4	4.9	64.88	117.37
24.4	7.9	36.26	63.07
24.4	11.0	23.63	44.29
24.4	14.0	26.44	33.07
24.4	17.1	15.07	21.06
27.5	-7.3	13.81	12.14
27.5	-4.3	49.91	38.34
27.5 27.5	-1.2	187.14	116.33
27.5 27.5	1.8	206.01	158.00
21.3	1.0	700 · AT	130.00

27.5	4.9	105.75	102.87
27.5	7.9	` 44.05	67.88
27.5	11.0	27.47	46.59
27.5	14.0	14.14	31.10
27.5	17.1	8.49	18.51
30.5	-7.3	10.77	11.45
30.5	-4.3	45.74	33.49
30.5	-1.2	181.38	113.79
30.5	1.8	206.88	184.12
30.5	4.9	120.79	111.26
30.5	7.9	57.71	59.45
30.5	11.0	36.11	55.75
30.5	14.0	27.67	31.83
30.5	17.1	14.11	21.69
33.6	-7.3	11.02	13.27
33.6	-4.3	48.80	43.77
33.6			
	-1.2	186.48	121.06
33.6	1.8	259.00	194.91
33.6	4.9	159.51	156.41
33.6	7.9	78.00	83.73
33.6	11.0	45.37	43.39
33.6	14.0	28.73	31.59
33.6	17.1	18.66	24.73
36.6	-7.3	11.48	11.01
36.6	-4.3	69.10	45.69
36.6	-1.2	169.96	91.52
36.6	1.8	292.91	206.74
36.6	4.9	128.13	140.66
36.6			
	7.9	96.68	62.75
36.6	11.0	66.98	50.84
36.6	14.0	33.21	43.84
36.6	17.1	22.43	21.79
39.7	-7.3	11.28	14.13
39.7	-4.3	9.77	14.29
39.7	-1.2	33.50	36.10
39.7	1.8	52.42	28.09
39.7	4.9	172.78	67.96
39.7	7.9	127.81	88.26
39.7	11.0	236.79	118.75
39.7	14.0	263.01	181.56
39.7	17.1	196.42	201.20
42.7	-7.3	8.54	16.78
42.7	-4.3	12.43	16.51
42.7	-1.2	50.43	30.66
42.7	1.8	46.56	34.68
42.7	4.9	144.42	104.68
42.7	7.9	110.15	82.54
42.7	11.0	238.48	167.40
42.7	14.0	154.10	155.70
42.7	17.1	308.35	258,29
45.8	-7.3	10.82	16.77
45.8	-4.3	8.26	13.87
45.8	-1.2	33.10	35.21
73.0	-1.2	33,10	33.21

27.5	4.9	105.75	102.87
27.5	7.9	44.05	67.88
27.5	11.0	27.47	46.59
27.5	14.0	14.14	31.10
27.5	17.1	8.49	18.51
30.5	-7.3	10.77	11.45
30.5	-4.3	45.74	33.49
30.5	-1.2	181.38	113.79
30.5	1.8	206.88	184.12
30.5	4.9	120.79	111.26
30.5	7.9	57.71	59.45
30.5	11.0	36.11	55.75
30.5	14.0	27.67	31.83
30.5	17.1	14.11	21.69
33.6	-7.3	11.02	13.27
33.6	-4.3	48.80	43.77
33.6	-1.2	186.48	121.06
33.6	1.8	259.00	194.91
33.6	4.9	159.51	156.41
33.6	7.9	78.00	83.73
33.6	11.0	45.37	43.39
33.6	14.0	28.73	31.59
33.6	17.1	18.66	24.73
36.6	-7.3	11.48	11.01
36.6	-4.3	69.10	45.69
36.6	-1.2	169.96	91.52
36.6	1.8	292.91	206.74
36.6	4.9	128.13	140.66
36.6	7.9	96.68	62.75
36.6	11.0	66.98	50.84
36.6	14.0	33.21	43.84
36.6	17.1	22.43	21.79
39.7	-7.3	11.28	14.13
39.7	-4.3	9.77	14.29
39.7	-1.2	33.50	36.10
39.7	1.8	52.42	28.09
39.7	4.9	172.78	67.96
39.7	7.9	127.81	88.26
39.7	11.0	236.79	118.75
39.7	14.0	263.01	181.56
39.7	17.1	196.42	201.20
42.7	-7.3	8.54	16.78
42.7	-4.3	12.43	16.51
42.7 42.7	-1.2	50.43	30.66
	1.8	46.56	34.68
42.7 42.7	4.9	144.42	104.68
42.7	7.9	110.15	82.54
42.7	11.0	238.48	167.40
42.7	14.0	154.10	155.70
45.8	17.1	308.35	258.29
45.8	-7.3 -4.3	10.82	16.77
45.8	-4.3 -1.3	8.26	13.87
73.0	-1.2	33.10	35.21

45.8	1.8	51.93	28.74
45.8	4.9	172.71	67.96
45.8	7.9	129.66	89.22
45.8	11.0	235.84	119.81
45.8	14.0	263.23	181.59
45.8	17.1	196.71	
48.8	<b>-7.3</b>		201.02
		17.86	22.04
48.8	-4.3	59.90	31.56
48.8	-1.2	140.31	106.02
48.8	1.8	267.31	210.44
48.8	4.9	278.81	220.65
48.8	7.9	97.68	86.11
48.8	11.0	49.23	93.74
48.8	14.0	29.87	73.05
48.8	17.1	24.04	53.05
51.9	-7.3	23.71	
51.9	-4.3		22.87
		92.99	57.53
51.9	-1.2	190.99	138.68
51.9	1.8	269.88	194.04
51.9	4.9	212.24	182.24
51.9	7.9	153.74	122.05
51.9	11.0	59.53	99.68
51.9	14.0	33.17	78.20
51.9	17.1	21.64	59.59
54.9	-7.3	24.13	17.83
54.9	-4.3	103.19	
54.9	-1.2		51.75
54.9		215.56	148.01
	1.8	268.28	136.32
54.9	4.9	180.59	173.33
54.9	7.9	140.68	139.70
54.9	11.0	68.70	120.79
54.9	14.0	37.25	77.37
54.9	17.1	31.18	66.39
58.0	-7.3	18.44	19.78
58.0	-4.3	92.81	55.19
58.0	-1.2	187.03	118.50
58.0	1.8		
58.0		237.15	164.80
	4.9	285.61	148.43
58.0	7.9	101.35	149.78
58.0	11.0	50.04	98.59
58.0	14.0	33.61	81.07
58.0	17.1	25.68	42.58
61.0	-7.3	21.04	26.57
61.0	-4.3	116.20	64.85
61.0	-1.2	192.34	120.25
61.0	1.8	227.86	
61.0	4.9		125.17
61.0		204.89	151.06
	7.9	113.73	136.03
61.0	11.0	45.35	115.15
61.0	14.0	40.01	81.20
61.0	17.1	25.38	52.63
64.1	-7.3	57.05	31.06
64.1	-4.3	118.25	62.28

64.1	-1.2	179.95	98.17
64.1	1.8	272.80	158.78
64.1	4.9	223.87	179.51
64.1	7.9	156.02	151.50
64.1	11.0	87.38	111.71
64.1	14.0	32.84	64.32
64.1	17.1	36.64	44.68
67.1	-7.3	76.97	38.93
67.1	-4.3	133.40	69.43
67.1	-1.2	186.87	92.66
67.1	1.8	242.79	140.76
67.1	4.9	253.32	178.79
67.1	7.9	180.79	128.27
67.1	11.0	134.79	134.54
67.1	14.0	47.91	74.80
67.1	17.1	44.61	
70.2	-7.3		51.67
		41.92	28.69
70.2	-4.3	140.13	76.47
70.2	-1.2	215.16	115.92
70.2	1.8	206.09	138.13
70.2	4.9	204.68	200.53
70.2	7.9	165.68	177.20
70.2	11.0	132.11	118.92
70.2	14.0	69.87	107.52
70.2	17.1	55.08	70.84
73.2	-7.3	59.23	25.86
73.2	-4.3	132.35	83.60
73.2	-1.2	202.13	133.27
73.2	1.8	249.30	145.58
73.2	4.9	251.86	143.79
73.2	7.9	231.32	200.63
73.2	11.0	133.35	144.96
73.2	14.0	113.99	86.73
73.2	17.1	64.76	84.23
76.3	-7.3	31.95	32.56
76.3	-4.3	111.48	72.46
76.3	-1.2	185.99	106.00
76.3	1.8	253.97	184.83
76.3	4.9	249.57	201.84
76.3	7.9	201.90	206.88
76.3	11.0	130.55	105.88
76.3	14.0	102.31	114.19
76.3	17.1	80.54	94.67
79.3	-7.3	73.87	38.79
79.3	-4.3	117.65	69.74
79.3	-1.2	179.95	119.46
79.3	1.8	237.23	155.33
79.3	4.9	250.64	231.14
79.3	7.9	268.51	197.20
79.3	11.0	209.91	183.44
79.3	14.0	124.84	103.31
79.3	17.1	76.99	86.57
82.4	-7.3	26.94	33.21
,-	,.5	20.77	33,21

82.4	-4.3	100.64	68.43
82.4	-1.2	194.65	152.94
82.4	1.8	250.18	172.52
82.4	4.9	274.86	214.38
82.4	7.9	200.12	189.49
82.4	11.0	168.91	155.90
82.4	14.0	132.26	117.13
82.4	17.1	75.10	100.72
85.4	-7.3	29.23	37.39
85.4	-4.3	41.56	54.02
85.4	-1.2	178.10	94.94
85.4	1.8	236.00	161.75
85.4	4.9	269.14	174.11
85.4	7.9	289.96	222.81
85.4	11.0	215.78	192.86
85.4	14.0	135.61	123.89
85.4	17.1	73.00	86.37
88.4	-7.3	37.52	28.02
88.4	-4.3	83.42	62.40
88.4	-1.2	221.65	96.40
88.4	1.8	212.28	138.30
88.4	4.9	315.33	195.33
88.4	7.9	243.60	186.90
88.4	11.0	184.56	157.61
88.4	14.0	146.28	113.26
88.4	17.1	69.28	89.99
91.5	-7.3	38.35	22.86
91.5	-4.3	75.27	43.32
91.5	-1.2	130.92	91.42
91.5	1.8	218.81	141.53
91.5	4.9	213.86	206.52
91.5	7.9	181.66	186.31
91.5	11.0	210.81	180.19
91.5	14.0	165.06	162.94
91.5	17.1	76.34	105.08
94.5	-7.3	62.42	31.93
94.5	-4.3	58.35	44.89
94.5	-1.2	184.65	101.33
94.5	1.8	215.69	124.15
94.5	4.9	279.20	176.70
94.5	7.9	278.02	176.02
94.5 94.5	11.0	237.93	159.97
	14.0	117.06	129.18
94.5	17.1	95.32	103.55
97.6	-7.3 -4.3	61.08	38.30
97.6	-4.3 -1.3	115.31	53.57
97.6	-1.2	149.82	113.48
97.6 97.6	1.8	222.56	138.18
97.6 97.6	4.9 7.9	290.78	145.07
97.6	11.0	260.72 215.74	216.67
97.6	14.0	213.74 98.42	151.14 143.14
97.6	17.1	160.56	122.54
71.0	11.1	100.30	144.34

100.6	-7.3	52.62	45.36
100.6	-4.3	179.52	110.56
100.6	-1.2	213.89	114.96
100.6	1.8	244.21	142.34
100.6	4.9	259.78	163.12
100.6	7.9	236.62	155.46
100.6	11.0	233.81	181.93
100.6	14.0	129.39	152.66
100.6	17.1	85.70	126.79
103.7	-7.3	65.49	45.38
103.7	-4.3	190.63	80.66
103.7	-1.2	239.14	94.31
103.7	1.8	286.22	120.96
103.7	4.9	267.17	162.52
103.7	7.9	264.22	162.13
103.7	11.0	248.58	195.81
103.7	14.0	161.54	156.53
103.7	17.1	110.41	147.45
106.7	-7.3	81.57	41.08
106.7	-4.3	155.38	78.28
106.7	-1.2	239.60	90.71
106.7	1.8	260.49	136.90
106.7	4.9	283.23	149.72
106.7	7.9	226.21	159.10
106.7	11.0	228.74	192.97
106.7	14.0	161.47	181.54
106.7	17.1	136.70	179.86
109.8	-7.3	140.92	56.01
109.8	-4.3	176.52	90.04
109.8	-1.2	178.98	115.59
109.8	1.8	216.33	121.45
109.8	4.9	261.32	142.42
109.8	7.9	212.03	163.99
109.8	11.0	236.09	158.75
109.8	14.0	198.13	159.49
109.8	17.1	159.16	159.05
112.8	-7.3	110.07	40.74
112.8	-4.3	177.42	73.15
112.8	-1.2	170.49	102.06
112.8	1.8	223.36	113.99
112.8	4.9	230.46	151.78
112.8	7.9	232.35	199.91
112.8	11.0	195.81	174.29
112.8	14.0	178.63	200.08
112.8	17.1	123.60	179.13
115.9	-7.3	141.10	66.83
115.9	-4.3	175.62	91.74
115.9	-1.2	194.75	91.60
115.9	1.8	214.67	132.23
115.9	4.9	279.29	185.22
115.9	7.9	224.67	173.66
115.9	11.0	225.37	203.87
115.9	14.0	188.48	224.33

115.9	17.1	179.06	168.92
118.9	-7.3	170.59	78.46
118.9	-4.3	205.91	122.04
118.9	-1.2	242.33	125.87
118.9	1.8	257.11	145.25
118.9	4.9	245.54	147.68
118.9	7.9	272.79	195.34
118.9	11.0	236.31	217.26
118.9	14.0	265.71	245.21
118.9	17.1	186.71	210.27
122.0	-7.3	117.86	61.20
122.0	-4.3	167.72	70.43
122.0	-1.2	193.50	113.10
122.0	1.8	246.25	115.62
122.0	4.9	213.43	128.72
122.0	7.9	295.09	
122.0	11.0	236.78	205.55
122.0			206.35
	14.0	233.13	187.95
122.0	17.1	183.23	133.34
125.0	-7.3	145.05	62.34
125.0	-4.3	157.93	77.59
125.0	-1.2	184.89	106.65
125.0	1.8	241.08	153.68
125.0	4.9	287.88	187.77
125.0	7.9	223.91	205.73
125.0	11.0	307.54	240.21
125.0	14.0	195.56	182.47
125.0	17.1	185.82	193.79
128.1	-7.3	94.82	76.51
128.1	-4.3	133.70	74.07
128.1	-1.2	153.03	106.87
128.1	1.8	237.90	123.42
128.1	4.9	177.05	199.23
128.1	7.9	256.77	211.86
128.1	11.0	257.41	246.53
128.1	14.0	283.41	226.72
128.1	17.1	173.52	166.87
131.1	-7.3	104.54	82.29
131.1	-4.3	119.34	85.79
131.1	-1.2	196.96	130.39
131.1	1.8	203.08	141.61
131.1	4.9	264.09	160.35
131.1	7.9	274.74	233.29
131.1	11.0	278.80	187.33
131.1	14.0	235.26	236.63
131.1	17.1	198.15	167.00
134.2	-7.3	139.34	71.80
134.2	-4.3	180.76	109.34
134.2	-1.2	184.09	111.92
134.2	1.8	234.13	146.68
134.2	4.9	299.85	177.01
134.2	7.9	189.79	202.97
134.2	11.0	257.81	215.62
137.4	11.0	231.01	213.02

134.2	14.0	245.46	235.45
134.2	17.1	186.02	180.48
137.2	-7.3	66.69	73.03
137.2	-4.3	118.50	101.53
137.2	-1.2	187.87	102.69
137.2	1.8	243.38	148.67
137.2	4.9	243.34	221.89
137.2	7.9	253.67	142.48
137.2	11.0	293.85	238.52
137.2	14.0	248.60	171.36
137.2	17.1	241.04	165.36
140.3	-7.3	92.39	62.64
140.3	-4.3	109.16	76.13
140.3	-1.2	198.92	106.81
140.3	1.8	219.13	140.84
140.3	4.9	212.21	191.21
140.3	7.9	233.46	174.92
140.3	11.0	281.93	203.29
140.3	14.0	291.09	198.46
140.3	17.1	256.15	194.66
143.3	-7.3	65.23	56.78
143.3	-4.3	124.01	85.14
143.3	-1.2	139.08	89.30
143.3	1.8	168.29	125.46
143.3	4.9	255.79	158.47
143.3	7.9	217.44	205.47
143.3	11.0	247.23	169.81
143.3	14.0	295.49	206.39
143.3	17.1	192.44	182.54
146.4	-7.3	64.58	53.57
146.4	-4.3	104.19	68.02
146.4	-1.2	147.65	120.75
146.4	1.8	237.59	140.30
146.4	4.9	255.21	158.41
146.4	7.9	279.55	175.86
146.4	11.0	260.50	235.50
146.4	14.0	288.94	204.06
146.4	17.1	274.92	246.19
149.4	-7.3	64.51	53.56
149.4	-4.3	104.11	67.79
149.4	-1.2	147.83	120.91
149.4	1.8	237.44	140.63
149.4	4.9	255.97	158.80
149.4	7.9	280.04	175.38
149.4	11.0	261.03	235.48
149.4	14.0	288.89	204.31
149.4	17.1	274.62	246.09

#### APPENDIX C

# TEMPORAL EVALUATION OF VORTICITY CONTOURS

A comparison of the major features of the vorticity contours has been made in order to obtain a qualitative evaluation of the temporal evolution on a global scale. The contour plot of  $\langle w_z \rangle_{i+1}$  is referred to the similar contour plot at phase time i.

# Figure (23) (W63 with respect to W1)

- A) In the tongue region note:
- 1) the shrinkage of the  $\langle \omega_z \rangle = 200$  contour line at X=24 cm,
- 2) the movement downstream of the  $\langle \omega_z \rangle = 180$  contour line at X=37 cm, and
- B) In the interface between tongue and the newly formed vortical structure note:
- 1) the separating of the  $\langle \omega_z \rangle = 130$  contour line at X=42 cm, and
- 2) the advancement of the  $\langle w_z \rangle$ =120 contour line on the high speed side at X=42 cm.

- C) In the newly formed vortical structure note:
- 1) the elongation of the  $\langle \omega_{x} \rangle = 140$  contour line at X=51 cm, and
- 2) the tanslation of the  $\langle \omega_{\perp} \rangle = 150$  contour line at X=50 cm.
- D)Region between the newly formed and isolated vortical structure is noted:
- 1) the equidistant separation of the  $\langle \omega_z \rangle = 100$  contour line of two vortical motions; the smaller vortical fluid mass is centered at X=70 cm and the larger at X=79.5 cm.
- a) the structure at X=70 cm experiences a slight redistribution,
- b) the structure at X=79.5 cm translates downstream.
- 2) the inward movement of the 90 line at X=74 cm on the high speed side.
- E)In the large isolated structure note:
- 1)growth of the  $\langle \omega_z \rangle = 120$  and 130 contour line at X=89 cm
- 2)growth of the  $\langle \omega_x \rangle = 90$  contour line at X=91.5 cm
- F)In the region between X=98 and X=150 cm note that:
- 1) (wz)=60 contour line at X=106 cm is being pinched and
- 2) the tearing of  $\langle \omega_z \rangle = 70$  contour line at X=132 cm.

# Figure (24) (W125 with respect to W63)

- A) In the tongue region note:
- 1) the tearing and isolation of  $\langle \omega_z \rangle = 190$  line at X=34 cm,
- 2)deppression of the  $\langle w_z \rangle = 180$  line at X=30 cm.
- B) In the interface region between the tongue and the newly formed vortical structure note:
- 1) reuniting of the  $\langle \omega_z \rangle = 130$  contour line at X=42 cm,
- 2)receding of the  $\langle w_z \rangle$ =120 contour line at X=42 cm on the high speed side.
- C)In the newly formed vortical structure note:
- 1)growth of the  $\langle \omega_z \rangle$ =140 contour line at X=48 cm on the low speed side, and
- 2) the birth of the  $\langle w_z \rangle = 160$  contour line at X=48 cm.
- D)In the region between the newly formed and isolated structure note:
- 1) shrinkage of the small vortical parcel (at X=70 cm) on the front, back and top,
- 2)tearing of the  $\langle w_z \rangle = 90$  contour line at X=73 cm,
- 3)incursion of  $\langle \omega_z \rangle = 80$  contour line at X=73 cm on the high speed side.

- E) In the large isolated structure note:
- 1)slight increase in  $\langle w_z \rangle = 130$  contour line at X=82 cm, and
- 2) the slight increase in the 100 line at X=88 cm.
- F) In the region between X=98 and X=150 cm:
- 1) Tearing of the 60 line at X=122 cm from high and low speed side.

# Figure (25) (W187 with respect to W125)

- A) In the tongue region note:
- 1)shrinkage of the  $\langle w_z \rangle$ =230 contour line at X=15.5 cm
- 2)pinching down of  $\langle w_z \rangle = 180$  contour line at X=32 cm from low and high speed sides.
- 3)growth of  $\langle \omega_z \rangle$ =180, 170, 160, and 150 contour lines at X=38 to X=41 cm
- B) In the interface region between the tongue and the newly formed vortical motion note:
- 1)outward movement of 130 line at X=42 cm to high speed side.
- C) In the newly formed vortical structure note:
- 1)growth of  $\langle w_z \rangle = 150$  and 160 contour lines at X=48.5 cm
- 2)shrinkage of the  $\langle \omega_z \rangle = 140$  cotour line at X=48.5 cm.

- D) In the region between newly formed and isolated structure note:
- 1) Fusing of the 100 line upstream to the newly formed vortical structures,
- 2) further inward movement of  $\langle \omega_z \rangle = 80$  contour line at X=73 cm from high speed side.
- E) In the large isolated structure note:
- 1)slight shrinkage of  $\langle w_z \rangle = 130$  contour line at X=80 cm.
- F) In the region between X=98 cm and X=150 cm note:
- 1)pinching off of  $\langle w_z \rangle$ =60 contour line at X=122 cm from the low and high speed side.

# Figure (26) (W227 with respect to W187)

- A) In the tongue region note:
- 1)pinching down of the =180 contour line at X=34 cm.
- B) In the interface region between the tongue and the newly formed vortical motion note:
- 1)slight outward movement of the  $\langle w_{\chi} \rangle = 120$  contour line toward the high speed side (X=42 cm)
- 2)slight outward movement of the  $\langle w_z \rangle = 130$  contour line toward the high speed side (X=42 cm).

- C) In the newly formed vortical structure note:
- 1)continued growth of the  $\langle w_z \rangle = 150$  and 160 lines at X=49 cm, towards the low speed side.
- D)In the region between the newly formed and isolated structure note:
- 1) continued shrinking of vortex at X=70 cm
- 2) inward movement of  $\langle w_z \rangle = 80$  contour line at X=74 cm from high speed side.
- E) In the large isolated structure note:
- 1) shrinkage of the  $\langle \omega_z \rangle = 120$  contour line at X=80 cm,
- 2) shrinkage and translation of  $\langle \omega_z \rangle = 130$  contour line at X=80 cm.
- F) In the region between X=98 cm and X=122 cm note:
- 1) complete tearing of  $\langle w_z \rangle = 60$  contour line at X=120 cm.

### Figure (27) (W289 with respect to W227)

- A) In the tongue region note:
- 1)shrinkage of the  $\langle w_{\chi} \rangle$ =180 contour line at X=38 cm and
- 2)decay of the  $\langle \omega_z \rangle = 190$  bubble at X=36 cm.

- B) In the interface region between the tongue and the newly formed vortical motion note:
- 1)receding of the  $\langle \omega_z \rangle$ =120 and 130 contour lines at X=43 cm, toward the high speed side.
- C)In the newly formed vortical structure note:
- 1)growth of the  $\langle \omega_z \rangle = 150$  and 160 contour lines at X=48 cm,
- 2)elongation of the  $\langle \omega_z \rangle$ =100, 110, 120 and 130 contour lines in the range of 56 to 64 cm and
- 3) birth of a  $\langle \omega_z \rangle = 170$  contour line.
- D)In the region between the newly formed and isolated structure:
- 1) fusing of the isolated  $\langle \omega_z \rangle = 100$  contour line at X=70 cm to the upstream  $\langle \omega_z \rangle = 100$  contour line of the formed vortex at X=65 cm
- 2) inward movement of  $\langle \omega_z \rangle = 80$  contour line on high speed side at X=73 cm
- E) In the large isolated structure note:
- 1)deformation of the  $\langle \omega_x \rangle = 120$  contour line at X=80 cm
- 2)shrinkage of the <w\_>=130 contour line at X=85 cm
- F)In the region between X=98 cm and X=150 cm:
- 1)shrinkage of <w\_z>=80 contour line at X=140 cm

# Figure (28) (W320 with respect to W289)

- A) In the tongue region note:
- 1) shrinkage of the  $\langle \omega_z \rangle = 220$  contour line at X=18 cm,
- 2) the growth of  $\langle w_z \rangle = 190$  contour line at X=27.5 cm,
- 3)shrinkage of  $\langle w_z \rangle = 180$  contour line at X=30.5 cm and
- B) In the interface between tongue and the newly formed vortical motion note:
- 1)receding of <w\_z>=130 contour line to high speed side at X=42.5
- C)In the newly formed vortical structure note:
- 1)growth of  $\langle w_z \rangle = 150$ , 160 and 170 contour lines at X=48 cm.
- D)In the region between the newly formed and isolated structure note:
- 1) complete tearing of the  $\langle w_z \rangle$  = 80 contour line at X=73 cm
- 2) inward movement from high speed side of the  $\langle \omega_z \rangle = 70$  contour line at X=73 cm.
- E)In the large isolated structure note:
- 1) substantial reduction of the  $\langle \omega_x \rangle = 120$  contour line at X=86 cm
- 2)slight increase in <w\_>=130 contour line at X=86 cm

- F) In the region between X=98 and X=150 cm:
- 1)pinching down on  $\langle w_z \rangle$ =50 contour line from high and low speed at X=110 cm
- 2)the fusing of the  $\langle \omega_z \rangle = 60$  contour line at X=122 cm.

REFERENCES

#### REFERENCES

- Bhatia, J.C., Durst, F. and Jovanovic, J. (1982) Corrections of hot-wire anemometer measurements near walls.

  J. Fluid Mechanics 122, 411-431.
- Brown, G and Roshko, A. (1974) On density effects and large structures in turbulent mixing layers.

  J.Fluid Mechanics 64, 775-816.
- Clauser, G.H. (1954) Turbulent boundary layers in adverse pressure gradients. J. Aeronautical Sci. 21, 91,108.
- Coles, D. (1962) The turbulent boundary in a compressible fluid. Rand Corp., Rep. R-403-PR.
- Coles, D. (1968) The young person's guide to the data. AFOSR-IFP-STANFORD Conference on computation of turbulent boundary layers.
- Collis, D. C. and Williams, M. J. (1959) Two-dimensional convection from heated wires at low reynolds numbers.

  J. Fluid Mechanics 16, 357-358.
- Dimotakis, P.E., Debussy, F.D. and Keochesfahani, M.M. (1981)
  Particle streak velocity field measurements in a
  two-dimensional mixing layer. Phys. Fluids 24(6)
- Drubka, R.E. (1981) Instabilities in near field of turbulent jets and the their dependance on initial conditions and Reynolds number. Ph.D. Thesis, Illinois Institute of Technology.
- Fiedler, H., Korschelt, D. and Mensing, P. (1978) On transport mechanism and structure of scalar field in a heated plane shear layer. Lect. Notes in Physics, Vol. 76, Springer, Berlin, 58-72.

- Fiedler, H., Korschelt, D. (1979) The two dimensional jet with periodic initial conditions.

  Proc. 2nd Symp. on Turbulent Shear Flows, London.
- Fiedler, H., Dziomba, B., Mensing, P., Rosgen, T. (1980) Initiation, Evolution and Global Consequences of Coherient Structures in Turbulent Shear Flows. Lect. notes in Physics, Vol 136, Springer, Berlin, 219-251.
- Fiedler, H., and Mensing, P. (1982) "The Plane Turbulent Shear Layer With Periodic Excitation." Private Communication, Submitted for Publication
- Foss, J.F., Klewicki, C.L., and Disimile, P.J. (1984) "In preparation"
- Ho, C.M. and Huang, L.S. (1982) Subharmonics and Vortex Merging in Mixing Layers. J. Fluid Nech. 119:443-73
- Ho, C.M. and Huerre, P. (1984) Perturbed Free Shear Layers.
  Ann. Rev. Fluid Nech. 16;364-424
- Hussain, A.K.M.F. (1970) Mechanics of perturbation waves in turbulent channel flow. Ph.D. Thesis, Stanford University
- Hussain, A.K.M.F. and Reynolds, W.C. (1970) The Mechanics of an Organized wave in Turbulent Shear Flow.

  J. Fluid Mech. 41:241-58.
- Hussain, A.K.M.F. and Zaman, K.B.M. (1980) Vortex pairing in a circular jet under controlled excitation.

  Part 2.Coherent structure dynamics.

  J Fluid Mech. 101, part 3:493-544
- Hussain, A.K.M.F. and Clark, A.R., (1981) On the coherient structure of the axisymmetric mixing layer: a flow-visualization study. J. Fluid Nech. 104:263-294.
- Hussain, A.K.M.F., (1983) Coherient Structures Reality and myth, Phys. Fluids, 26(ID), 2816-2850.

- Fiedler, H., Korschelt, D. (1979) The two dimensional jet with periodic initial conditions.

  Proc. 2nd Symp. on Turbulent Shear Flows, London.
- Fiedler, H., Dziomba, B., Mensing, P., Rosgen, T. (1980) Initiation, Evolution and Global Consequences of Coherient Structures in Turbulent Shear Flows. Lect. notes in Physics, Vol 136, Springer, Berlin, 219-251.
- Fiedler, H., and Mensing, P. (1982) "The Plane Turbulent Shear Layer With Periodic Excitation." Private Communication, Submitted for Publication
- Foss, J.F., Klewicki, C.L., and Disimile, P.J. (1984)
  "In preparation"
- Ho, C.M. and Huang, L.S. (1982) Subharmonics and Vortex Merging in Mixing Layers. J. Fluid Nech. 119:443-73
- Ho, C.M. and Huerre, P. (1984) Perturbed Free Shear Layers. Ann. Rev. Fluid Mech. 16;364-424
- Hussain, A.K.M.F. (1970) Mechanics of perturbation waves in turbulent channel flow. Ph.D. Thesis, Stanford University
- Hussain, A.K.M.F. and Reynolds, W.C. (1970) The Mechanics of an Organized wave in Turbulent Shear Flow.

  J. Fluid Mech. 41:241-58.
- Hussain, A.K.M.F. and Zaman, K.B.M. (1980) Vortex pairing in a circular jet under controlled excitation.

  Part 2.Coherent structure dynamics.

  J Fluid Mech. 101, part 3:493-544
- Hussain, A.K.M.F. and Clark, A.R., (1981) On the coherient structure of the axisymmetric mixing layer: a flow-visualization study. J. Fluid Mech. 104:263-294.
- Hussain, A.K.M.F., (1983) Coherient Structures Reality and myth, Phys. Fluids, 26(ID), 2816-2850.

- Klebanoff, P.S. and Diehl, Z.W. (1951) Some features of artificially thickened fully developed turbulent boundary layers with zero pressure gradient. NACA Tech. note 2475.
- Klewicki, C.L. (1983) "A Calibration Procedure for the Measurement of Transverse Vorticity Using Hot-wire Anemometry" M.S. Thesis, Michigan State University.
- Loehrke, R.I. and Nagib, H.M. (1972) Experiments on management of free-stream turbulence. AGARD Rep. R-598.
- Loehrke, R.I. and Nagib, H.M. (1976) Control of free-stream turbulence by means of honeycombs: A balance between suppression and generation.

  Trans.A.S.M.E.I, J. Fluids Engng. 98, 342-353.
- Mensing, P. (1981) Einfluss Kontrolllierter Storungen auf line Ebene Turbulente Scherschicht, Dipl.-Eng., Dissertation Hermann-Fottinger-Institut, TU Berlin
- Oster, D. and Wygnanski, I. (1982) The forced mixing layer between parallel streams. J. Fluid Mech. 123:91-130
- Preston, J.H. (1958) The minimum Reynolds number for a turbulent boundary layer and the selection of a transition device.

  J. Fluid Mech. 3(4):373-384
- Wygnanski, I., Oster, D. and Fiedler, H. (1979) A forced plane, turbulent mixing-layer; a chalange for the predictor. Proc. 2nd symp. on turbulent shear flows, London.
- Zeman, K.B.M.Q. and Hussain, A.K.M.F. (1981) Turbulence suppression in free shear flows by controlled excitation.

  J. Fluid Mech., 103: 133-159.

